Rev.Adv.Mater.Sci. 9 (2005) 45-108

FUNDAMENTALS OF INTERFACE PHENOMENA IN ADVANCED BULK NANOSCALE MATERIALS

B. Baretzky[1], M. D. Baró[2], G. P. Grabovetskaya[3], J. Gubicza[4], M. B. Ivanov[3], Yu.R. Kolobov[3], T.G. Langdon[5,6], J. Lendvai[4], A. G. Lipnitskii[3], A.A. Mazilkin[1], A.A. Nazarov[7], J. Nogués[8], I.A. Ovidko[9], S. G. Protasova[10], G. I. Raab[7], Á. Révész[4], N.V. Skiba[9], J. Sort[2], M. J. Starink[5], B.B. Straumal[10], S. Suriñach[2], T. Ungár[4] and A.P. Zhilyaev[11]

[1] Max-Planck-Institut für Metallforschung, Stuttgart, 70569 Germany
[2] Universitat Autonòma de Barcelona, Bellaterra, 08193 Spain
[3] Tomsk State University, Tomsk, 634050, Russia
[4] Eötvös University, Budapest, 1117 Hungary
[5] Materials Research Group, School of Engineering Sciences, University of Southampton, Southampton SO17 1BJ, UK
[6] Departments of Aerospace & Mechanical Engineering and Materials Science, University of Southern California, Los Angeles, CA 90089-1453, USA.
[7] Ufa State Aviation Technical University, Ufa, 450001 Russia
[8] Institució Catalana de Recerca i Estudis Avançats (ICREA) and Departament de Física, Universitat Autònoma de Barcelona, 08193 Bellaterra (Barcelona), Spain
[9] Institute of Problems of Mechanical Engineering, RAS, St.-Petersburg, 199178 Russia
[10] Institute of Solid State Physics, RAS, Chernogolovka, 142432 Russia
[11] Institute of Mechanics, Ufa Scientific Center, RAS, Ufa, 450000 Russia

Received: March 06, 2005

Abstract The review is devoted to a study of interface phenomena influencing advanced properties of nanoscale materials processed by means of severe plastic deformation, high-energy ball milling and their combinations. Interface phenomena include processes of interface defect structure relaxation from a highly nonequilibrium state to an equilibrium condition, grain boundary phase transformations and enhanced grain boundary and triple junction diffusivity. On the basis of an experimental investigation, a theoretical description of the key interfacial phenomena controlling the functional properties of advanced bulk nanoscale materials has been conducted. An interface defect structure investigation has been performed by transmission electron microscopy (TEM), high-resolution X-ray diffraction, atomic simulation and modeling. The problem of a transition from highly non-equilibrium state to an equilibrium one, which seems to be responsible for low thermostability of nanoscale materials, was studied. Also enhanced grain boundary diffusivity is addressed. Structure recovery and dislocation emission from grain boundaries in nanocrystalline materials have been investigated by analytical methods and modeling.

Table of contents

Corresponding author: Alexander P. Zhilyaev, e-mail: AlexZ@anrb.ru

1. INTRODUCTION

At the present time, nanoscale materials can be rationally designed to exhibit novel and significantly improved physical and chemical phenomena and processes due to their nanocrystalline structure. The properties of condensed phases at the nanoscale are not necessarily predictable from those observed for coarse-grained materials. Important changes in behavior are caused not only by continuous modification of characteristics with refining microstructure but also by the emergence of entirely new phenomena, e.g. quantum size confinement, wave-like transport and predominance of interfacial phenomena [1-3]. Today there are more than 30 different processes for manufacture of nanostructured (NS) materials, including the ones based on vapor deposition (chemical and physical), sputtering, vacuum arc deposition, mechanical alloying, electrodeposition and severe plastic deformation (SPD). However, many of these are expensive, require sophisticated equipment and often produce only comparatively thin structures, typically thinner than 1 mm. Severe plastic deformation processes (equal-channel angular pressing, high-pressure torsion, multi-forging, accumulative roll bonding) do not have this drawback but instead they create a real nanocrystalline microstructure. The grain size in SPD materials is in the range of 5-1000 nm. However, there is a potential for applying SPD techniques to compact fully dense bulk nanomaterials from ball milled powders and rapidly quenched ribbons. The nanoscale materials processed to date have demonstrated novel and often extraordinary properties such as a decrease in the elastic moduli, decreases of the Curie and Debye temperatures, enhanced diffusivity and improved magnetic properties [4-6]. With respect to the mechanical properties, many experiments have revealed the potential for achieving high strength, wear resistance, good ductility at ambient temperatures and superplasticity at elevated temperatures [4,7]. A control of nanoscale grain boundary properties has permitted the development of new materials with unprecedented combinations of high toughness, strength and resistance to high-temperature creep. This breakthrough was achieved by controlling the grain boundary chemistry and structure on the nanometer scale [7]. Recently, *Nature* and *Science* published papers reporting the occurrence of low temperature and/or high strain rate superplasticity in nanocrystalline metals and alloys [8,9]. These results have remarkable scientific value for materials science since they allow the development of new technology for the superplastic forming of components having complex shapes. These superplastic properties are due not only to the ultrafine grain sizes but also to the enhanced diffusivity that have been indirectly confirmed in some publications on diffusion measurements in nanocrystalline materials [10,11]. It was shown particularly that the grain boundary phase transformations (wetting, prewetting, pre-melting) can lead to the formation of stable thin layers of the grain boundary phase [12]. The presence of a GB phase can both stabilize the fine structure of nanograined materials and ensure enhanced grain boundary diffusion [12]. Recently, it has been demonstrated that grain boundary phase transformations are responsible for the remarkable phenomenon of high-strain high-rate superplasticity in Al-alloys [13]. The unusual behaviour of grain boundaries in nanostructured ballmilled Fe suggest that they essentially represent a second phase in which the magnetic properties differ from those of bulk bcc-Fe [14,15]. The ordered paramagnetic Fe-Al alloys in the ball-milled nanostructured state exhibit ferromagnetic properties [16].

A comprehensive study of physical and mechanical properties has become possible as innovative methods for NS materials processing have been advanced. The main intriguing question examined here is how they differ in their properties and behaviour from conventional materials. There is some evidence that nanostructured materials processed by different methods can differ drastically in their properties in spite of the fact that they have comparable mean grain sizes. At least two major problems will be highlighted to examine this point. The first is concerned with the negative Hall-Petch slope observed in some experiments that was often associated with heat treatment of samples. Little attention has been focused on quantifying this heat treatment-related strengthening. It is still unclear whether these ef-

fects are due to a change of the 'inherent' properties of the grain boundaries or due to a change of the microstructure during heat-treatment [10]. Variability in the strain to failure in nanoscale metals also is not well understood. As mentioned above, superplasticity was observed in nanocrystalline nickel [8] and copper [9] processed by electrodeposition. By contrast, there is no ductility in nickel obtained by severe plastic deformation despite the fact that at the start of the testing both materials have a similar grain size. Comparable discrepancies have also been found in diffusion experiments performed on electrodeposited and SPD processed samples of nickel. Whereas electrodeposited nickel has demonstrated enhanced diffusivity that can be explained by increasing the volume fraction of the interfaces, SPD nickel possesses even higher diffusivity (by 2-3 orders of magnitude) compared to electrodeposited nickel samples. In such a case, simple physical reasoning suggests the strain to failure during superplastic deformation should be larger in SPD nickel than in electrodeposited nickel. Are these disagreements in experimental data a direct result of processing technique? Or are these differences driven by the presence of grain boundary phases formed during the SPD? An answer to these questions can be attained if different groups of investigators work as one team and disseminate and exploit their scientific results. Two successful attempts have been made to monitor microstructure evolution at early stage of deformation during ECAP [17,18] and HPT [19]. However, the main issue of SPD processing is the mechanism for development of high angle random boundaries and this is still unclear. Is it a dislocation accumulation process transforming dislocation walls into low angle boundaries and finally into high angle arrays or is it a rotation mode taking place during SPD? This problem will be addressed using severe plastic deformation of pure metals as a model material.

As was mentioned in many earlier publications (see for example [4]) high angle random boundaries formed during SPD are in a non-equilibrium state that can be characterized by enhanced GB surface energy. Some evaluations [20] indicate that the GB surface energy in SPD materials can be higher than in conventional coarse-grained materials. But no thorough investigations have been done yet. We aim to investigate the kinetics of transition from a highly non-equilibrium state to equilibrium condition, where this seems to be responsible for low thermostability of nanoscale materials. This investigation is planned using high resolution electron microscopy and high resolution x-ray, DSC/DTA analysis and atomic simulation. As noticed above, the interfacial structures and their evolution in nanoscale solids processed by different methods are essentially different not only from those in conventional coarse-grained polycrystals but also from each other. Therefore, the construction of phase diagrams containing the novel lines of the grain boundary phase transitions which allow the correct thermodynamic description of nanostructured materials is of critical importance [21]. As a result, it is necessary to delineate the temperature and concentration intervals where the nanocrystalline structure of materials is stabilized by the presence of grain boundary phases. The theoretical part of the review will be focused on modelling of the interfacial structures and phenomena in materials under study, where this information is needed to understand their nature and evaluate their potential for practical use. These studies are based on theoretical concepts, methods and models developed recently for interfaces and nanoscale processes in solids [22,23].

The review consists of the following sections.

In Section 2, general description of severe plastic deformation as a method for processing ultrafine-grained and nanocrystalline materials is discussed. We focus on three techniques used in the present work, namely, equal-channel angular pressing, high-pressure torsion and ball milling as well as their combinations. Special attention is paid to the new technique of cold HPT consolidation of ball milled powder.

Section 3 describes recent studies of the effects of plastic deformation on the Co microstructure after high pressure torsion process on un-milled and ball milled powders that have been studied and compared to those induced simply by ball milling (BM). X-ray diffraction analysis reveals that both processing routes generate in Co large amounts of stacking faults, which result in a mixture of hexaconal closely packed (hcp) and face-centered cubic (fcc) lattice. Cold-consolidation using high pressure torsion has been applied to ball-milled Fe-based amorphous ribbons to process bulk disks. The mainly amorphous bulk samples demonstrated soft magnetic behavior, higher Curie temperature and enhanced microhardness with respect to the ribbons.

Section 4 is devoted to a detailed investigation of the microstructural characteristics in samples of pure nickel processed using three different procedures of severe plastic deformation: equal-channel angular pressing (ECAP), high-pressure torsion (HPT) and a combination of ECAP and HPT. Micro-

structural characteristics such as the grain size distributions, the textures, the distributions of the misorientation angles and the boundary surface energies in the as-processed materials have been evaluated using different experimental techniques. It is shown that a combination of ECAP and HPT leads both to a greater refinement in the microstructure and to a smaller fraction of boundaries having low angles of misorientation. The estimated boundary surface energies were higher than anticipated from data for coarse-grained materials and the difference is probably due to the non-equilibrium character of many of the interfaces after SPD processing.

Section 5 describes results of studying structure and the phase composition of Al-Zn, Al-Mg and Al-Mg-Zn alloys before and after high-pressure torsion. The initial grain size of (Al) grains and reinforcing second phases decreases drastically reaching the nano-range. At the same time the Zn-rich (Al) supersaturated solid solution decomposes completely and reaches an equilibrium corresponding to room temperature. This process is less pronounced for Mg. Therefore, the severe plastic deformation of supersaturated solid solutions can be considered, similar to the irradiation at ambient temperature, as a balance between deformation-induced disordering and deformation-accelerated diffusion towards the equilibrium state.

Section 6 portrays annealing phenomena and creep behavior in nanoscale materials. Computer modeling of GB free volume and surface energy and their influence on creep behavior in nanocrystalline metals are discussed in Section 6.1. Results on the mechanisms and kinetics of relaxation (recovery) of nonequilibrium GBs in SPD- nanomaterials are reviewed in Section 6.2. The GB diffusion coefficient in nanomaterials is closely related to the nonequilibrium GB structure and depends on the time of diffusion annealing. This dependence is studied in terms of a solution of the diffusion equation with time-dependent coefficient and the experimental data on GB diffusion coefficient are analyzed on the basis of this solution. In Section 6.3 we provide a brief overview of theoretical models describing the emission of perfect and partial lattice dislocations from grain boundaries in deformed nanocrystalline materials. Focus is placed on the effects of the lattice dislocation emission on ductility of nanocrystalline materials fabricated by severe plastic deformation methods. The lattice dislocation emission from grain boundaries is treated as a manifestation of the interaction between different deformation mechanisms operating in the nanocrystalline matter.

Section 7 summarizes our current understanding of the characteristics and behavior of ultrafine-grained and nanocrystalline materials which were produced in the present work.

The present review has been written in the frame of INTAS Project (03-51-3779) under editing of the team leaders with particular contributions of team participants. Detailed information on the teams and the Project can be found on the WEB site: http://imech.anrb.ru/~INTAS03513779. This project unites East and West partners working in close areas of scientific interest in order to carry out a comprehensive study of interface structure, diffusion and related phenomena in nanoscale materials [24]. In our opinion, this review attempts to provide a comprehensive approach in which the fine structures and properties associated with the internal interfaces in nanostructured materials has been investigated through the development of a range of complementary methods and by employing project participants having expertise in several different but related experimental and theoretical areas.

2. PROCESSING AND EXPERIMENTAL

2.1. Equal-channel angular pressing and high-pressure torsion

ECAP principle. The method of ECA pressing realizing deformation of massive billets via pure shear was developed by Segal and co-workers in the beginning of the eighties [25,26]. Its goal was to introduce intense plastic strain into materials without changing the cross sectional area of billets. Due to that, repeated deformation is possible. In the early 90s the method was further developed and applied as an SPD method for processing of structures with submicron and nanometric grain sizes [4,27,28]. In these experiments the initial billets with a round or square cross section were cut from rods, from 70 to 100 mm in length. The cross sectional diameter or its diagonal did not generally exceed 20 mm.

Intense plastic straining is introduced into a sample by pressing it through a die within a channel, which is bent at a selected angle in order to impose the requisite strain by shear. Fig. 2.1a is a schematic of the principle of ECA pressing. A test sample is machined to fit within the die and is pressed through the die using a plunger. Since the two sections of the channel within the die are equal in cross section, it follows that, neglecting any end effects; the pressed sample has the same dimensions as the original sample. Thus, repetitive pressings may be easily undertaken in order to

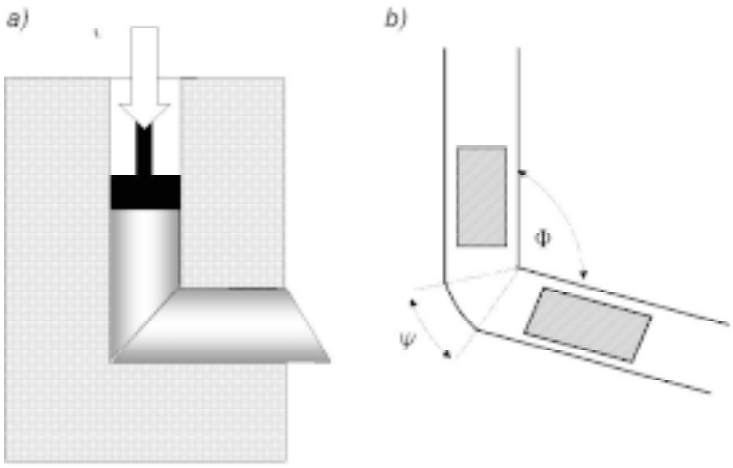

Fig. 2.1. ECAP: (a) – a schematic view, (b) – a section of the die showing the internal angles Φ and Ψ.

achieve a very high total strain. Two angles may be used to specify the strain imposed on each passage through the die. These angles, illustrated in Fig. 2.1b, represent the angle of intersection of the two channels, Φ, and the angle subtended by the outer arc of curvature at the point of intersection of the two channels, Ψ. The strain imposed on a single passage through the die is determined exclusively by the values of Φ and Ψ, and in practice it has been shown that the total strain, ε_N, accrued from N passages through the die is given by the relationship [29]:

$$\varepsilon_N = \frac{N\Phi}{\sqrt{3}}\left[2\Psi \operatorname{ctg}\left(\frac{\Phi}{2}+\frac{\Psi}{2}\right)+\Psi \operatorname{cosec}\left(\frac{\Phi}{2}+\frac{\Psi}{2}\right)\right]. \quad (2.1)$$

Model experiments have confirmed the validity of this relationship with the exception only of the sample edges where the strain may be affected by frictional effects. The value of Ψ has a relatively minor influence on the total strain. In practice, a strain of ~1 is achieved in a single pass when $\Phi = 90°$, so that a total of ten passes will give a strain close to ~10. It has been shown experimentally that an ultrafine grain size is attained most readily when the strain imposed is very intense [30]; therefore, the present experiments were conducted using dies having $\Phi = 90°$. When repetitive pressings are made on the same sample, different processing routes may be followed for the second and subsequent pressings.

Three separate possibilities are illustrated schematically in Fig. 2.2. In route A, the sample is pressed each time with no rotation; in route B the sample is rotated by 90° between each pressing, and in route C the sample is rotated by 180° between each pressing. In practice, route B may be further differentiated into route B_A, where the sample is rotated alternately by 90° in forward and backward directions between each pressing, and route B_C, where the sample is rotated by 90° in the same direction between each pressing. Experiments have shown that an ultrafine grain size with high-angle

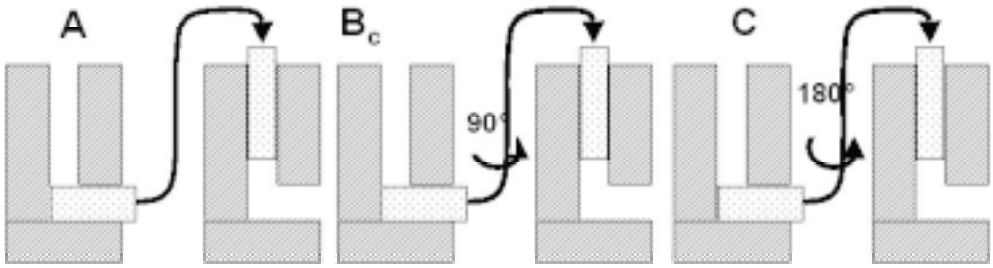

Fig. 2.2. Possible processing routes for ECAP pressing.

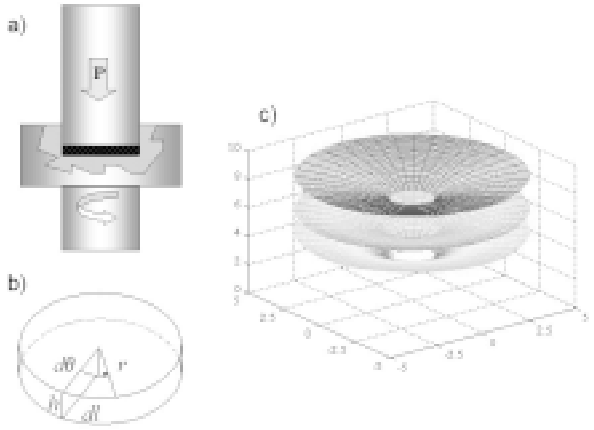

Fig. 2.3. (a) Schematic illustration of HPT processing and (b) parameters used in estimating the total strain in HPT, (c) three-dimensional representation of the total strain at the surface of a disk in HPT estimated from eqn (2.6) for totals of N = 1 (lower section), 5 (central section) and 7 (upper section) whole revolutions: the strain in the central region of the disk is not shown for simplicity.

boundaries is achieved most rapidly when using route B_C [31]. The experiments reported here were conducted using route B_C.

Principles of HPT. The conception of HPT [32] processing is depicted schematically in Fig. 2.3. Fig. 2.3a shows the sample, in the form of a disk, located between two anvils where it is subjected to a compressive applied pressure, P, of several GPa at room temperature and simultaneously to a torsional strain which is imposed through rotation of the lower support. Surface frictional forces therefore deform the disk by shear so that deformation proceeds under a quasi-hydrostatic pressure. Fig. 2.3b depicts the variables used in estimating the strain imposed in HPT where, for an infinitely small rotation, $d\theta$, and displacement, dl, it follows that $dl = rd\theta$ where r is the radius of the disk and the incremental shear strain, $d\gamma$, is given by

$$d\gamma = \frac{dl}{h} = \frac{rd\theta}{h}, \qquad (2.2)$$

where h is the disk thickness. Assuming that the thickness of the disk is independent of the rotation angle, θ, formal integration can be used so that, noting the equivalent strain $\varepsilon = \gamma / \sqrt{3}$, the true logarithmic strain, ε_{EQ}, is given by

$$\varepsilon_{EQ} = \log(1+\varepsilon) = \log\left(1+\frac{\theta r}{\sqrt{3}h}\right). \qquad (2.3)$$

Since $\theta = 2\pi N$, where N is a number of revolutions, it follows that

$$\varepsilon_{EQ} = \log\left(1+\frac{2\pi Nr}{\sqrt{3}h}\right) \qquad (2.4)$$

and in practice Eq. (2.4) is often simplified to the form [33]

$$\varepsilon_{EQ} = \log\left(\frac{2\pi Nr}{\sqrt{3}h}\right). \qquad (2.5)$$

Although Eq. (2.5) leads to a divergence of strain in the centre of the disk at $r = 0$, it is a useful relationship for determining the total strain at least within the outer rim of the disk.

An alternative relationship has also been developed which incorporates the decrease in thickness of the disk as a consequence of the applied pressure, P. For this condition, the true strain is given by [33]

$$\varepsilon_{EQ} = \log\left[\left(1+\frac{2\pi Nr}{\sqrt{3}h}\right)^2 + \left(\frac{h_0}{h}\right)^2\right]^{\frac{1}{2}}, \qquad (2.6)$$

where h_0 and h are initial and final thickness, respectively. In a very recent report, Eq. (2.6) was further simplified because, since $(2\pi Nr/h) >> 1$, it follows that [33]

$$\varepsilon_{EQ} = \frac{1}{2}\log\left[\left(\frac{2\pi Nr}{\sqrt{3}h}\right)^2 + \left(\frac{h_0}{h}\right)^2\right]. \qquad (2.7)$$

Thus, Eqs. (2.4) to (2.7) provide four distinct relationships that may be used to estimate the total strains within disks subjected to HPT.

To evaluate the significance of these four relationships, it is useful to calculate the total strains for the conditions where r = 10 mm, h_0 = 0.3 mm, h= 0.1 mm and for the situation where the disk is subjected to a total of N = 5 whole revolutions. It then follows by calculation that the values of ε_{true} are ~7.5 from Eqs. (2.4) – (2.7). Thus, the difference between these four results is negligible although in practice Eqs. (2.6) and (2.7) may be more realistic because they also incorporate the reduction in the disk thickness. Based on the uncertainties in calculating strain, it is reasonable to agree with an earlier suggestion that the straining introduced in HPT is most

realistically expressed by simply specifying the number of revolutions imposed on the sample [34].

Using Eq. (2.6), Fig. 2.3c displays the three-dimensional distributions of the total strain at the upper surface of the disk for totals of $N = 1$ whole revolutions of the sample (lower section), $N = 5$ revolutions (central section) and $N = 7$ revolutions (upper section): for simplicity in presentation, these plots omit the central parts of the sample where the strains are very small. It is apparent from Fig. 2.3c that Eq. (2.6) describes a smooth increase in the total strain with increasing numbers of whole revolutions and identical trends pertain also to Eqs (2.4), (2.5), and (2.7). In practice, a more accurate evaluation of the total strain stored within the disk during HPT requires the use of finite element methods [35].

Three distinct types of HPT processing [36] are illustrated schematically in Fig. 2.4: these types are termed (a,b) constrained and (c) unconstrained HPT, respectively. In constrained HPT, the disk is machined to fit into a cavity in the lower anvil and the load is applied so that, in principle at least, there is no outward flow of material under the application of a high load. Constrained HPT is therefore conducted in the presence of a back-pressure. In practice, however, it is difficult to achieve an idealized constrained condition and there is generally at least some limited flow between the upper and lower anvils. In unconstrained HPT, the specimen is free to flow outwards under the applied pressure and little or no back-pressure is introduced into the system.

2.2. Ball milling and cold consolidation by means of HPT

Mechanical alloying (MA), first developed in the 1960s, is a high energy ball milling process [37-39]. An initial blend of powders is repeatedly kneaded together and re-fractured by the action of the ball-powder collisions until a powder is produced in which each particle has the composition of the initial powder blend. The extremely fine grain sizes generated during MA as well as the ability to produce a variety of non-equilibrium phases ranging from supersaturated solid solution to nanocrystalline and/or amorphous phases, may offer a means of improving ductility and providing a better balance of properties in challenging new materials, such as intermetallic compounds. Since the process takes place entirely in the solid state, it is also possible to produce new alloys from virtually immiscible components. Alternatively the MA process can be used to distribute a second phase homogeneously throughout a chosen matrix to produce a particulate reinforced metal matrix composite (MMC). Unlike other methods (phase gas composition, electrodeposition), mechanical alloying/ball milling (MA/BM) produces nanostructured materials not by cluster assembling but by structural decomposition of coarse-grained structures as the result of heavy plastic deformation. This makes the BM technique similar to several plastic deformation techniques developed in [4]. Ball milling has become a widely used method to synthesize nanocrystalline materials because of its simplicity, the relatively inexpensive equipment and the applicability to essentially all classes of materials. Nevertheless, some serious problems are usually cited: contamination from milling media and/or milling atmosphere and the need to consolidate the powder product while maintaining the nanostructured feature of the material.

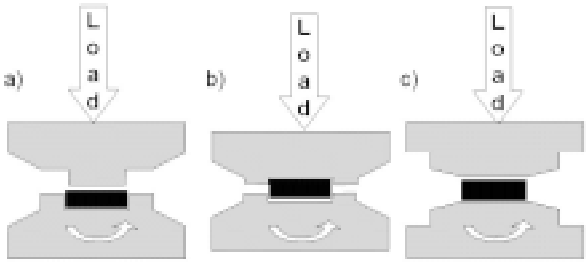

Fig. 2.4. Principles of HPT for (a, b) constrained and (c) unconstrained conditions.

In the present work, a planetary mill has been utilized for producing powder of metals and alloys. This mill, also known as centrifugal mill, is a device used to rapidly grind materials to colloidal fineness (approximately 1 micron and below) by developing high grinding energy via centrifugal and/or planetary action. Each vial sits on an independent rotable platform, and the entire assembly is also rotated in a direction opposite to the direction of the vial platform rotation. In planetary action, centrifugal forces alternately add and subtract. The grinding balls roll halfway around the bowls and then are thrown across the vials, impacting on the opposite walls at high speed. Grinding is further intensified by interaction of the balls and sample.

As was mentioned above, the consolidation of powder while maintaining the nanostructure is one of the major problems of ball milling. High-pressure torsion and equal-channel angular pressing can be used for this purpose. HPT is especially suitable because of the high pressure imposed. Ball milled powder as well as amorphous ribbons were used in the present study in order to fabricate bulk nanocrystalline (partially amorphous) samples.

3. MICROSTRUCTURE CHARACTERISTICS OF BALL MILLED MATERIALS CONSOLIDATED BY HIGH PRESSURE TORSION

3.1. Microstructural effects and large microhardness in cobalt processed by HPT consolidation of ball milled powders

Extensive research has been carried out during the last decades on the allotropic phase transformations of cobalt [40-42]. This metal undergoes a phase transition, from hexagonal closed packed (HCP) to lattice to face-centered cubic (FCC) lattice, when it is heated above the thermodynamic equilibrium temperature, T_t = 695K. In spite of its apparent simplicity, several specific features make this phase change particularly worth studying. For instance, the average transformation enthalpy has been found to be different when heating (473 $J \cdot mol^{-1}$) or cooling (352 $J \cdot mol^{-1}$), which implies that a considerable thermal hysteresis exists in the transformation [43]. Moreover, T_t can be significantly lowered by applying high hydrostatic pressure [44]. In addition, pure fcc-Co has been obtained at room temperature (well below T_t) in particles of nanometric sizes [45-47] or after a high-energy ball milling process [48]. In fact, since hcp and fcc are both close packed structures, stacking faults usually play a key role in all the models describing the transformation, either when it is thermally activated or induced by a cold-work process [40-42].

Among the traditional routes for plastic deformation, ball milling has become a widespread technique for the processing of equilibrium and non-equilibrium powder materials [49]. Moreover, in recent years, growing interest has emerged in bulk nanocrystalline materials processed by severe plastic deformation techniques, such as high pressure torsion or equal channel angular pressing [4,50]. The resultant materials often exhibit novel and unique properties, such as high strength and wear resistance or a high strain-rate superplasticity [8,24]. All these phenomena mainly originate from the significant grain size refinement accompanying severe plastic deformation. The understanding of the microstructure evolution during plastic deformation methods is of great importance for the advancement of the applications of this type of materials.

In this study, cobalt powders have been processed by a combination of two different techniques of plastic deformation: ball milling and high pressure torsion. Long-term milling and HPT result in similar crystallite size refinement. However, the foils obtained after both processing routes are composed of a two-phase mixture (hcp + fcc), with large amounts of stacking faults, especially of twin-type. Interestingly, the foils, which are virtually free of porosity, exhibit large microhardness values (H_v in excess of 7.3 GPa). Both grain boundaries and twin faults, which impose barriers for dislocation motion, may be responsible for the large strain hardening.

Co powders (99.5%, 325 mesh, from Alfa-Aesar ®) were mechanically milled in a planetary ball mill (*Fritsch Pulverissette* 7), at 500 rpm, during times ranging from 0.5 to 45 h, using agate vials and balls, in a ball-to-powder weight ratio of 10:1. The vials were previously sealed under argon atmosphere to prevent oxidation. The unmilled and ball milled (BM) powders were subsequently consolidated by means of a HPT process, using a modified *Bridgman* anvil type device [51]. Several foils were prepared, each corresponding to a different milling time, by subjecting pre-compacted as-milled powders to a 5 whole-turn torsion under an applied pressure of 6 GPa.

High-resolution transmission electron microscopy (HRTEM) observations were carried out on a foil processed by BM during 20 h and subsequent HPT, using a Jeol 4000EX microscope operating at 400 kV. The specimen preparation procedure consisted of conventional mechanical polishing until thickness of 40 μm followed by Ar ion milling using a Gatan PIPS with small incident angle, allowing large thin and homogeneous areas to be obtained.

X-ray diffraction (XRD) experiments, using Cu-K_α radiation, were performed both in as-milled (pre-compacted) powders and in foils obtained after HPT. Microstructural parameters (cell parameters, crystallite sizes, microstrains, stacking fault probabilities and phase percentages) were quantified by means of the recently developed XRD data analysis software *Materials Analysis Using Diffraction* (MAUD), which is based on a full pattern fitting procedure (Rietveld method) [52-54]. The whole experimental XRD pattern is modeled using pseudo-Voigt functions, whose intensities depend on the structure of the phases present in the specimen [55]. Crystallite sizes and microstrains are determined from the angular dependence of the Cauchy and Gaussian components of the half-width at half-maxima (HWHM) of the diffraction peaks, following the Delft model [53]. The program also allows calculating stacking faults probabilities. This is carried

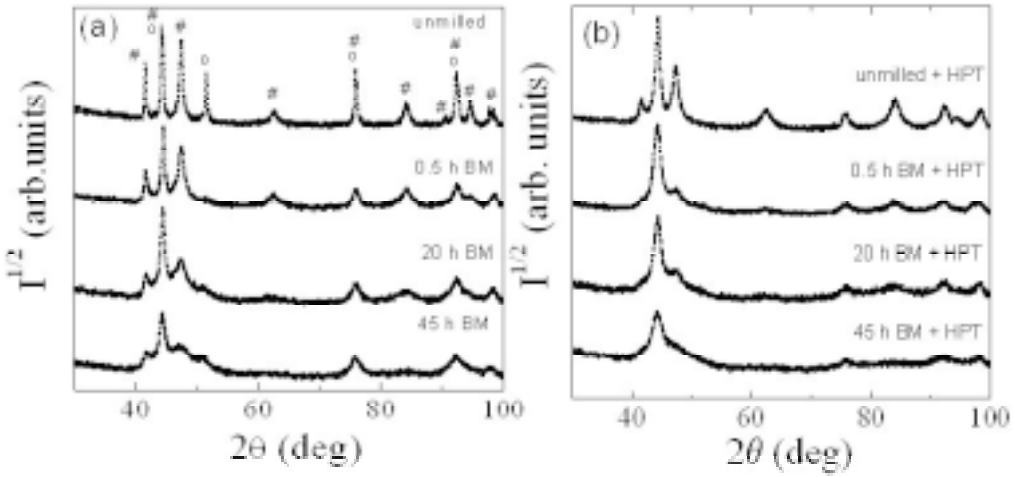

Fig. 3.1. (a) XRD patterns of Co before milling and after ball milling (BM) for 0.5, 20 and 45 h. (b) XRD patterns obtained after subjecting to high pressure torsion (HPT) unmilled Co powders and Co milled for 0.5, 20 and 45 h. The symbols # and o denote the hcp and fcc phases, respectively.

out according to Warren's formulae, from where two types of faults, namely twin and deformation faults can be quantified [56].

The Vickers microhardness of the HPT foils was measured at half the radius of the disks by means of a MHT-10 tester attached on a Zeiss Axioplan optical microscope, using a load slope of 0.2 N/s. Sufficient hardness measurements were carried out to ensure standard deviations below 5%. It is well known that reliable values of microhardness require the material to be thick enough and free of porosity [24]. Since these conditions cannot be entirely ensured in as-milled powders, the microhardness was only measured in HPT foils.

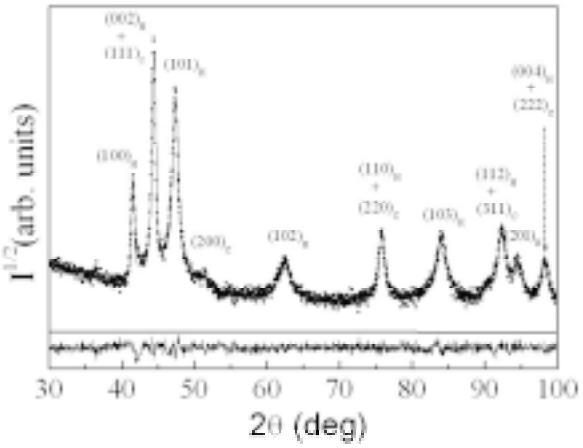

Fig. 3.2. XRD pattern of Co milled for 0.5 h together with the curve generated from the full-pattern fitting procedure and the corresponding difference between the calculated and the experimental profiles. The Miller indexes have also been indicated in the figure. Note that H and C denote the hcp and fcc phases, respectively.

Fig. 3.1 shows the XRD patterns of unmilled Co and Co milled for 0.5, 20 and 45 h, before (a) and after (b) HPT. Fig. 3.2 shows the XRD pattern of the 0.5 h BM Co powders, together with the curve generated by the full-pattern fitting procedure and the corresponding difference between the calculated and the experimental profiles. It can be seen that the XRD pattern can be very well fitted using the Rietveld method. The Miller indexes of the different peaks are also indicated in Fig. 3.2. In Fig. 3.1a it can be seen that the starting Co is a mixture of hcp and fcc phases (note that the symbols # and O denote the hcp and fcc phases, respectively). The fcc-Co is probably retained from the gas-atomization process used to synthesize the starting Co powders. The amount of fcc rapidly reduces with milling time. This is evidenced by the large decrease in intensity of the $(200)_C$ peak after 0.5 h of milling. However, as milling time further increases, a wide hump appears at the position of this peak, indicating that fcc-Co is somewhat recovered. Conversely, when the unmilled powders are subjected to HPT, the fcc-Co transforms almost completely into hcp-Co (see Fig. 3.1b). Moreover, this transformation persists, although not so efficiently, when HPT is applied to already ball-milled powders.

The milling time dependencies of the hcp-Co weight percentage, before and after HPT, are shown

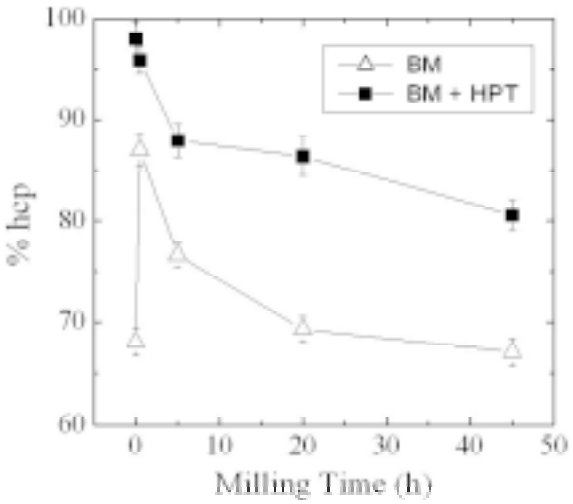

Fig. 3.3. Milling time dependencies of the hcp weight percentage for as-milled (pre-compacted) Co powders (-Δ-) and powders ball milled (BM) and consolidated by HPT (-■-). The lines are guides to the eye.

in Fig. 3.3. A maximum hpc content is observed in both cases for short milling times and a two-phase mixture is observed afterwards. However, hcp-Co always remains the predominant phase, especially after HPT. Remarkably, HPT on the unmilled samples results in an almost 100 % hcp structure.

Also worth mentioning is that a widening of the diffraction peaks is observed as milling time increases and, even more remarkably, after BM + HPT. This is due to the crystallite size refinement and the increase of microstrains associated with both processing routes. The dependence of the crystallite size of the hcp phase, $\langle D \rangle_H$, on the milling time, before and after HPT, is shown in Fig. 3.5. Due to the exceedingly small amount of fcc after HPT, the values of the crystallite size and microstrains for fcc-Co cannot be reliably determined for all milling times, although $\langle D \rangle_C$ is estimated to be of around 3 nm after long-term milling + HPT. It can be seen that, in as-milled powders, $\langle D \rangle_H$ decreases progressively with milling time, reaching a minimum value of 8.7 nm after milling for 45 h. HPT on the unmilled powders results in $\langle D \rangle_H$ = 12 nm, i.e. similar to the one obtained after 20 h of milling. However, HPT becomes very effective in terms of crystallite size refinement when carried out in the milled powders. This is already evident from the XRD peak widths shown in Fig. 3.1. It is remarkable that when the 45 h as-milled powders are subjected to HPT, $\langle D \rangle_H$ becomes extremely small, of the order of 3.5 nm, indicating that Co is close to amorphization.

The high resolution transmission electron microscopy image of a thinned Co foil obtained by BM during 20 h and subsequent HPT is shown in Fig. 3.4. It can be seen that the specimen is composed of very small crystallites, oriented in different directions and well soldered together. A detailed examination reveals that the sample is free of porosity, i.e. fully dense, hence exhibiting a bulk character. It is worth noting that the crystallites are irregular in shape and size, most of them attaining sizes of less than 10 nm. Due to these reduced dimensions, the crystallites are often overlapped when they are observed by HRTEM, thus making it very difficult to perform a quantitative study of the type and amount of stacking faults. Hence, this quantification was not attempted by HRTEM, but was performed from the Rietveld analyses of the XRD patterns. It is noteworthy that, according to XRD results, in Co milled for 20 h subsequently subjected to HPT, $\langle D \rangle_H$ is of the order of 7 nm, which is only slightly smaller than the values observed by HRTEM. The small discrepancies could arise from the disordered character of the grain boundaries, which could decrease the coherence length and thus the crystallite size, as determined by XRD.

The milling time dependence of the microstrains in the hcp phase, $\langle \varepsilon^2 \rangle^{1/2}_H$, is shown in the inset of Fig. 3.5. It is found that microstrains in the hcp phase increase slightly after subjecting as-milled powders to HPT. Hence, our results indicate that, although both $\langle D \rangle_H$ and $\langle \varepsilon^2 \rangle^{1/2}_H$ tend to level off after long-term milling, further structural refinement can be achieved by the application of the HPT process.

The dependencies of stacking fault probabilities for the hcp phase, before and after HPT are shown in Figs. 3.6a and 3.6b. According to Warren's description of stacking faults, two types of faults can be distinguished [56], i.e. deformation fault and twin faults, whose probabilities are denoted in Fig. 3.6 as α_H and β_H, respectively. These faults bring about different alterations of the stacking sequence of compacted atomic planes. In undistorted hcp the stacking sequence can be represented by …ABABABAB… (where A and B designate compacted atomic planes along the $\{001\}_H$ direction). A deformation fault in hcp originates from dissociation into Shockley partial dislocations of basal slip along the close-packed $\langle 110 \rangle_H$ directions, leading to the …AB**ABCA**CA… sequence. A twin fault occurs as a result of formation of twin boundaries and the generated sequence is …AB**ABC**BCB… Both faults bring about the formation of local fcc packing,

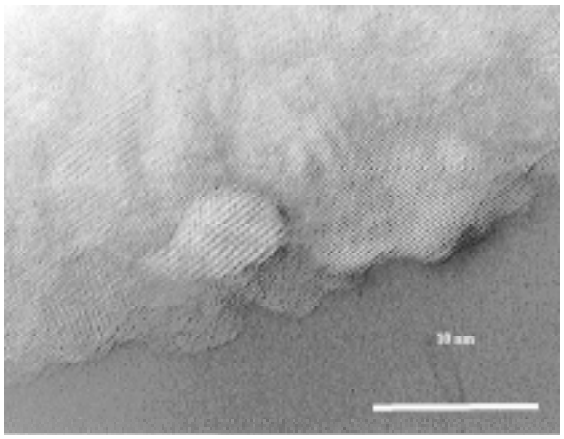

Fig. 3.4. HRTEM image of a thinned Co foil prepared by ball milling Co powders during 20 h and consolidation by HPT.

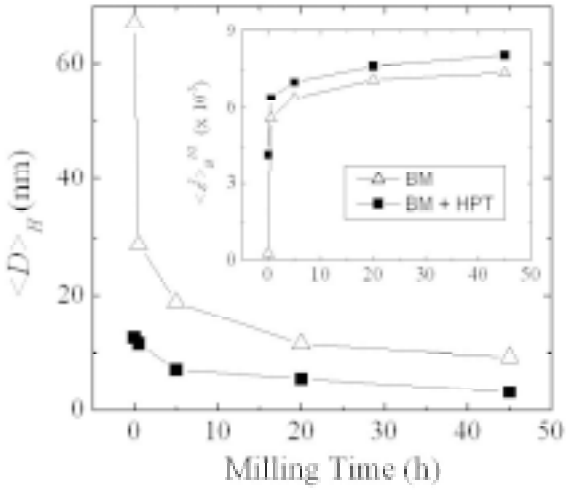

Fig. 3.5. Milling time dependencies of the hcp crystallite size for as-milled (pre-compacted) Co powders (-Δ-) and powders ball milled (BM) and consolidated by HPT (-■-). In the inset, milling time dependencies of the microstrains in the hcp phase. Note that the lines are guides to the eye.

as indicated by the bold letters. As can be seen in Fig. 3.6, the amounts of stacking faults increase with milling time. However, while for BM alone twin faults are predominant, after BM+HPT deformation faults prevail.

Finally, the Vickers microhardness, H_V, is plotted in Fig. 3.7 as a function of the inverse of the square root of the crystallite size in the hcp phase (i.e. the predominant phase), $(\langle D\rangle_H)^{-1/2}$. As shown in the figure, the increase of microstrains with $(\langle D\rangle_H)^{-1/2}$ is non-monotonic and a change of slope is evident for intermediate crystallite sizes ($\langle D\rangle_H \approx 6$ nm).

As is shown in Fig. 3.3, long-term ball milling favors the formation of fcc-Co, whereas HPT favors hcp-Co. The Co allotropic phase transformations occurring during BM have been studied in certain detail recently [48,57-60]. In particular, it has been found that a mechanism of accumulation and coalescence of twin faults in the hcp phase governs the formation of fcc-Co after long-term milling. The milling intensity (i.e. vial frequency or ball-to-powder weight ratio) can be adjusted to tune the evolution of the phase change [48,60]. In addition, the transformation from the metastable high-temperature fcc phase to the low-temperature hcp phase by means of application of moderate pressures has been already reported and has been found to be related to stacking fault activity [61]. Nevertheless, when Co is subjected to extremely large pressures the hcp phase tends to transform to fcc again [62]. However, this occurs for pressures of the order of 100 GPa, much larger than the ones applied in the present work. In particular, the transformation from fcc to hcp-Co, induced by either cooling through T_t

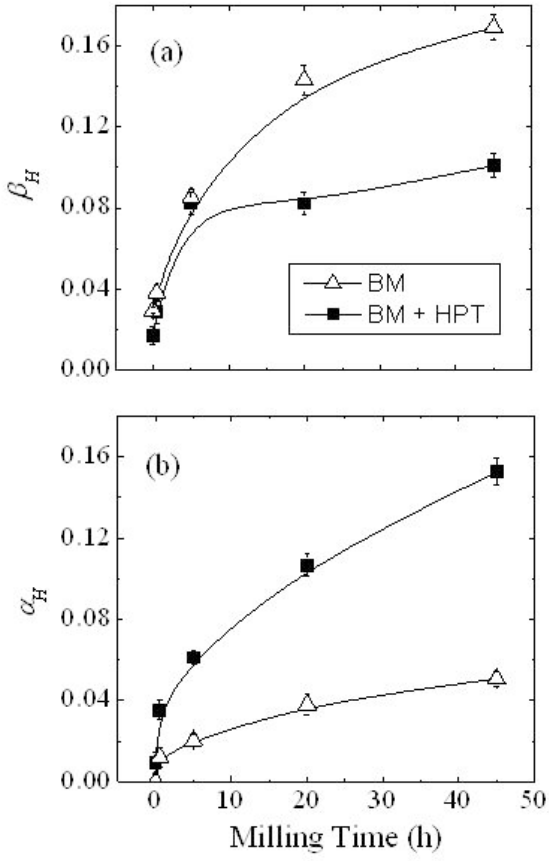

Fig. 3.6. Milling time dependencies of (a) the twin fault probability (for the hcp phase), β_H , and (b) the deformation fault probability, α_H, in as-milled powders (-Δ-) and powders ball milled (BM) and subsequently consolidated by HPT (-■-). The lines are guides to the eye.

or by cold-work (i.e. external pressure), is commonly assumed to occur by the passage of 1/6 <11-2> Shockley partial dislocations on alternate $\{111\}_C$ planes [63,64]. It is noteworthy that, although the small percentage of fcc-Co retained after HPT makes it impossible to estimate the fault probabilities in this phase, an increase of deformation fault probability in fcc-Co, α_C, has been observed during short-term milling (from $\alpha_C \sim 0$ in unmilled Co to $\alpha_C = 0.05$ after milling for 0.5 h), and has been related to the form ation of Shockley partial dislocations and the subsequent transformation of fcc into hcp-Co during the first stages of the milling process [59].

As can be seen in Fig. 3.6 fractions of both types of faults in hcp-Co, deformation and twin, increase with milling time. However, in as-milled powders, twin faults prevail over deformation faults, especially after long-term milling. This is mainly due to the randomness of the shock loads acting during the milling process, together with the limited number of slip systems in hcp materials [65]. Conversely, after application of HPT, large amounts of deformation faults are created at the expense of twin faults, which is in agreement with the partial Shockley dislocations driven transformation of fcc into hcp-Co by cold work [63,64].

A constitutive description of the onset of twinning in hcp metals has been reported recently by Meyers *et al.* [66]. In particular, it has been theoretically shown that both the critical stress for twinning and the yield stress for slip depend on the crystallite size. However, the stress required to generate twinning increases more rapidly than the yield stress for slip as crystallite size is reduced. Moreover, it has been found experimentally that in 70/30 brass, Ni-Co based alloys or Cu the density of microtwins for small crystallite sizes is significantly lower than for larger crystallite sizes [67,68]. Hence, it could be argued that during HPT, since the crystallite size is drastically reduced, the stress required to generate twinning increases so much that twinning becomes, in fact, unfavorable, compared to slip, hence leading to an increase in α_H at the expense of β_H. Moreover, a disappearance of multi-twins has also been reported in Au nanoparticles as their size becomes extremely small [69], which has been interpreted in terms of atomic rearrangement along certain preferential crystallographic directions. Furthermore, it has also been reported that, in hcp-Co crystals, for certain values of shear stresses applied along the c-axis it is energetically favorable that partial annihilation of twins develops, due to the large stress-induced bending of the basal planes

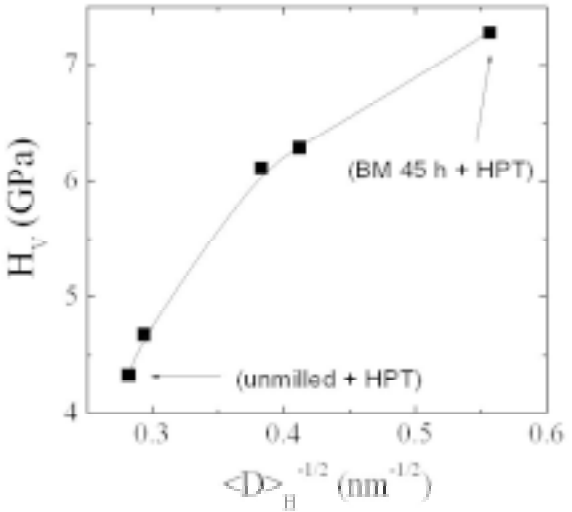

Fig. 3.7. Dependence of the Vickers microhardness, H_V, on the inverse square root of the hcp crystallite size, $\langle D \rangle_H^{-1/2}$, measured on foils prepared by BM + HPT. The line is a guide to the eye. Note that the Hall-Petch relationship (i.e. linear variation of H_V on $\langle D \rangle_H^{-1/2}$) is not exactly fulfilled.

[70]. In our case, since as-milled Co powders are polycrystalline it is reasonable to assume that, during HPT, a fraction of crystallites are oriented in such a way that partial annihilation of twins can actually occur, thus leading to the observed decrease of α_H.

Furthermore, some models also argue that pre-existing twin or grain boundaries can provide, in a regenerative manner, Shockley partial dislocations which would induce the change in stacking sequence required to drive the fcc to hcp transformation during HPT [71,72]. Nevertheless, it should be noted that in order for the transformation to be complete, a non-random arrangement of deformation faults should occur, preferably at two-layer separation. Since the Co microstructure is already heavily and randomly faulted after long-term milling, it is unlikely that HPT can completely rearrange stacking faults to drive a full transformation from fcc to hcp Co. Hence, the resultant hcp phase contains large amounts of deformation-type stacking faults and some fcc-Co still persists after HPT, especially when HPT is applied to long-term milled powders.

As it is observed in Fig. 3.7, high values of H_V, up to 7.35 GPa, are obtained after subjecting long-term milled powders to HPT. This value is much larger than the microhardness reported in Co films deposited onto Cu substrates [73], larger than the ones in several Co-based alloys [73,74] and about

80% of H_V of Co/WC cermet nanocomposites, which are being widely used in wear resistance applications [75]. Usually, in single-phase polycrystalline materials, a linear variation of H_V on $(<D>_H)^{-1/2}$ is expected, leading to the so-called Hall-Petch relationship [65]. This relationship originates from considering the role of grain boundaries as barriers for dislocation motion. Typically, the yield stress necessary for slip becomes larger as the crystallite size reduces and, hence, H_V increases. Nevertheless, as can be seen in Fig. 3.7, in Co subjected to BM + HPT, the dependence of H_V on $<D>_H^{-1/2}$ is not exactly linear. More accurately, the rate of increase of H_V is very high for large crystallite sizes (i.e. short-term milling) and it becomes lower as milling time is further increased. Actually, in extremely fine-grained materials a certain softening is sometimes observed due to the impossibility to form pileups of dislocations when the crystallites become exceedingly small [76]. In fact, it has been suggested recently that for nanocrystalline materials, the Hall-Petch model may not be fully operative and other mechanisms, such as Coble creep or grain boundary diffusional creep, would better govern the dependence of microhardness on the crystallite size [77]. Moreover, in addition to grain boundary strengthening, other hardening mechanisms may also be simultaneously acting during plastic deformation of Co particles. For instance, twin boundaries can be thought to subdivide the grains and therefore increase the barriers for slip. Actually, twin boundaries are a particular case of grain boundaries with a low index of coincidence. The idea of whether twins can play a similar role as grain boundaries during work hardening of metals with low stacking fault energy (such as Co) was originally suggested by Remy [78] and has been recently studied from both theoretical [79] and experimental [80] points of view. In particular, it has been shown that the increase of the twin volume fraction leads to a decrease in the dislocation mobility [79,80]. However, in polycrystals where both grain and twin boundaries coexist, grain boundaries still constitute stronger barriers for dislocation motion than twin boundaries. This is because dislocations can dissociate and penetrate relatively easily into the twinned region, whereas at grain boundaries a significant pile-up of dislocations is required before slip in successive neighboring grains can occur [80]. As has been shown in Fig. 3.6b the twin fault probability in HPT foils increases steeply for short milling times and tends to level off for longer milling times. This may explain why H_v increases at an anomalous high rate for short-term milling (i.e. low $<D>_H^{-1/2}$ values).

In conclusion, a correlation between microstructure and mechanical properties (i.e. microhardness) of Co foils prepared by ball milling and subsequent high pressure torsion has been presented. The crystallite size is found to be significantly reduced after HPT, much further than by subjecting Co powders to a long-term milling process alone. Simultaneously, large amounts of stacking faults, especially deformation faults, are created during HPT. This is in contrast with BM, where the twin fault probability is significantly larger than the deformation fault probability. Possible mechanisms to explain these differences in the fault behavior have been discussed. Furthermore, besides the large amount of structural defects, a two-phase mixture (i.e. hcp + fcc) develops during long-term milling and still persists after HPT. All these structural features seem to have an influence on the microhardness, which becomes very large after long-term milling + HPT (i.e. H_V > 7.3 MPa). It has been shown that the dependence of H_V on the crystallite size of the predominant phase (i.e. hcp) does not strictly follow the Hall-Petch relationship. Hence, although the crystallite size refinement is probably the main factor governing the increase of H_V, other structural features, such as the stacking fault accumulation and the associated hcp-fcc transformation, are also likely to contribute to H_V.

3.2. Cold-consolidation of ball-milled Fe-based amorphous ribbons

Amorphous alloys are attaining widespread applications as soft ferromagnets (in transformers, motors or as high-frequency switching power supplies) and as high strength and high corrosion resistance materials [81]. However, before 1990, the shapes of these alloys were limited mainly to wires, thin films, powders or ribbons. Moreover, the preparation of sheets with thickness over 100 mm is generally very difficult due to the high cooling rates required for glass formation. In particular, Fe-based amorphous alloys with good soft magnetic properties were first synthesized in the early 70's [82,83]. During the last two decades, several multi-component glassy alloys with a wide supercooled liquid region have been also prepared [84-87] from which, due to their high resistance against crystallization, bulk glassy samples can be obtained by using conventional mold casting methods [88,89]. However, the majority of these alloys are not ferromagnetic. Nevertheless, it has been recently found that the Fe-Al-P-C-B-Ga system exhibits, simultaneously, good soft magnetic properties at room temperature and an ex-

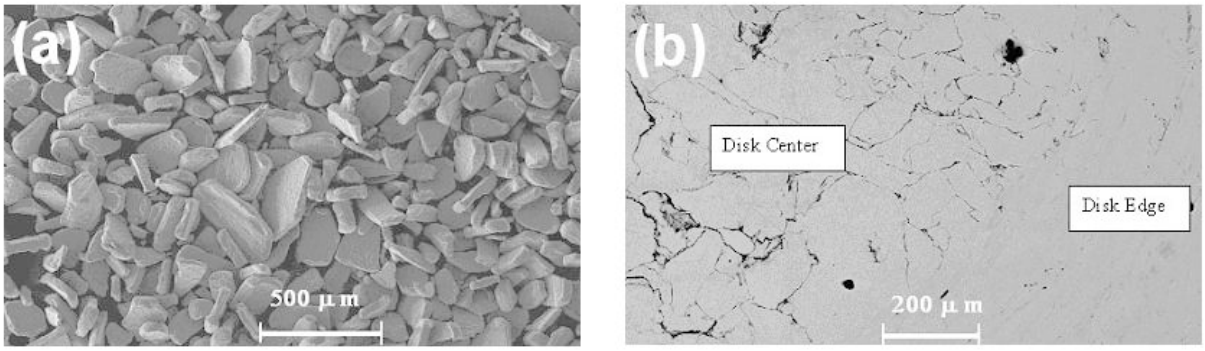

Fig. 3.8. Scanning electron microscopy images of (a) flaky powders after ball milling of the $Fe_{77}Al_{2.14}Ga_{0.86}P_{8.4}C_5B_4Si_{2.6}$ ribbons and (b) a portion of a disk obtained by HPT of the as-milled powders.

tended supercooled liquid region [90]. The addition of Si further enhances its glass forming ability [91].

It is noteworthy that in order to obtain bulk metallic glasses one standard procedure is to consolidate amorphous powders in the supercooled liquid region (i.e. between the glass transition temperature, *Tg*, and the temperature corresponding to the onset of crystallization, *Tx*). This is carried out by powder metallurgy techniques (e.g., hot pressing or warm extrusion). At this temperature range, the viscous flow allows the formation of the bulk metallic glass without crystallization [92,93]. However, this procedure is not always appropriate because these techniques require the powder to be held at elevated temperatures for relatively long times, hence leading, in many cases, to a loss of some metastable properties. Moreover, the hot-compaction is limited to those alloy compositions which exhibit large supercooled liquid regions.

In our work a different approach is considered. Amorphous ribbons with the nominal composition $Fe_{77}Al_{2.14}Ga_{0.86}P_{8.4}C_5B_4Si_{2.6}$ have been short-term ball-milled and subsequently consolidated by high pressure torsion. This technique is commonly used to refine the crystallite size in crystalline materials [4,50,94], to tune phase transformations [95] or to obtain novel and unique properties, such as high strength and wear resistance or high strain-rate superplasticity [8]. High pressure torsion can be considered as a cold consolidation technique because the consolidation of the powders is carried out without external heating and the temperature basically does not increase during the torsion process. In our case, the disks obtained after HPT partially preserve the amorphous nature of the ribbons and exhibit enhanced Curie temperature and microhardness.

A multi-component prealloy with nominal composition $Fe_{77}Al_{2.14}Ga_{0.86}P_{8.4}C_5B_4Si_{2.6}$ was prepared by induction melting of a mixture of Fe, Al, Si metals and Fe-C, Fe-B, Fe-P and Fe-Ga (purity 99.9%) precursors. From this prealloy, rapidly quenched ribbons with cross-section of about 0.02×10 mm^2 were prepared by single roller melt spinning. Some parts of the ribbons were subsequently cut into small pieces and ball milled for 10 h, under argon atmosphere, in a planetary mill using agate vials and balls. The as-milled powders were sieved and those with sizes less than 300 μm were subsequently consolidated by means of a HPT process, using a modified Bridgman anvil type device [51]. Several disks, of approximately 9 mm in diameter and 0.3 mm in thickness were prepared by subjecting the powders to five whole-turn torsion under an applied pressure of 6 GPa.

The melt-spun ribbons and the foils prepared by HPT were examined by X-ray diffraction using Cu-K_α radiation. Moreover, the samples were microscopically investigated using a JEOL JSM-6300 scanning electron microscope (SEM) and a Philips CM20 transmission electron microscope (TEM), operated at 200 keV. For TEM observations, the disks were cut into thin slices and some parts (i.e., those corresponding to the disk edges) were dimpled and ion milled using a Gatan Precision Ion Polishing System (PIPS).

The thermal stability was studied by DSC using a Perkin-Elmer calorimeter and a heating rate dT/dt = 20 K/min. The Curie temperatures were evaluated by means of a thermomagnetic gravimeter (TMG), where the magnetic weights of the ribbon and the disks were measured during heating, at a rate dT/dt = 20 K/min, from T = 300K to T = 1100K, apply-

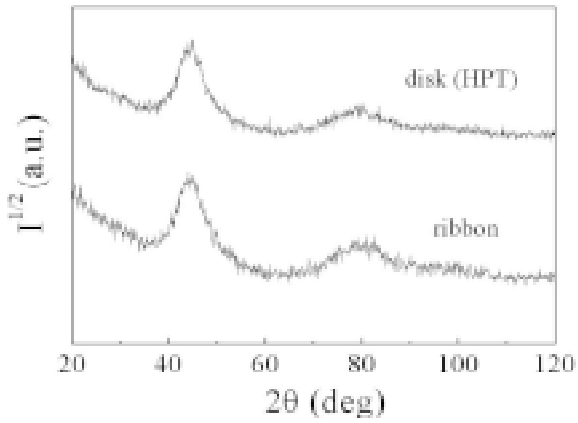

Fig. 3.9. X-ray diffraction patterns of the $Fe_{77}Al_{2.14}Ga_{0.86}P_{8.4}C_5B_4Si_{2.6}$ ribbon and disk prepared by HPT.

ing a magnetic field H = 9500 A/m. The coercivities of the ribbons and the disks were measured by means of a Foerster coercivemeter. Finally, the Vickers microhardness, H_V, was evaluated by means of a MHT-10 indenter attached on a Zeiss Axioplan optical microscope. Sufficient hardness measurements were carried out to ensure standard deviations below 5%.

Note that, in the disks, all these properties were essentially measured at their edges, where the HPT process is more effective in obtaining bulk specimens of compacted powders.

Fig. 3.8 shows the SEM images of (a) the powders obtained after ball-milling the $Fe_{77}Al_{2.14}Ga_{0.86}P_{8.4}C_5B_4Si_{2.6}$ ribbons and (b) an overall view of the outer morphology of the compacts produced by consolidation of the as-milled powders by HPT.

It can be seen that the as-milled powders exhibit flaky shapes and lateral sizes of a few hundred micrometers. This is the typical morphology of ribbons subjected to a ball milling process [96]. After consolidation by HPT, the powders become well soldered together and the disks are almost fully dense, hence exhibiting a bulk character. Actually, two different parts can be well distinguished in the disks: the central region, in which some traces of the as-milled particles are still visible at the surface of the disks, and the edge, which exhibits better homogeneity due to the more effective radial shear flow acting during torsion straining (see Fig. 3.8b).

Fig. 3.9 shows the XRD patterns of the ribbon and the edge of the disk prepared by HPT. Both of them consist of broad halos without any sharp diffraction peaks, indicating that no massive crystallization occurred either during ball milling or during HPT.

The bright field TEM images and the corresponding selected-area electron diffraction (SAED) patterns of both a part of the ribbon and a portion of the disk edge are shown in Figs. 3.10a and 3.10b, respectively. The amorphous nature of the ribbon is clearly evidenced by the featureless contrast of the bright field image and the existence of halo rings in the corresponding SAED pattern. However, the TEM image of the disk reveals that, although no crystalline peaks were observed by XRD, a few dispersed nanocrystallites (with sizes generally less than 5 nm) are formed during ball milling and subsequent HPT. The corresponding SAED pattern shows the presence of some rings besides the amorphous halos. These rings, typical of polycrystalline mate-

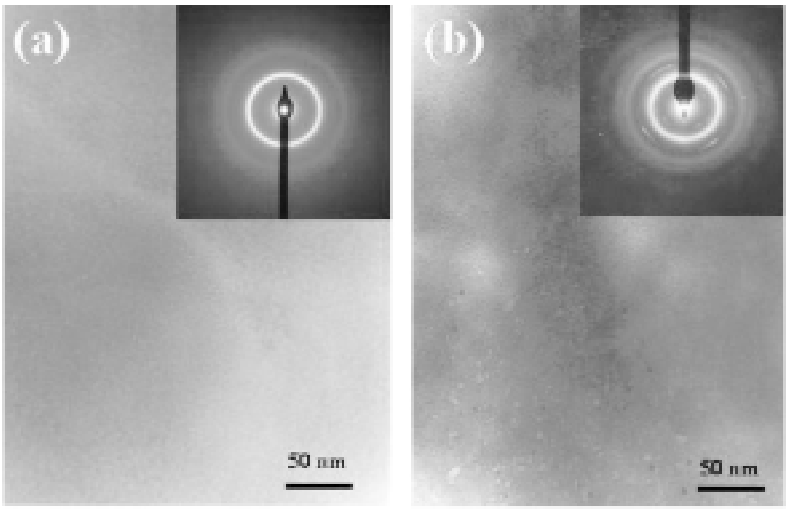

Fig. 3.10. Bright-field electron microscopy images and corresponding selected-area electron diffraction patterns of the $Fe_{77}Al_{2.14}Ga_{0.86}P_{8.4}C_5B_4Si_{2.6}$ ribbon (a) and disk prepared by HPT (b).

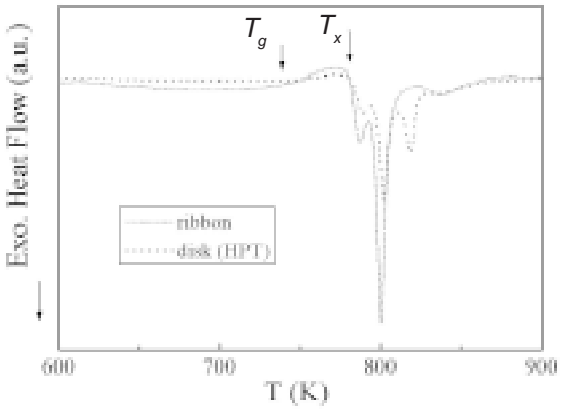

Fig. 3.11. Continuous heating DSC curves (heating rate *dT*/*dt* = 20 K/min) of the ribbon and HPT disk (*Tg* and *Tx* are the glass transition temperature and the temperature of crystallization of the ribbons, respectively).

rials, have been identified to correspond to the tetragonal Fe_2B phase.

One cannot completely disregard the possibility that some α-Fe nanocrystals could also be present since, in this case, the main crystalline rings would appear exactly at the same radius as the amorphous rings. Moreover, due to the discontinuity of the crystalline rings, some texture can be inferred in the nanocrystals nucleated during HPT. It is worth mentioning that, as can be seen in Fig. 3.10b, all these crystallites are immersed in a majority amorphous matrix. The formation of dispersed crystallites could be a consequence of the significant changes that HPT is likely to impose on the short-range order of the amorphous alloy.

Fig. 3.11 shows the DSC curves of the $Fe_{77}Al_{2.14}Ga_{0.86}P_{8.4}C_5B_4Si_{2.6}$ ribbon and the disk prepared by HPT. The crystallization behavior is different in both cases (both the shape of all the peaks and the position of one of them vary), suggesting that changes in both the topological and chemical short-range order of the alloy may have occurred during the HPT process. Moreover, the overall crystallization enthalpy in case of the disks is lower than for the ribbons (i.e. ΔH = 138 J/g for the ribbons whereas ΔH = 90 J/g for the disks), indicating that the disks are already partially nanocrystalline, as has been observed by TEM. It should be also noted that the supercooled liquid region of the ribbons ($\Delta T = T_x - T_g$) is approximately 40K, which is in agreement with the results on samples with similar compositions [91].

Fig. 3.12 shows the TMG curves of the ribbon (before and after ball milling) and the edge of the disk. The disks obtained by HPT exhibit a slightly higher Curie temperature (i.e., T_C = 620K) than the unmilled ribbons (i.e., T_C = 600K). The T_C enhancement is likely to originate from irreversible changes in the chemical short-range order occurring during ball milling and HPT processes, since T_C is directly related to the exchange energy between magnetic atoms [97,98]. Moreover, the magnetic weight of the unmilled ribbon virtually vanishes at $T \sim$ 620K, whereas that of the disk levels off at a finite value and starts to increase progressively for $T >$ 620K. The fact that the magnetic weight does not vanish for the disk is a consequence of the existence of the Fe_2B (and maybe also α-Fe) nanocrystals in the as-prepared disks, since both phases are ferromagnetic at room temperature. The progressive increase in the magnetic weight that occurs in the disk for $T >$ 620K is probably due to the growth of the Fe_2B (and maybe α-Fe) crystallites nucleated during the HPT process. In addition, the TMG curves in Fig. 3.12 show a sudden increase in the magnetic weight at about T = 790K.

This can be attributed to the crystallization of a mixture of other ferromagnetic phases (such as α-Fe or Fe_3B), as has been indeed observed by XRD [99]. Finally, the magnetic weight becomes zero for high enough temperatures. Note that the Curie temperatures of Fe_2B and α-Fe (T_C of Fe_2B = 1015K, T_C of α-Fe = 1043K) are somewhat larger than the temperature at which the magnetic weight vanishes in the disk (T = 980K). This reduction in Curie temperatures can be due to the small sizes of the crystallites and the concomitant increase of thermally-induced magnetic fluctuations (i.e., finite size effects) [100].

Moreover, the saturation magnetization of the disks is found to be similar to that of the ribbons ($M_S \sim$ 150 emu/g in both cases), while the coercivity, H_C, increases significantly for the as-prepared disks (H_C = 188 A/m at the disk edge) with respect to the ribbons (H_C = 3 A/m). The increase in H_C is probably due to the structural inhomogeneities (e.g. irregularities in the surface of the particles) induced by ball milling and subsequent HPT, which hinder the magnetic domain wall propagation, although some effects due to oxygen contamination cannot be completely excluded as being partially responsible for the H_C increase [101]. However, it should be noted that after short-term annealing (600 s at T = 700K), the disks relax and recover low values of coercivity (H_C = 25 A/m at the disk edge), hence

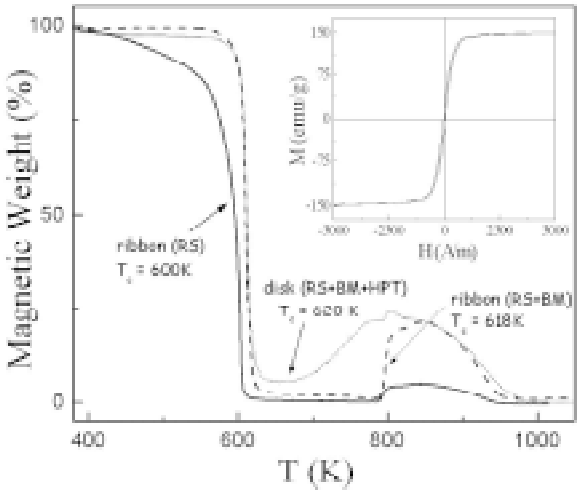

Fig.3.12. TMG curves of the rapidly solidified (RS) ribbon, the ball milled (BM) ribbon and the edge of the disk prepared by HPT. The inset shows the hysteresis loop of the disk edge.

maintaining reasonable soft magnetic properties. A typical hysteresis loop of the disk edge is shown in inset of Fig. 3.12.

The microhardness of the disks is also larger than for the ribbons. Namely, H_V = 6.7 GPa for the ribbons, while H_V = 7.7 GPa at the disks center and values as high as 8.1 GPa are obtained when measuring at 1 mm from the disk edge. The enhancement of H_V can be due to the large amount of microstrain and the small crystallite size usually achieved during a HPT process, which typically result in enhanced mechanical properties [24,95]. However, the high diffusion rate accompanying high pressure torsion is also likely to reduce the free volume of the system, thus diminishing the self-diffusion in the amorphous phase and, as a consequence, the microhardness would also increase [102]. In addition, the flaky shape of the particles is known to be very effective in order to get a highly dense packing of the powders, avoiding the presence of oxides at the particles surface, which would probably have a detrimental effect on the mechanical properties [96]. Finally, it is also possible that the composite-like microstructure observed at the disk edges (i.e., nanocrystals embedded in an amorphous matrix) could be favorable to enhance microhardness [94,103].

Summarizing these results one can see that partially glassy disks of approximately 9 mm in diameter and 0.3 mm in thickness can be prepared by cold-compaction using high pressure torsion of ball-milled $Fe_{77}Al_{2.14}Ga_{0.86}P_{8.4}C_5B_4Si_{2.6}$ amorphous ribbons. The torsion straining process presumably induces significant changes in the short-range order (both chemical and topological) of the multicomponent alloy, which result in the formation of dispersed nanocrystallites inside the amorphous matrix and a reduction in the overall crystallization enthalpy. The disks exhibit enhanced Curie temperature and microhardness with respect to the ribbons. This cold-compaction technique proves itself to be appropriate for the fabrication of thin bulk partially amorphous disks and it is particularly appealing for the consolidation of amorphous alloys with reduced supercooled liquid region.

4. THE MICROSTRUCTURAL CHARACTERISTICS OF ULTRAFINE-GRAINED METALS

4.1. Dislocation density and microstructure of UFG nickel by high-resolution X-ray and TEM

Several authors have made TEM investigations on the microstructure of Ni samples processed by SPD including ECAP [104,105], HPT [106] and by electrodeposition [107-109]. In recent reports it was noted that the microstructure after ECAP shows arrays of reasonably equiaxed grains but the grain boundaries are irregularly arranged and poorly defined suggesting a high-energy non-equilibrium configuration with large internal stresses. HPT straining [106] can produce an ultrafine-grained (UFG) microstructure that may not be fully homogeneous across the sample cross-section. It was concluded that in order to obtain samples with the desired homogeneous UFG microstructure they have to be processed at applied pressure values higher than 6 GPa and with more than five whole revolutions. It was reported that electrodeposition can lead to more extensive refinement of Ni with nanocrystalline microstructure of 20-40 nm.

The highly strained microstructure of SPD materials can only be characterized locally by transmission electron microscopy. In this sense high resolution X-ray diffraction has the advantage of providing information on the mean grain size and a function of grain size distribution, internal microstrains and related dislocation densities [110,111]. It is especially useful in the case of UFG metals and alloys produced by SPD where the measurement of the very high dislocation densities (10^{15}-10^{16} m^{-2}) is complicated by TEM. The complete characterization of the microstructure can be achieved by si-

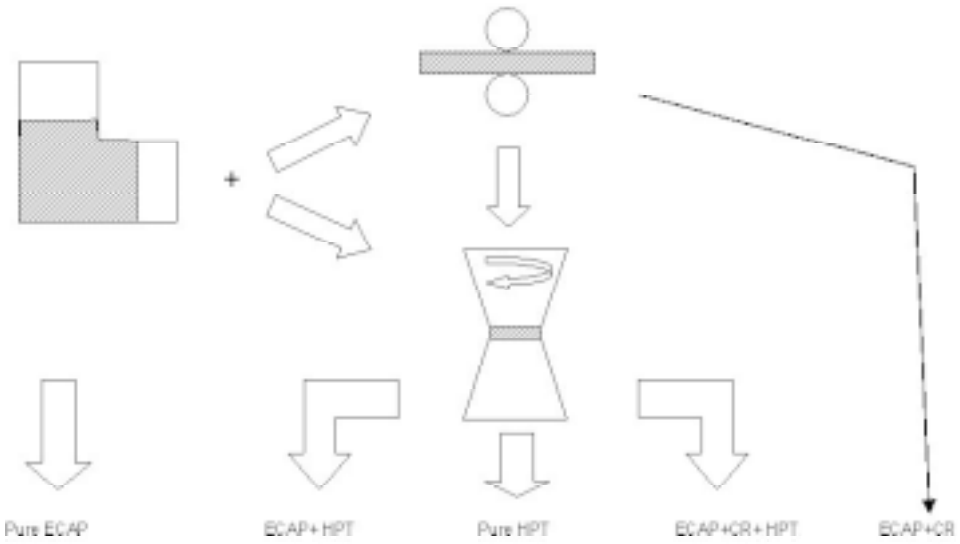

Fig. 4.1. Schematic representation of ultrafine-grained nickel processing.

multaneous application of X-ray diffraction and TEM. This paper reports new results on the measurement of crystallite size and size distribution and the dislocation density in SPD processed pure nickel by means of high-resolution X-ray diffraction. The deformation was carried out by ECAP, HPT, cold rolling (CD) and their combination. An additional specimen was produced by electrodeposition. The results of the X-ray diffraction peak profile analysis are compared with TEM analysis and discussed in terms of correlations and discrepancies.

High purity nickel (99.99%) was deformed by different methods of SPD, i.e. equal channel angular pressing, cold rolling (CR), high-pressure torsion and their combinations. The principles of severe plastic deformation by ECAP and HPT have been documented in several papers [27,104-106]. Nickel cylinders having diameters of 16 mm and lengths of ~100 mm were subjected to ECAP at room temperature using a die with an internal angle of 90°. Samples were pressed repetitively for 8 passes, equivalent to a total strain of ~8, and each sample was reversed from end to end and rotated by 90° about the longitudinal axis between passes. Earlier experiments showed this procedure produces an as-pressed mean grain size of ~0.35 μm [105]. For processing by HPT, disks with diameters of 10 mm and thickness of ~0.3 mm were torsionally strained under a high pressure of 6 GPa for a total of 5 complete revolutions, equivalent to a true logarithmic strain of ~6. This procedure produces a mean grain size of ~0.17 μm [106]. Three additional samples were prepared by combination of different methods: (i) ECAP and cold rolling (denoted as ECAP+CR); (ii) ECAP and HPT (denoted as ECAP+HPT); (iii) the combination of three deformation modes (denoted as ECAP+CR+HPT). Cold rolling of ECAP specimens was performed at room temperature with total reduction in the thickness from 1.7 to 0.25 mm, equivalent to a reduction of ~85%. Fig. 4.1 shows schematically all processing routes. In addition, a sample of electrodeposited nanocrystalline nickel with a grain size of ~35 nm was also included for comparison with the deformed specimens. The microstructure of the samples was examined using high-resolution X-ray diffraction.

The diffraction profiles were measured by a special high resolution double-crystal diffractometer with negligible instrument-induced broadening [112,113]. The Nonius FR591 rotating copper anode (λ=0.15406 nm) was operated at 40 kV and 70 mA. The $K_{\alpha 2}$ peak of the Cu radiation was eliminated by a 0.16 mm slit placed between the source and the symmetrically cut 220 Ge monochromator. The profiles were recorded by a linear position sensitive gas-flow detector (OED 50 Braun, Munich). Selected samples were examined by transmission electron microscopy (TEM) using a JEM-100B electron microscope.

A numerical procedure has been worked out for fitting the Fourier transform of the experimental profiles by the product of the theoretical functions of the size and the distortion (strain) Fourier transforms (Multiple Whole Profile fitting – MWP) [110,111]. The theoretical functions were calculated from a microstructural model with the following assumptions: (i)

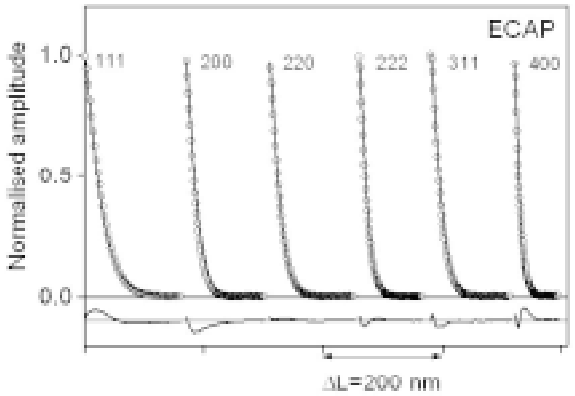

Fig. 4.2. The measured (open circles) and the fitted (solid line) Fourier coefficients as a function of *L* for the ECAP nickel sample. The differences between the measured and fitted values also shown at the bottom of the figure at the same scale.

the crystallites are spheres and have log-normal crystallite size distribution; (ii) the lattice distortions are caused by dislocations. From the median, m, and the variance, s, of the size distribution the area- and the volume-weighted mean crystallite size values can be obtained [110]. Since the area-weighted mean grain size was determined from TEM micrographs, the same weighted mean crystallite size is calculated from the results of X-ray diffraction profile analysis. The area-weighted mean crystallite size was determined from *m* and σ using the following equation:

$$< d >_{AREA} = m \exp(2.5\sigma). \qquad (4.1)$$

The distortion (or strain) Fourier coefficients of a peak profile, A^D, in a dislocated crystal can be given as [114]:

$$A^D = \exp(-\rho B L^2 f(\eta) g^2 \overline{C}), \qquad (4.2)$$

where $B=\pi b^2/2$, *b* is the absolute value of the Burgers vector of the dislocation, ρ is the dislocation density, *L* is the Fourier length defined as $L = na_3$, where $a_3 = \lambda/2(\sin\theta_2 - \sin\theta_1)$, *n* are integers starting from zero, $\eta = L/R_e$, R_e is the effective outer cut-off radius of dislocations, *g* is the absolute value of the diffraction vector, $\overline{C}$ is the average dislocation contrast factor and $f(\eta)$ is a function derived explicitly by Wilkens (see Eqs. A.6 to A.8 in Ref. [114] and Eqs. (22) and (23) in Ref. [110]). Instead of R_e, it is more appropriate to use the parameter $M=R_e \cdot \rho^{1/2}$ defined by Wilkens as the dislocation arrangement parameter [112]. In an untextured cubic polycrystalline specimen the values of $\overline{C}$ can be expressed as a function of the indices of reflections, *hkl* [115]:

$$\overline{C} = \overline{C}_{h00}\left[1 - q\frac{(h^2k^2 + h^2l^2 + k^2l^2)}{(h^2 + k^2 + l^2)^2}\right], \qquad (4.3)$$

where $\overline{C}_{h00}$ is the average dislocation contrast factor for the *h*00 reflections and *q* is a parameter depending on the elastic constants of the crystal and on the character of dislocations (e.g. edge or screw type).

The MWP method has the following steps:

- the Fourier coefficients of the measured physical profiles are calculated by a non-equidistant sampling Fourier transformation;
- the Fourier coefficients of the size and strain profiles were calculated;
- the experimental and the calculated Fourier coefficients are compared by the least squares method.

The procedure has five fitting parameters for cubic crystals: the median, *m* and the variance, σ, of the log-normal size distribution function, the dislocation density, ρ, the dislocation arrangement parameter, *M,* and *q* for the average dislocation contrast factors. The values of *q* have been calculated for nickel assuming the most common dislocation slip system <110>{111}. For pure screw or pure edge dislocations the numerically calculated values of *q* are 2.24 or 1.42, respectively [116]. Consequently, the value of *q* gives the edge or screw character of dislocations. The dimensionless parameter, $M=R_e \cdot \rho^{1/2}$ defined as the dislocation arrangement parameter gives the strength of the dipole character of dislocations: the higher the value of *M*, the weaker the dipole character and the screening of the displacement fields of dislocations. Further details of the fitting procedure are given elsewhere [110,111].

The procedure of X-ray peak profile fitting was carried out for all specimens study here. Fig. 4.2 represents an example of the fitting for nickel produced by ECAP. The figure shows the experimentally determined Fourier transforms (open circles) and the best fitted theoretical curves (solid lines). The differences between the measured and fitted values are also shown in the lower part of the figure. The scaling of the differences is the same as in the main part of the figure. The indices of the reflections are also indicated. As the result of the fitting the microstructural parameters are determined and listed in Table 4.1.

Fig. 4.3 shows the crystallite size distribution for three different processing methods: ECAP, HPT

Table 4.1. Microstructural parameters for the nickel samples processed by different methods.

Nickel samples	m, nm	σ	$\langle d \rangle_{area}$ nm	d_{TEM} nm	$\langle \varepsilon^2 \rangle^{1/2}$, 10^{-3}	q	M	r, 10^{14} m^{-2} X-ray	DSC
ECAP	29±2	0.60±0.05	71±5	350	2.5±0.3	1.84±0.06	3.7±0.4	9±1	0.4
ECAP+CR	25±2	0.41±0.05	38±4	300	2.6±0.3	2.18±0.06	1.5±0.3	11±1	0.6
HPT	26±2	0.44±0.04	42±4	170	3.1±0.3	2.16±0.05	1.5±0.4	17±2	0.7
ECAP+HPT	24±2	0.53±0.05	48±4	140	3.7±0.4	1.64±0.06	1.5±0.2	25±2	1.9
ECAP+CR +HPT	15±1	0.67±0.06	46±3	100	3.5±0.4	1.61±0.05	2.3±0.3	20±2	2.1
Electro-dep.	6±1	0.76±0.06	24±3	35	7.0±0.5	1.66±0.07	4.1±0.4	82±4	6

and electrodeposition. One can see from Fig. 4.3 and Table 4.1 that HPT results in higher dislocation densities and lower mean crystallite size values during deformation than ECAP. At the same time the HPT process leads to narrower distributions of crystallite size compared to ECAP. The method of electrodeposition gives smaller crystallite size and a higher dislocation density than any of the SPD methods. On the other hand, the electrodeposited nickel has the widest crystallite size distribution among all the materials studied here.

The method of high resolution X-ray diffraction allows making some conclusions about the type of dislocations prevailing in the present samples. The ECAP nickel has a mixed type of dislocation since q=1.84 that is equal to the average q values for pure screw (q=2.24) and edge (q=1.42) dislocations. On the contrary the HPT samples show a tendency to have dislocations of more screw character (q=2.16). This can be interpreted in terms of the rotational mode of deformation. The character of dislocations in the electrodeposited material is more edge (q=1.66).

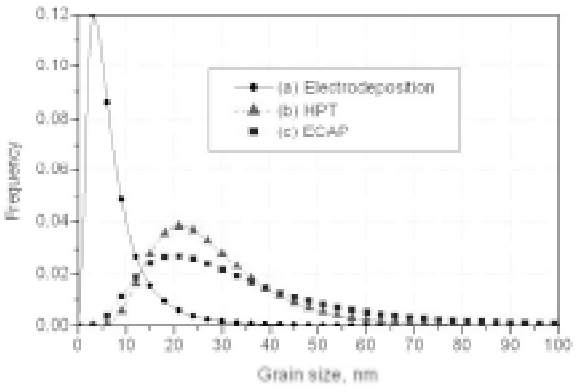

Fig. 4.3. The crystallite size distributions for nickel samples obtained by three different methods: (a) electrodeposition; (b) high-pressure torsion; (c) equal channel angular pressing.

Fig. 4.4 represents the grain size distributions for the nickel samples which were subjected to subsequent deformation process after ECAP to increase the total strain: ECAP, ECAP+CR, ECAP+HPT and ECAP+CR+HPT. It can be seen from Fig. 4.4 and Table 4.1 that any of the second steps of subsequent deformation after ECAP results in a reduction in the crystallite size. Applying three deformation method after each other (ECAP+CR+HPT), further crystallite size refinement is achieved, and the size distribution is broadened compared to the two-step deformed samples. It can be established that the density and the dipole character of the dislocation structure increases by applying additional deformation after ECAP. The increase in the dislocation density is higher for ECAP+HPT than for ECAP+CR. The combination of ECAP+CR+HPT does not result in higher dislocation density compared to ECAP+HPT, and at the same time, the incorporation of cold-rolling between ECAP and HPT gives broader crystallite size distribution with lower mean size (see Table 4.1). It has been found that the smallest crystallite size and the highest dislocation density are obtained by electrodeposition. No definite conclusion can be made on the edge or screw character of dislocation ensembles formed during two- or three-step processing.

The dislocation density of ECAP and HPT samples of nickel is in the same order of magnitude reported by other authors. The values of dislocation density for all nickel samples are about one order of magnitude higher than the dislocation density evaluated for the same material in [117] from differential

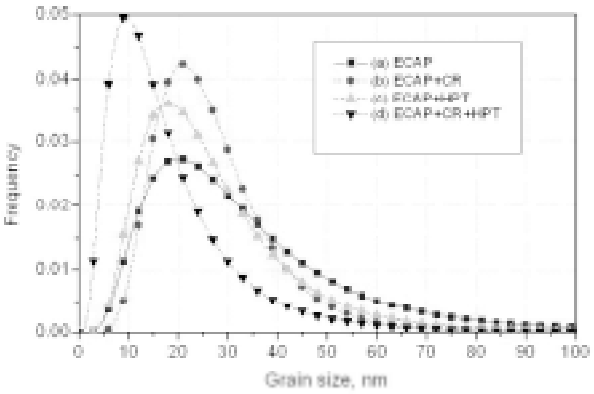

Fig. 4.4. The crystallite size distributions for nickel samples obtained by combination of different methods.

scanning calorimetry (DSC) experiments. The difference can be attributed to the simple model employed in the evaluation of stored elastic energy, which has not taken into account the character of dislocations and their arrangement.

The root mean square strain due to the dislocation structure was determined for the 400 reflection at the value of L=0.5 nm using the following equation [112]

$$< \varepsilon_{g,L}^2 > \approx \left(\frac{\rho \bar{C} b^2}{4\pi} \right) \ln\left(\frac{R_e}{L} \right). \qquad (4.4)$$

In this calculation the values of ρ and R_e obtained from the MWP fitting procedure were used. The root mean square strain values are listed in Table 4.1 and they correlate well with the values of the dislocation density.

Fig. 4.5 shows TEM micrographs for UFG nickel specimens produced by (a) ECAP, (b) ECAP+CR, (c) HPT, (d) ECAP+HPT, (e) ECAP+CR+HPT and (f) electrodeposition. An examination of the TEM pictures in Fig. 4.5 reveals several common features associated with these samples. All of the SPD processes lead to highly non-equilibrium microstructures with many grain boundaries that are poorly defined and with grain interiors having complex contrast. These observations suggest a high level of internal stresses and elastic distortions of the crystal lattice. Former TEM studies showed that the materials processed by SPD techniques may also possess distinctive inhomogeneities [105,106].

Thus, HPT samples generally exhibit some variation in the microstructure between the center and the edge of the disk whereas samples processed by ECAP have an anisotropy of grain-shape along the pressing direction.

In the present investigation, the use of a combination of ECAP and HPT provides an opportunity for removing some of these undesirable properties and for strong refinement of the microstructure. Fig. 4.5d shows a TEM micrograph of nickel after ECAP+HPT processing while Fig. 4.5e demonstrates the microstructure obtained by combination of ECAP, cold rolling and HPT. Under these conditions, the microstructure is rather homogeneous with a mean grain size of ~140 nm for ECAP+HPT and about 100 nm for ECAP+CR+HPT. In agreement with the X-ray analysis, the refinement of the microstructure during the subsequent SPD process after ECAP can be seen by comparing Figs. 4.5a, 4.5d, and 4.5e. It is informative to compare the grain and the crystallite size values obtained by TEM and X-ray diffraction, respectively. For the ECAP processed nickel the mean crystallite size obtained by X-ray (71 nm) is about five times smaller than the value of 350 nm evaluated by TEM. A similar tendency is observed for the nickel sample produced by HPT, but the difference is smaller between the crystallite size obtained by X-ray diffraction (42 nm) and the grain size determined by TEM (170 nm). In the nickel samples produced by a combination of SPD methods, the mean grain sizes are 48 and 46 nm for the ECAP+HPT and ECAP+CR+HPT samples, respectively. The evaluation of TEM micrographs for the same samples gives about 140 and 100 nm, respectively. As has been shown by the X-ray analysis, the three-step-deformation (ECAP+CR+HPT) resulted in broader size distribution of the crystallites with lower median than ECAP+HPT which can also be observed by comparing Figs. 4.5d and 4.5e. For the electrodeposited nickel both X-ray and TEM evaluations give the smallest crystallite (24 nm) or grain size (35 nm) values among the materials studied. It is worth to note that for the electrodeposited nickel sample the area-weighted mean crystallite size value is comparable with a mean grain size obtained from TEM.

The difference between the crystallite size obtained by X-ray and the grain size values determined by microscopy techniques describes the complexity of the microstructure. For the ECAP deformed nickel sample, TEM study gives a value of the mean grain size of about 350 nm [106], orientation imaging microscopy [118] with sensitivity angle θ<2 leads to a value of about 270 nm while the X-ray analysis results in an area-weighted crystallite size of 71 nm.

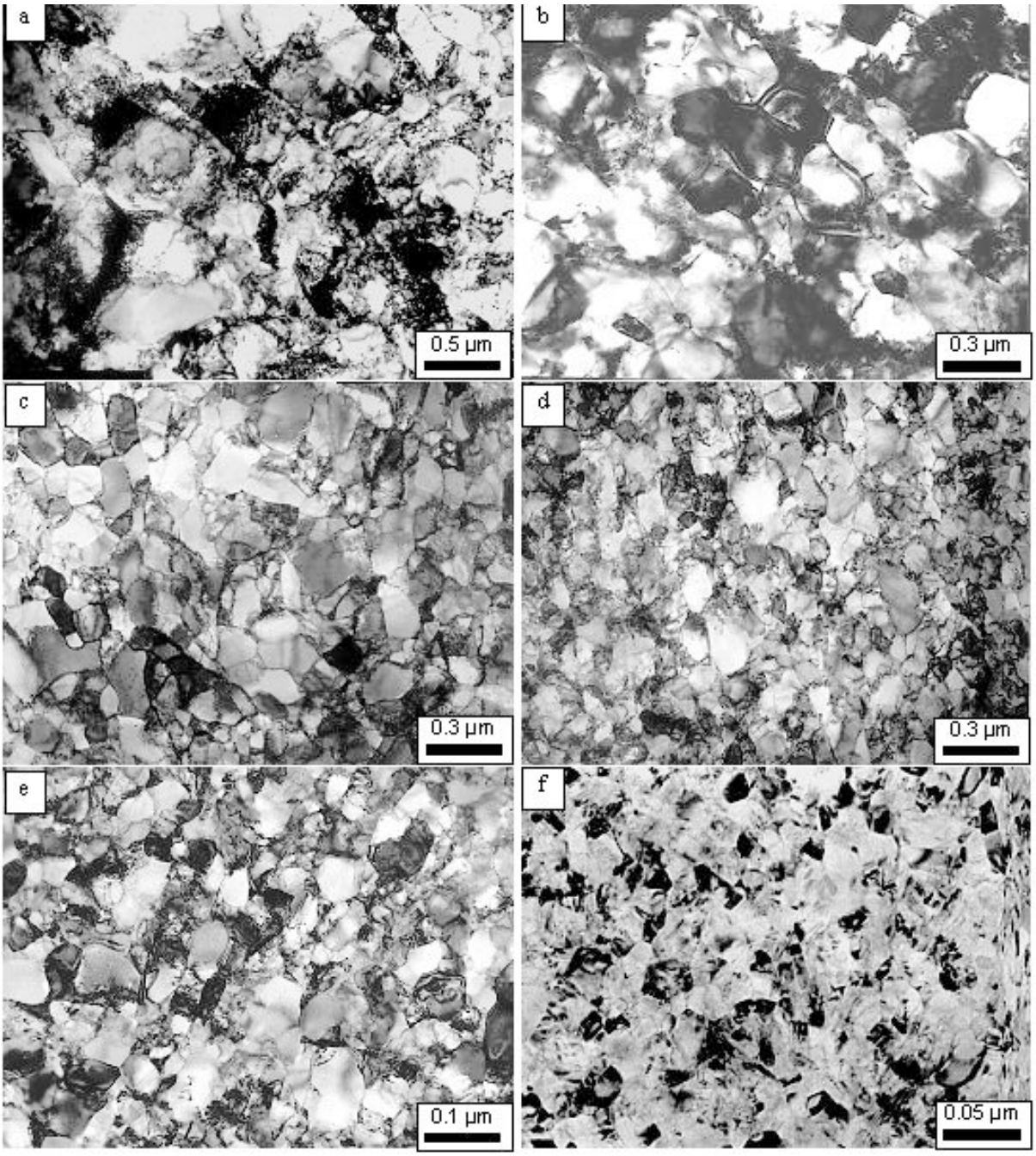

Fig. 4.5. Microstructure of UFG nickel processed by (a) – ECAP; (b) – ECAP+CR; (c) – HPT; (d) – ECAP+HPT; (e) – ECAP+CR+HPT; (f) – electrodeposited nickel.

Each characteristic size value describes a certain feature of the microstructure in ECAP nickel: $\langle d \rangle_{TEM}$ ~ 350 nm corresponds to the average distance between high angle grain boundaries, $\langle d \rangle_{OIM}$ ~ 270 nm gives the typical distance between all grain boundaries with misorientations higher than 2, and $\langle d \rangle_{X\text{-}RAY}$ ~ 71 nm relates to the average size of the coherently scattering domains which usually equals the dislocation cell size in SPD materials.

This conclusion is supported also by comparison of the ECAP and ECAP+CR samples. Although, the grain sizes obtained by TEM (350 and 300 nm) are very close to each other, notable difference can be found in the crystallite sizes determined by X-ray diffraction (71 and 38 nm). This is a consequence of the formation of dense tangles of dislocations arranged in low angle boundaries during cold rolling.

High-resolution X-ray diffraction and TEM experiments were conducted to determine the microstructure and dislocation density in ultrafine-grained materials after processing by ECAP, HPT, cold rolling and their combinations. Additionally to the nanostructured materials produced by SPD, electrodeposited nickel has been investigated. Assuming that the crystallite size distribution in all samples obeys a log-normal function and that the strains are caused by dislocations, the parameters of the crystallite size distribution and the dislocation structure were calculated by fitting the Fourier transforms of the experimental X-ray diffraction profiles to physically well established theoretical functions. The crystallite size values were compared to the grain sizes determined by TEM. It was found that the additional deformation after ECAP resulted in further grain refinement and an increase of the dislocation density. However, the electrodeposition has given even finer microstructure and higher dislocation density than the materials processed by SPD methods. The crystallite size values are lower than the grain size for all the specimens, since the former measures the dislocation cell size in SPD materials. At the same time for the elctrodeposited nickel the crystallite size is close to the grain size determined by TEM.

4.2. OIM study of ultrafine-grained nickel

For many industrial applications, the critical factor in selecting a material is often the specific strength. Ultrafine-grained materials, with grain sizes in the submicrometer or nanometer range, are expected to have higher strength and toughness than their coarse-grained counterparts. Accordingly, grain refinement is generally achieved by developing appropriate thermo-mechanical processing treatments involving a combination of heat treatments and mechanical working. In practice, these treatments have the disadvantage that they are specific to any selected alloy and new treatments must be developed for each separate alloy. An alternative possibility is to attain a UFG structure through the use of a processing technique involving the application of severe plastic deformation: examples of SPD processing include equal-channel angular pressing [4,25,27], high-pressure torsion [4,19,32], accumulative roll-bonding (ARB) [119-121], friction stir processing (FSP) [122-124] or combinations of these techniques such as ARB followed by FSP [125] or ECAP followed by HPT [20,117,126]. An important advantage of SPD processing is that the same procedure may be used to introduce UFG structures into a wide range of metallic alloys.

There are two important characteristics defining the UFG structure in metals. First, it is necessary to measure the mean grain size, the distribution of grain sizes, the distribution of the grain boundary misorientations and the texture of the as-processed material. Second, it is important also to examine the thermostability of the UFG microstructure since, if the ultrafine grains are reasonably stable at elevated temperatures, there is a potential for achieving superplastic ductility at both unusually low testing temperatures and exceptionally rapid strain rates [8]. Despite the fact that an increase in strength is generally associated with a loss in ductility in testing at ambient and low temperatures, recent experiments demonstrated that SPD processing, when taken to a sufficiently high strain, is capable of producing materials exhibiting extraordinary combinations of both high strength and high ductility [127]. This result was attributed to the unique characteristics of the UFG microstructure produced by SPD processing including the presence of an exceptionally high fraction of non-equilibrium grain boundaries [27].

The two procedures of ECAP and HPT appear to be the most attractive for developing microstructures having reasonably homogeneous distributions of ultrafine and equiaxed grains. In ECAP a bar or rod is pressed through a die constrained within a channel bent into an L-shaped configuration [25,128-130] whereas in HPT a thin disk is subjected to a high pressure and concurrent torsional straining [19,32,106].

Although there have been extensive reports documenting the microstructural evolution taking place during SPD processing in ECAP [17,18] and HPT [106] and the subsequent stability of the UFG microstructures in annealing treatments [105,131,132], relatively little attention has been given either to the development of texture in SPD processing or to the nature of the grain boundary misorientation distributions. However, both of these parameters play a significant role in determining the bulk properties of the materials [133,134]. Some information has become available recently on the grain boundary misorientation distributions after ECAP of pure Al and Al alloys [135-145], ECAP of pure Cu [144,146,147], ECAP and HPT of pure nickel [19,118] and ECAP of pure Zr [148].

Although the results on pure Ni are fairly limited [118], the experimental data suggest that HPT pro-

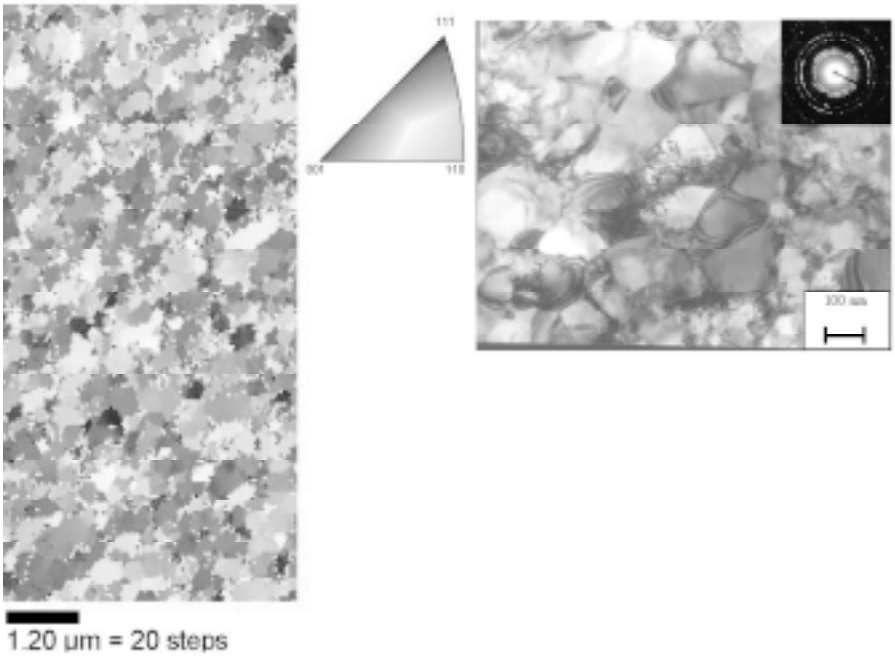

Fig. 4.6. A color-coded orientation image and a corresponding TEM micrograph of the UFG nickel processed through a combination of ECAP and HPT: the standard stereographic triangle shows the orientations of the grains.

duces a microstructure with a higher fraction of high-angle grain boundaries than ECAP. However, no systematic investigation has been conducted to date to examine the development of texture and the concomitant evolution of the grain size distribution and the boundary misorientation statistics when processing by ECAP, by HPT and by a combination of these two processing procedures. Accordingly, the present investigation was initiated to provide this information.

Pure nickel was selected as a model material for use in this investigation and the experiments were conducted to determine the distribution of grain sizes, the texture and the characteristics of the grain boundary misorientation distributions using transmission electron microscopy and orientation imaging microscopy (OIM). In addition, the grain boundary misorientation data were combined with results obtained using high-resolution X-ray diffractometry [20] and differential scanning calorimetry [20] to estimate the grain boundary surface energy in the ultrafine-grained pure Ni. The distributions of the grain sizes, microtexture and the grain boundary misorientations were determined using OIM. The experimental data were collected using a Philips XL-30 FEG scanning electron microscope (SEM) with a TSL orientation imaging system [118,149]. The mean grain size was estimated for each condition using a JEOL transmission electron microscope.

The grain size distributions. The value of the mean grain size represents the key parameter in defining the nature of the UFG microstructure formed through SPD processing. In general, the mean grain size is usually determined from measurements taken using TEM but these measurements tend to be difficult because it is well-established, after processing by both ECAP [150] and HPT [151], that many of the boundaries in the as-processed material are diffuse in nature or represent transition zones between highly deformed grains. In addition, the boundary extinction contours are often very irregular due to the non-equilibrium character of the boundaries and the presence of many extrinsic dislocations. Nevertheless, preliminary observations by TEM gave mean grain sizes in the Ni samples of ~350 nm after ECAP, ~170 nm after HPT and ~140 nm after ECAP+HPT, respectively.

The lack of a homogeneous and clearly-defined array of equiaxed grains in many materials after SPD processing makes it difficult to fully characterize the UFG microstructure in terms of the distribution of grain sizes. One possibility is to assume, a priori, that the distribution follows a log-normal function as in conventional ball-milling but it is not easy to con-

firm this assumption because the complex contrast in the TEM images makes it difficult to clearly differentiate between many of the individual grains.

The problem of microstructural characterization can be significantly overcome through the use of OIM. Fig. 4.6 illustrates this problem by showing images taken by OIM (on the left) and TEM (on the right) for the sample prepared through the combined process of ECAP+HPT: the stereographic triangle in the center shows the orientations of the individual grains recorded by OIM. It is apparent from inspection of both images that the microstructure in this condition consists of a reasonably equiaxed array of grains with a mean grain size in the range of ~0.1 – 0.2 μm.

A complete analysis of the grain size distribution in any UFG structure requires detailed OIM observations and the use of appropriate analytical software. This characterization introduces the ancillary problem of deciding upon the appropriate tolerance angle (TA), where TA is defined as a parameter of the OIM measurements such that two neighboring points are considered to belong to the same grain if the difference in their individual misorientations is less than TA. The effect of using different values for TA is illustrated in Fig. 4.7 where the grain size distributions are shown for samples processed by (a) ECAP, (b)

HPT and (c) ECAP+HPT for values of TA equal to 2°, 5°, 10°, and 15°, respectively. Within each set of distributions in Fig. 4.7, it is apparent that the shapes of the individual plots depend significantly upon the value selected for TA. In general, the grain size distribution after ECAP appears to be multipeaked whereas the distributions after HPT and ECAP+HPT are smoother and reasonably close to log-normal functions.

Fig. 4.8 provides a pictorial illustration of the effect of the tolerance angle by showing, for the same fields of view, the color-coded orientation images after (a) ECAP and (b) HPT for the two tolerance angles of 2° (on the left) and 15° (on the right): these angles represent the lower and upper cut-off limits corresponding, respectively, to a measure of essentially all grain boundaries in the array and a measure of only the high-angle grain boundaries defined according to the Brandon criterion which designates low-angle boundaries as having misorientations up to 15° [152]. Thus, some low-angle boundaries disappear, and the grain size appears intuitively larger, when using the higher cut-off angle of TA = 15°.problem of deciding upon the appropriate tolerance angle (TA), where TA is defined as a parameter of the OIM measurements such that two neighboring points are considered to belong to the same grain if the difference.

It is apparent from Fig. 4.8 that the grain size is significantly smaller after processing by HPT by comparison with ECAP and, in addition, the microstructure appears to be more homogeneous and generally more equiaxed after HPT processing. Furthermore, it appears from Fig. 4.2 that the distributions approximate to a log-normal function for the HPT and ECAP+HPT samples when taking TA = 2° and, despite some perturbations in the curve, the distribution after ECAP may be approximated also to a log-normal function. Thus, it is reasonable to define a tolerance angle of 2° as a suitable cut-off in defining the grain size in UFG microstructures. The grain sizes reported earlier after SPD processing were recorded using TEM and they correspond, to a first approximation, to the use of a tolerance angle of 2°.

Texture analysis and grain boundary statistics. Microtexture data, in the form of pole figures obtained from OIM measurements, are shown in Fig. 4.9 for samples prepared through ECAP, HPT and ECAP+HPT, respectively; also shown in Fig. 4.10 are 3D views of the corresponding orientation distribution functions (ODF) calculated using harmonic methods. The three dimensional ODF for ECAP, HPT and ECAP+HPT nickel samples are plotted in the form of iso-surfaces with 1/4, 1/2, and 3/4 of absolute maximum for corresponding orientation distributions. Fig. 4.9 shows pole figures (001), (011) and (111) types for UFG nickel obtained by ECAP (Fig. 4.9a), HPT (Fig.4.9b) and the combination of both (Fig. 4.9c). Following the work by Canova *et al.* [153], a detailed analysis of texture in pure aluminum after ECAP pressing was accomplished [50]. In particular, it was established that all three components of torsion texture revealed in [49], namely the C-component ({001}‹110›), A- fiber ({111}‹hkl›) and B-fiber ({hkl}‹110›), are observed in ECAP pure aluminum. Similar features have been discovered in ECAP and HPT nickel samples. Major texture maxima correspond to the C- component schematically depicted on Fig. 4.9a. The maximum of the C-component is stronger for ECAP nickel samples (~5.5 of random level) and there is a weak A-fiber present in the pole figures. The orientation distribution function plotted as 3D function in Euler angles (φ_1, Φ, φ_2) is shown in Fig. 4.10. A schematic diagram of the A, B, C- components of pure shear texture is depicted on Fig. 4.10a, where the squares

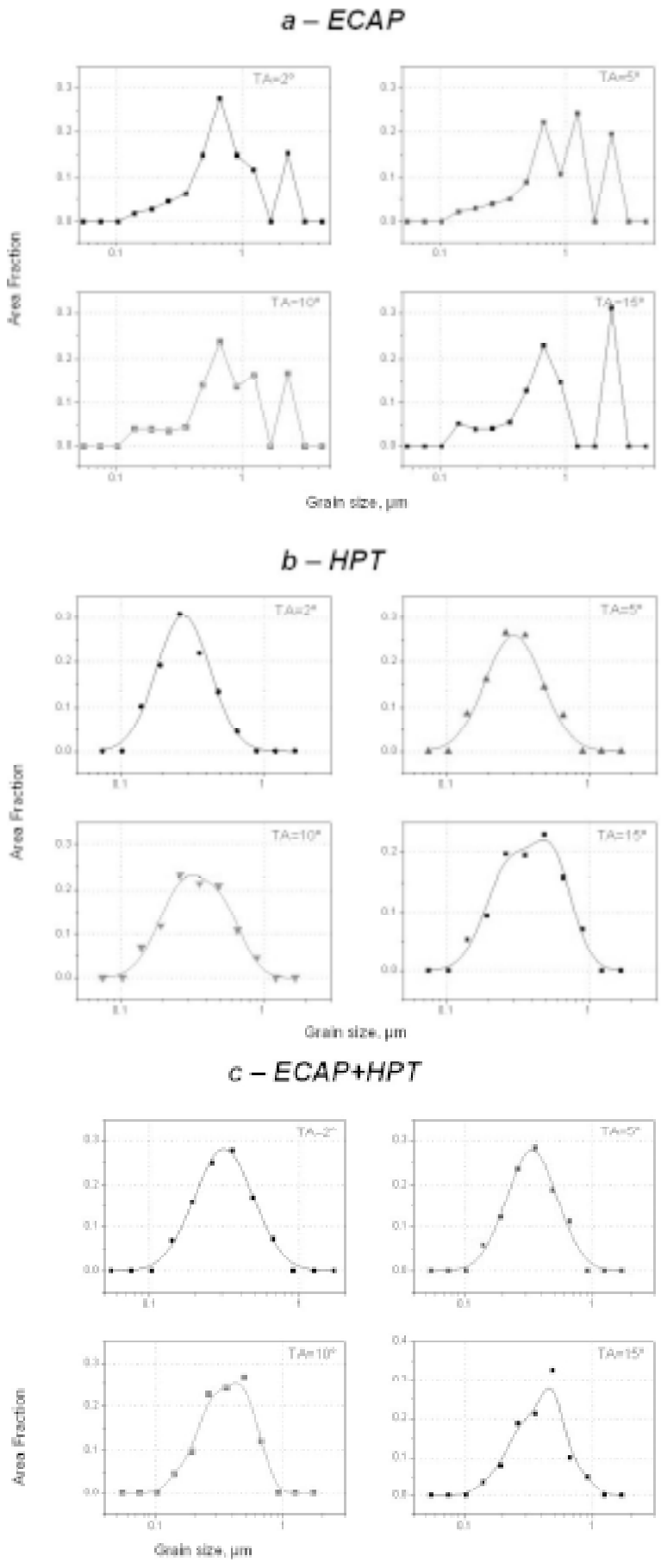

Fig. 4.7. Grain size distributions in UFG nickel as a function of the tolerance angle from 2° to 15° using orientation imaging microscopy after (a) ECAP; (b) HPT and (c) ECAP+HPT.

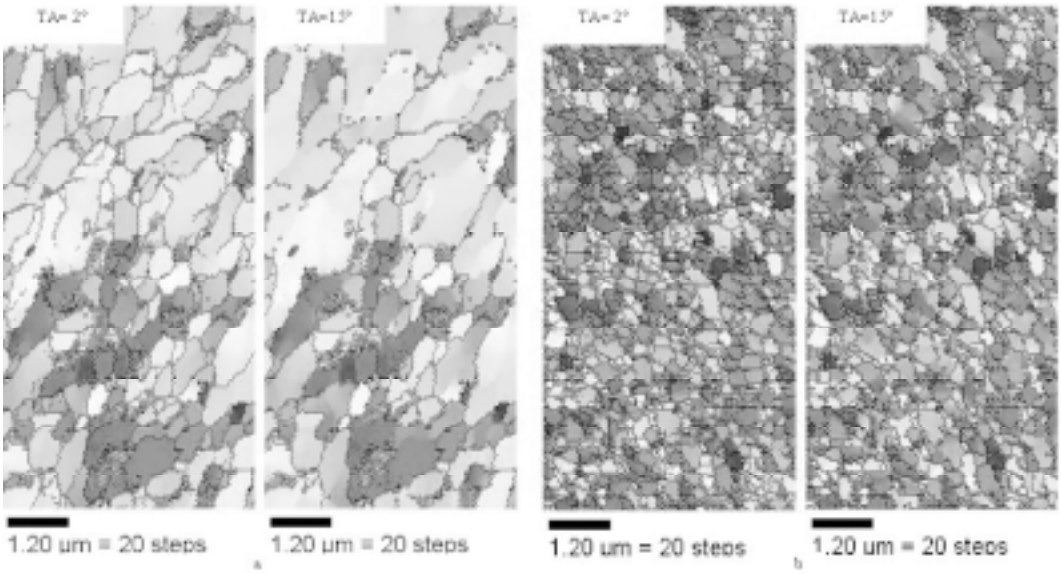

Fig. 4.8. Color-coded orientation images of UFG nickel after (a) ECAP and (b) HPT using tolerance angles of 2° and 15°.

correspond to C-component, circles are B- fiber and blue line represents A-fiber.

It is noted that the ECAP texture (Fig. 4.10b) consists mostly of C-component and it shows a minor maximum near the end of the A-fiber. The texture of the HPT and ECAP+HPT nickel samples possess more complex structures but nevertheless the C-component dominates. Generally, relatively little attention has been given to the nature of the texture after SPD processing. However, there is a report of the evolution of texture in Cu processed by HPT where, with increasing strain in torsion, the intensity of the {200} peak decreased relative to the {111} peak giving an ultimate after 5 turns of HPT of ~6.3 [51]. This result is not consistent with the present data for pure Ni where there is a strong axial texture of the {200} peak with a maximum of ~3 compared to a maximum for the {111} peak below 2.0 of random level. The texture in ECAP copper was measured and modeled very recently [154] and it was shown that it is similar to a shear texture that is characterized by distinct orientations of the C-component [154,155].

The grain boundary misorientation distributions are shown in Fig. 4.11 for the three processing conditions of ECAP, HPT and ECAP+HPT in the form of the distribution of misorientation angle and the relevant axes are shown as insets. The corresponding fractions of low-angle (Σ1) boundaries having misorientations up to 15°, twin (Σ3) boundaries, other special (Σ5-30) boundaries and high-angle boundaries (HAB) having orientations >15° are depicted also as histogram. The misorientation angle in Fig. 4.11 denotes the measured disorientation angle between any two adjacent points in the OIM scan. Inspection of Fig. 4.11 shows the distributions are bimodal in character for all three processing conditions with peaks at both low (<15°) and high (>15°) angles. The peaks at angles <15° are not consistent with the theoretical prediction for a random distribution but the experiments show that the fraction of these low-angle boundaries is lower in HPT than in ECAP and there is an even greater reduction for the sample processed by ECAP+HPT. There is also evidence in all three distributions for the presence of two peaks at the higher angles, with these peaks lying in the vicinity of misorientation angles of ~35° and ~60°, ratio respectively. A similar effect was reported in experiments on pure Al processed by ECAP [139] and the second peak corresponds to the twin misorientation. It follows from Fig. 4.11 that the fraction of low-angle boundaries decreases from ~27% after ECAP to ~17% after HPT and ~14% after ECAP+HPT whereas a random distribution predicts a fraction of high-angle boundaries of ~90%.

The presence of these low-angle peaks is a natural consequence of the very high strains, and thus the large numbers of dislocations, that are intro-

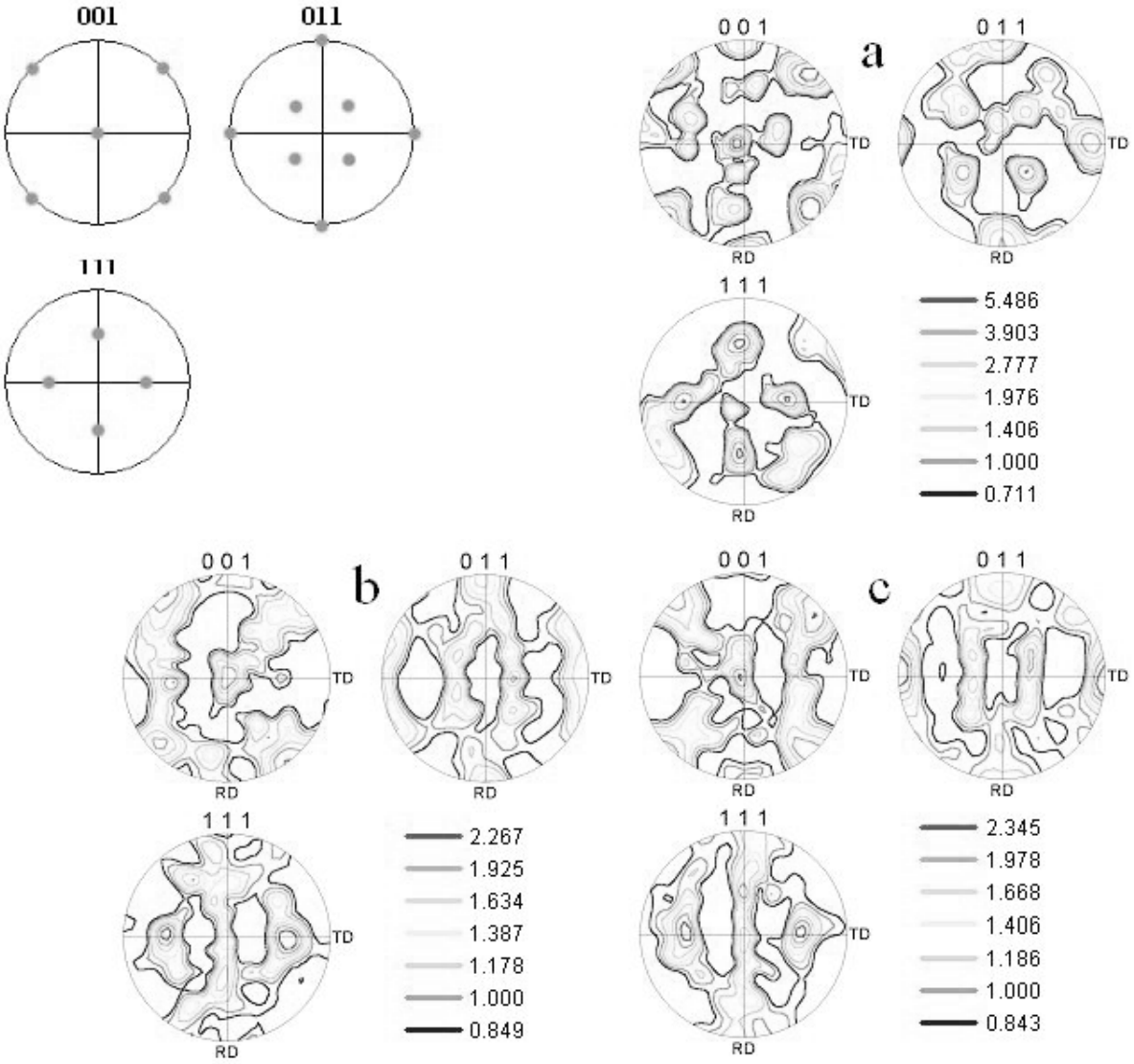

Fig. 4.9. Pole figures (001), (011), (111) for ECAP (a), HPT (b) and ECAP+HPT (c) nickel samples. Schematic view of the same pole figures for C-component of shear texture is shown.

duced into the materials during processing. Nevertheless, these low-angle peaks are not consistent with the theoretical predictions for a random distribution of misorientation angles. An important conclusion from the present investigation is that a combination of ECAP and HPT leads both to a finer homogeneous microstructure and to a higher fraction of high-angle boundaries with a general misorientation distribution that is significantly closer, as shown in Fig. 4.11, to the theoretical distribution. According to the sigma value distribution (Table 4.2), ECAP processing leads also to a higher fraction of twin boundaries ($\Sigma 3$) by comparison with HPT. The fraction of twins after ECAP+HPT was also slightly higher than after HPT, thereby suggesting that the twin boundaries are reasonably stable when subjected to subsequent processing by HPT. Table 4.2 shows also that all processing routes lead to a remarkably high fraction of special boundaries (Σ 5-30) by comparison with the theoretical random distribution

Summarizing this section one can conclude that the results show the mean grain size is largest after ECAP, intermediate after HPT and the smallest grain size of ~140 nm was achieved after a combination of ECAP and HPT. Texture measurements reveal a strong texture after ECAP and a weaker texture after HPT. There are common features for texture development in nickel samples during severe plastic deformation by ECAP and HPT (and

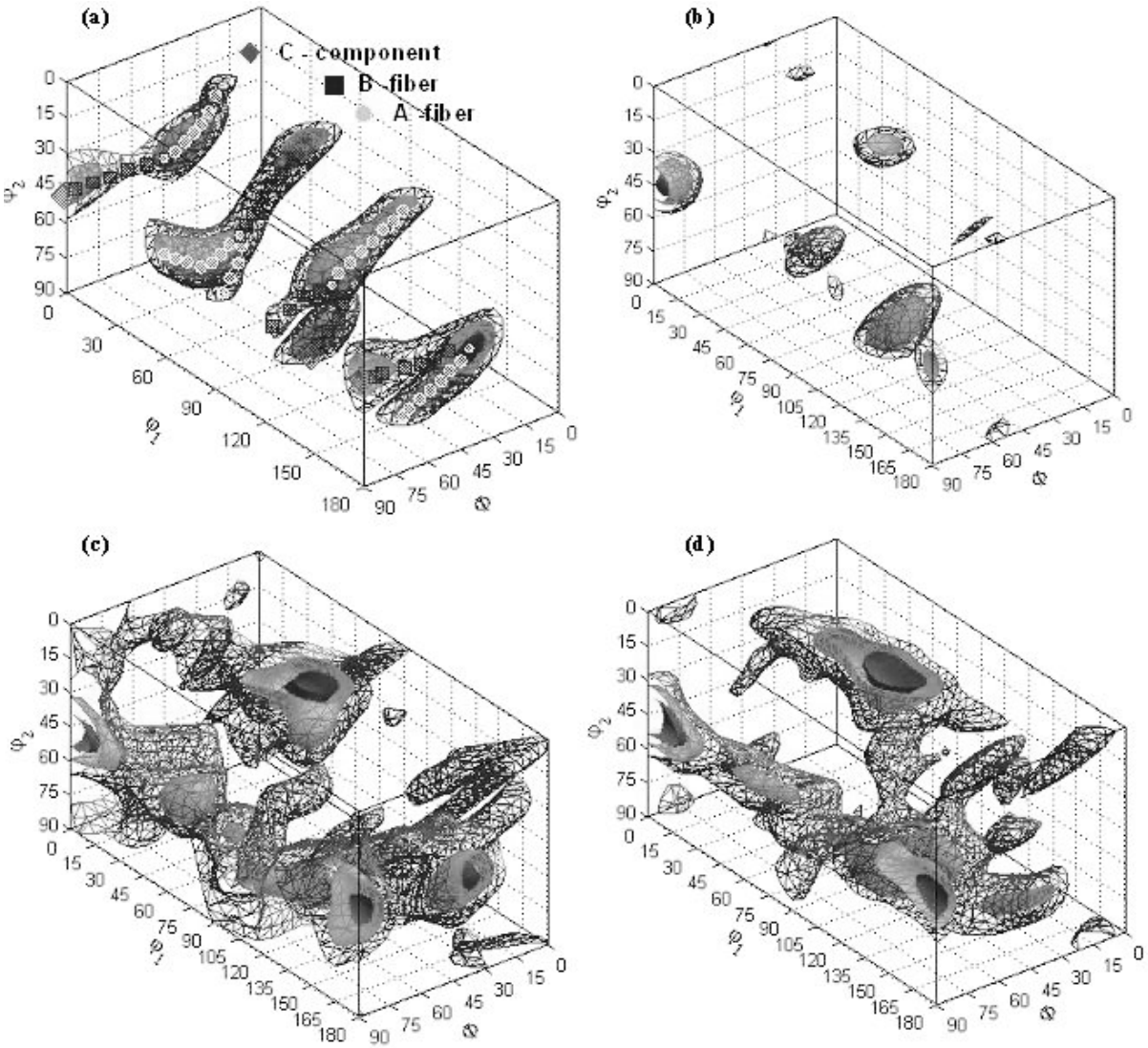

Fig.4.10. 3D view of orientation distribution function for pure shear texture (a), ECAP (b), HPT (c) and ECAP+HPT (d) nickel samples. Iso-surfaces of 1/4, 1/2 and 3/4 of maximum intensity are plotted.

Table 4.2. The grain boundary character distribution (Σ) as a percentage in UFG nickel after ECAP, HPT and ECAP+HPT.

Samples \ Boundaries	Σ 1	Σ 3	Other, Σ5-30	HAB
ECAP nickel	23.2	5.1	11.7	60.0
HPT nickel	15.4	3.0	13.5	68.1
ECAP+HPT nickel	10.5	3.3	15.5	70.7
Random distribution	2.1	1.6	7.0	89.3

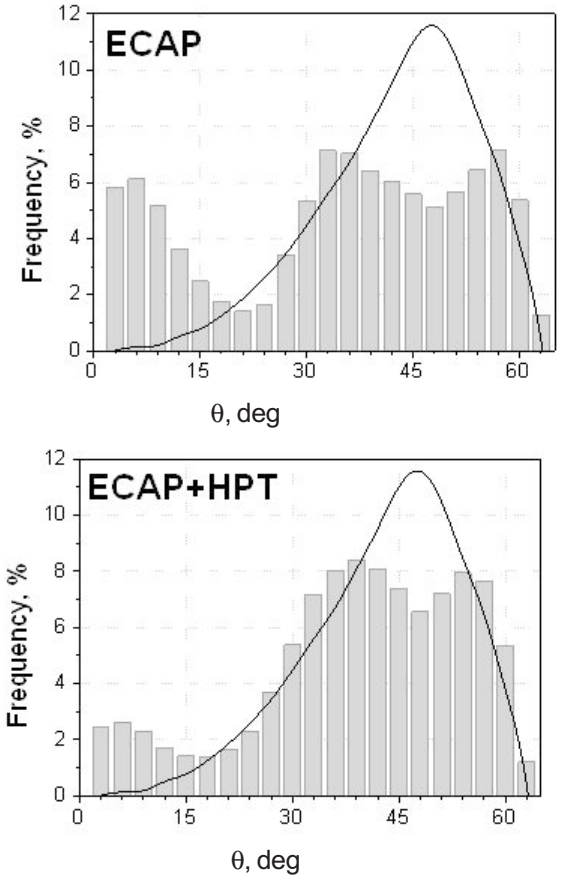

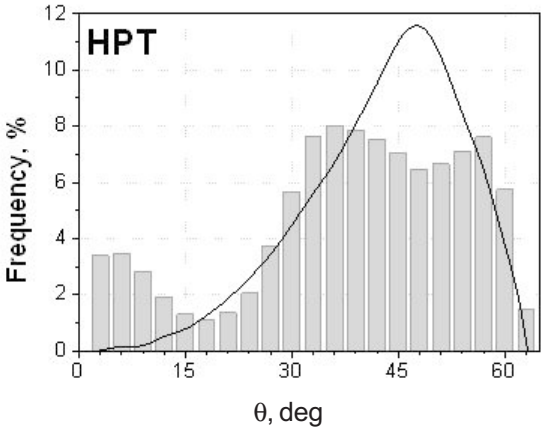

Fig. 4.11. The grain boundary misorientation distributions in UFG nickel after (a) ECAP, (b) HPT, and (c) ECAP+HPT. The solid curve represents the prediction for a random distribution of grain orientations.

also by their combination) and the texture reveals the main components (C-component, A- and B-fibers) typical for pure shear in materials subjected to torsion straining. A combination of ECAP and HPT leads to a similar texture as after pure HPT but with some deviations. An analysis of grain boundary misorientation distributions reveals a higher fraction of low angle boundaries for ECAP nickel (about 27%) with the fraction decreasing for HPT (about 15-17%) and ECAP+HPT samples (below 15%).

4.3. DCS analysis of GB surface energy

In polycrystalline materials subjected to deformation, the total excess of enthalpy per molar material can be expressed as

$$\Delta H = \Delta H_{GB} + W, \tag{4.5}$$

where ΔH_{GB} is the total excess energy from the grain boundaries and W is the total excess energy related to the enhanced elastic energy stored in the dislocations. The first term of equation (4.5) is given by

$$\Delta H_{GB} = \alpha \cdot \gamma \cdot \Omega \cdot N_A \left(\frac{1}{d_0} - \frac{1}{d} \right), \tag{4.6}$$

where α is a geometrical factor, γ is the grain boundary surface energy, Ω is the atomic volume ($1.09 \cdot 10^{-29}$ m^3), N_A is Avogadro's number, and d_0 and d are the initial and final grain sizes, respectively. For an idealized model of spherical grains, the value of a is 3. Since $l/d_0 >> l/d$, it follows that the grain boundary energy may be represented (in units of J mol^{-1}) as

$$\Delta H_{GB} = 3 \frac{\gamma}{d_0} \Omega \cdot N_A. \tag{4.7}$$

The elastic energy stored in the strain field of the dislocation structure may be calculated using the following relationship:

$$W = A^* G^2 b \rho \log \frac{R_c}{r_0}, \tag{4.8}$$

where the coefficient A^* is equal to $1/4\pi$ for screw dislocations and $1/[4\pi(1-\nu)]$ for edge dislocation where ν is Poisson's ratio, G is the shear modulus ($7.89 \cdot 10^{10}$ Pa), ρ is the dislocation density, R_C is the effective outer radius for dislocation interactions and $r_0 \approx \boldsymbol{b}$ is the dislocation core radius where $\boldsymbol{b}$ is the magnitude of the Burgers vector ($2.49 \cdot 10^{-10}$ m). The values of R_C and ρ may be determined from X-ray experiments and the value for A^* can be taken as the weighted sum for the screw and edge dislocations:

$$A^{*} = \frac{1}{4\pi}\left(f_{screw} + f_{edge}\frac{1}{1-\nu}\right), \qquad (4.9)$$

where f_{screw} and f_{edge} are the individual fractions of the screw and edge dislocations. Combining equations (4.5) - (4.9), it follows that

$$\gamma = \frac{d_0 \cdot (\Delta H - W)}{3 \cdot \Omega \cdot N_A}. \qquad (4.10)$$

Usually, the value of γ represents all types of grain boundaries in the material. However, earlier experiments showed that the grain boundary misorientation distribution in UFG nickel subjected to SPD processing is bimodal [118] and the energy of the low-angle boundaries depends strongly on the misorientation angle. Strictly, it is necessary also to consider not the fraction of any particular type of boundary but rather their relative area (or length in a two-dimensional model). Considering a model of identical grains, the frequencies of specific grain boundary misorientations can then be used in the calculation.

The energy of the low-angle boundaries (LAB) as a function of the misorientation angle is given, in the Read-Shockley model [156], by the relationship

$$\gamma_{LAB} = E_0 \cdot \theta \cdot (A_0 - \log\theta), \qquad (4.11)$$

where $E_0=(Gb)/[4\pi(1-\nu)]$ and $A_0=1+\log[b/(2\pi r_0)]$.

The relationship given in Eq. (4.11) can be rewritten in a general normalized form as

$$\gamma_{LAB} = \gamma_{HAB} \cdot \frac{\theta}{\theta_0} \cdot \left(1 - \log\left(\frac{\theta}{\theta_0}\right)\right), \qquad (4.12)$$

where θ_0 is a critical misorientation angle delineating the transition between low-angle and high-angle boundaries and γ_{HAB} is the surface energy for the high-angle boundaries where the misorientations are larger than θ_0. It is generally accepted that the limit for LAB is given by θ_0 = 15° (or π/12 in radians).

In Fig. 4.12, the function represented by Eq. (4.12) is shown as a solid line. The surface energy is then expressed as

$$\gamma = \gamma_{HAB}\left(\sum_{\theta \le 15} f_{\theta}^{LAB} \cdot \frac{\theta}{\theta_0}\left(1 - \log\left(\frac{\theta}{\theta_0}\right)\right) + f^{HAB}\right), \qquad (4.13)$$

where f_{θ}^{LAB} and f^{HAB} are the fractions of the low-angle and the high-angle boundaries, respectively, with the fraction of twins excluded from f^{HAB}. From Eqs. (4.12) and (4.13), the surface energy of the high-angle grain boundaries can be evaluated.

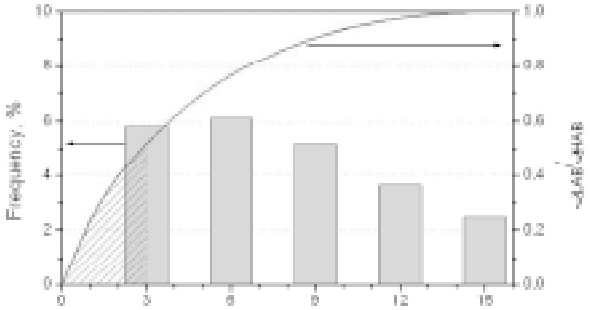

Fig. 4.12. The normalized function (solid line) calculated from Eq. (4.12) and an enlarged portion of the grain boundary misorientation distribution for UFG nickel after ECAP: the hatched area for the grain boundary surface energy corresponds to the fraction of low-angle boundaries in the range from 0 - 3 degrees.

Finally, Eq. (4.12) can be rewritten in the form

$$\gamma = \sum_i f_i \cdot \gamma_i + f^{HAB} \cdot \gamma_{HAB}, \qquad (4.14)$$

where f_i and γ_i are the fraction of low-angle boundaries and the boundary energy for this fraction, respectively.

It is possible, in principle at least, to evaluate the grain boundary surface energy using equation (4.11) in the limit where $\theta \rightarrow 15°$. However, the dislocation core radius is not defined explicitly so that, assuming a reasonable core radius of $r_0 = b/2$ where b is the Burgers vector, it follows that the function in equation (4.11) achieves a maximum at θ = 18.2° and γ_{LAB} (at θ = 18.2°) ~ 0.715 J·m^{-2}. Alternatively, Eq. (4.11) can be parameterized to have a maximum at θ = 15° and in this case the core radius becomes r_0 ~0.61b and the value of the surface energy is ~0.6 J·m^{-2}. Similar values have been reported in the literature for the surface grain boundary energies of coarse-grained Ni [157] and Cu [158] and a very similar estimate was reported also for HPT Cu, based on DSC measurement of the released enthalpy, where the energy was calculated as close to ~0.8 J·m^{-2} [159]. It is interesting to note that the level of the released heat during the DSC experiments on HPT copper was reported as 95.25 J·mol^{-1} for experimental conditions corresponding to a pressure of 5 GPa at room temperature after a total of 5 turns [159]. This value is in excellent agreement with the present result of ~102.7 J·mol^{-1} ob-

tained for HPT Ni under a pressure of 6 GPa at room temperature after 5 turns.

The values of the grain boundary surface energy obtained in the present work are higher than those generally reported in the literature. This suggests that the grain boundaries in the UFG Ni are in a high-energy state as anticipated from several early reports of the presence of non-equilibrium boundaries after SPD processing [4]. Furthermore, the geometrical factor, α, in Eq. (4.6) has been variously estimated for real microstructures as ~1.67 [160] or ~1.3 [161] and these values will lead to even higher estimates for γ_{HAB}.

Despite these shortcomings, the results generally present a comprehensive assessment of the nature of the microstructures introduced into pure nickel through processing by ECAP, by HPT and by a combination of both procedures. In general, there is very good agreement with the results reported for Cu after HPT [159] and there is also a consistency with earlier reports of the non-equilibrium nature of the grain boundaries after SPD processing. The experimental results provide a very clear demonstration of the advantage of processing materials through a combination of ECAP followed by HPT.

5. DECOMPOSITION OF SUPERSATURATED SOLID SOLUTION AND FORMATION OF NS STRUCTURE DURING HPT

In the continuous trend towards the development of materials with improved mechanical properties, a recently developed technique is to produce a very small grain size such that a significant fraction of the atoms are located at the grain boundaries. Among the methods capable of producing such materials, a certain number (e.g. inert gas condensation, ball-milling) result in the production of powders which must be subsequently consolidated. By contrast, methods based on severe plastic deformation produce materials which are monolithic and fully dense without further processing. Conventional processes of high deformation such as rolling or wire drawing strongly change the geometry of the sample. However, two special methods of severe plastic deformation do not involve important changes in the material geometry, namely equal channel angular pressing and high pressure torsion [27,162]. The possibility of producing the bulk nanostructured metals with a grain size in nanometer or submicrometer ranges using these methods have been demonstrated [4]. ECAP consists in forcing a cylindrical specimen to pass through two channels of equal cross-section intersecting at an angle 2θ. After passing through the channels, the sample, while retaining its original geometry, has undergone a shear deformation which, under typical conditions ($\theta = 45°$, i.e. perpendicular channels), is of the order of 1 [163]. The process can be repeated several times in order to accumulate larger amounts of strain. In HPT, a disc-shaped sample is pressed between two Bridgman-type anvils and the upper anvil is rotated, resulting in intense shearing of the material. ECAP is better suited for direct applications of severely deformed materials, since it produces specimens in the centimetre size range. However, for fundamental investigations, HPT gives the possibility of applying extremely high levels of deformation, and thus of determining the upper limits of the material modifications which can be expected from severe plastic deformation.

The SPD of metals and alloys permits one to obtain materials with ultrafine grains or a phase composition that is impossible to produce by conventional thermal treatment. One can mention for example the formation of supersaturated solid solutions [164,165], complete dissolution of cementite during HPT in pearlitic steel [166,167] and disordering or even amorphization in SPD intermetallics [168,169]. One important and still not clarified issue is the role of the diffusion-controlled processes during SPD. In the conventional thermal treatment, a clear difference exists between cold work and deformation at elevated temperature. At high temperatures the diffusion fluxes are high and ensure the recovery processes which proceed simultaneously with deformation at a comparable rate. During conventional cold work the diffusion can be neglected and the resulting microstructure and properties of a material are fully controlled by the deformation. However, it is well known, that the vacancies produced during the irradiation can induce the diffusion fluxes and allow to reach the thermodynamically equilibrium phase structure at low temperatures (e.g. by decomposition of solid solution or formation of low-temperature phases) [170]. Heavy plastic deformation produces many lattice defects, and one can suppose that the vacancy and/or interstitial production during HPT or ECAP is high enough to release the diffusion-controlled recovery processes simultaneously to the deformation. One can suppose that under some conditions SPD can simultaneously lead to the refinement of the grain structure (path from equilibrium) and to release the kinetically suppressed processes of formation of

phases which are equilibrium at temperature and pressure of SPD treatment (path towards equilibrium).

In order to clarify this issue we chose two binary Al-based systems Al–Mg and Al–Zn and ternary Al–Mg–Zn alloys. First of all, these systems are the base for numerous industrial alloys. The diffusivity of Zn and Mg in Al matrix is rather different [171-173], the addition of Zn decreases and that of Mg increases the lattice spacing of Al [174-177]. In Al–Zn alloys the matrix is strengthened by metallic Zn precipitates [178]. In Al-Zn and Al-Mg-Zn systems the precipitates are intermetallic [178,179]. The data on influence of pressure and irradiation exist for these systems [180-183]. One important equlibration path may be the formation of layers of phases which are stable in the grain boundaries (GB) and unstable in the bulk [184-186]. Such phases form as a result of GB wetting, premelting and prewetting phase transitions [21,184-188]. GB phases can substantially influence the GB energy [189], GB segregation [184,189,190], diffusional [187,188,191-194], mechanical [184,190] and electrical [195] properties of polycrystals. The GB wetting phase transitions were recently observed in Al-Mg and Al-Zn systems [13,196]. It means that the GB solidus line in the one-phase solid solution area of the bulk Al-Mg and Al-Zn phase diagrams should exist. The hypothesis was proposed that the high strain rate superplasticity observed in ternary Al-Mg-Zn alloys [197,198] proceed between the GB and bulk solidus line and is driven by the formation of specific GB phases in these alloys [24,196].

Seven binary and ternary Al-based alloys (Al-10 wt.% Zn, Al-20 wt.% Zn, Al-30 wt.% Zn, Al-5 wt.% Mg, Al-10 wt.% Mg, Al-2 wt.% Mg-5 wt.% Zn and Al-4 wt.% Mg-10 wt.% Zn) were prepared by vacuum induction melting and casting into 9 mm diameter rods. They were made of high purity components (5N5 Al, 5N Zn of and 4N5 Mg). Samples of 1 and 0.3 mm thickness were cut off from the rods by spark erosion. The disks with a coarse-grained (CG) structure, 9 mm in diameter and 0.3 mm thick, were prepared from the alloy buttons by grinding, spark erosion sawing and chemical etching in 47% HCl + 50% HNO_3 + 3% H_2O solution. They were subjected to shear deformation by torsion at room temperature under a quasi-hydrostatic pressure of 5 GPa in a Bridgman-anvil type unit (5 torsions, duration of process 300 s, final thickness 0.11 mm) [32]. The sample was placed between an upper immobile and lower rotatable Bridgman anvils. The shear was realized by turning one anvil relative the other at a speed ω = 1 rpm. In previous experiments [199] it was shown that for a given experimental procedure there is no slip between the anvils and the surface of the samples. Due to the high thermoconductivity of anvils and good thermal contact the temperature of the sample during HPT remains below 50 °C. The deformation procedure used in the present experiments (torsion under high pressure) is a complex process since it involves simultaneous torsion and compression of the samples. Details on HPT can found in Section 1.

Transmission electron microscopy investigations have been carried out on the JEM-4000EX microscope at accelerating voltage 400 kV. The microscope is equipped by the Gresham energy dispersive X-ray (EDX) microanalysis system with high-purity Ge detector. It was used for the local analysis of the alloying element concentration. Samples for the investigations were prepared by jet electropolishing technique in an 75% methanol-25% nitric acid siolution at the temperature 243K. Phase constitution of the alloys was analysed by selected area electron diffraction. Dislocation density in TEM investigations was measured using a conventional technique by counting the number of dislocation intersections with a line of a definite length, X-ray diffraction data were obtained on the SIEMENS-500 diffractometer with a graphite monochromator and line position sensitive gas flow detector. Cu$K\alpha_1$ radiation was used. To obtain the lattice parameter of the studied alloys, reflections in high-angle interval (2θ >100°) were used. The precise centroid position of the profile was determined by an approximation procedure with a Lorentz function. The lattice parameter was determined by a Nelson-Riley extrapolation technique; relative error was about 0.01%.

The XRD profile evaluation procedure developed by Ungar *et al.* [110,111] allowed obtaining the values of mean grain size and dislocation density in the Al-Mg and Al-Mg-Zn alloys after HPT deformation. This technique is based on the fitting of the experimentally determined peak profile Fourier coefficients by the Fourier transforms of *ab-initio* size and strain profiles. In this method the strain is assumed to be caused by dislocations and the crystallites are modeled by ellipsoids with log-normal size distribution.

Al-Zn coarse grained (CG) alloys (state before HPT deformation) contain isolated grains of (Zn) solid solution among the grains of (Al) solid solution (Fig. 5.1a). Both (Al) and (Zn) grains are almost dislocation-free with a dislocation density of about 10^{10} m^{-2}. The mean grain size in all studied Al-Zn

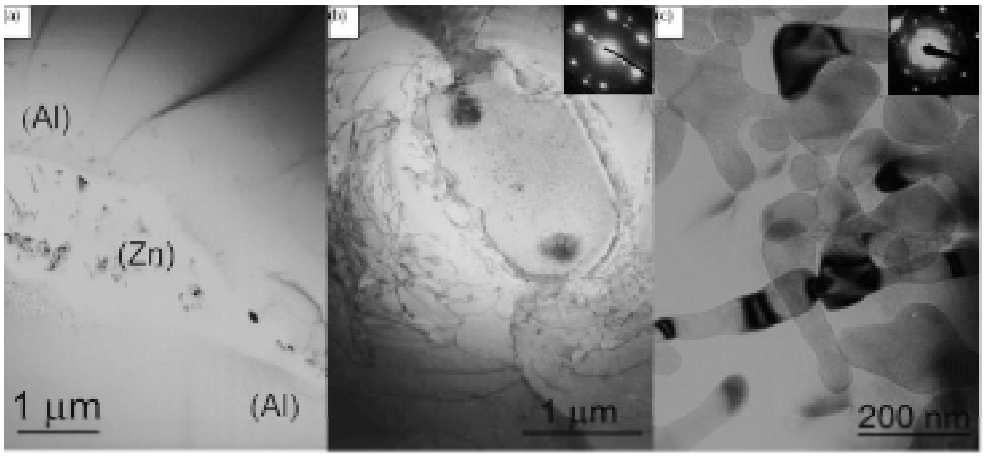

Fig. 5.1. Microstructure of coarse grained aluminum based alloys: Al-30%Zn (a), Al-10%Mg (b); Al-10%Zn-4%Mg (c).

alloys is ~500 μm for (Al) and 3-5 μm for (Zn). Al-Mg and Al-Zn-Mg CG alloys also contain grains of two phases (Figs. 5.1b and 5.1c). These are (Al) solid solutions with a mean size of 500 μm and colonies of intermetallic phases: β-phase (Al_3Mg_2) in Al-Mg alloys (Fig. 5.1b) and τ-phase ($Mg_{32}(ZnAl)_{39}$) in Al-Zn-Mg alloys (Fig. 5.1c). The colony size was about 500 nm. The dislocation density in (Al) is ~10^{12} m^{-2}. XRD data do not reveal the presence of τ and β phases in the alloys. Specimens of all studied Al-Zn alloys after HPT have two phases, and two kinds of grains are observed in the structure (Fig. 5.2). These are (Al) grains with the size of ~800 nm and grains of (Zn) which size is ~200 nm. The dislocation density for these alloys is rather low and ~10^{12} m^{-2}. It is only slightly higher than in the CG alloys. The grains are practically equiaxial with distinct extinction contours.

The structures of Al-Mg (Fig. 5.3) and Al-Zn-Mg (Fig. 5.4) alloys after HPT are rather similar. Grains with sizes of ~150 nm are detected in the structure of both alloying systems. Dislocations are observed to be mainly arranged in subgrain boundaries. Selected area diffraction (SAED) patterns revealed the presence of the β-phase particles in Al-Mg alloy and τ-phase particles. They are uniformly distributed in the material. The particles of the β phase are extremely dispersed. They are not distinguished in the conventional TEM micrographs and they were detected by the additional spots in the electron diffraction patterns. The grain sizes of the β and τ phases can be estimated to be ~10 nm. X-ray analysis did not detect the secondary phases in these alloys. Fig. 5.5 displays the data on the grain size of (Al) solid solution and second phases, (Zn) and Al_3Mg_2, before and after HPT deformation.

For three investigated systems the dependence of the lattice parameter on the alloying element concentration was obtained for both CG and HPT-deformed specimens (Fig. 5.6). It can be seen from

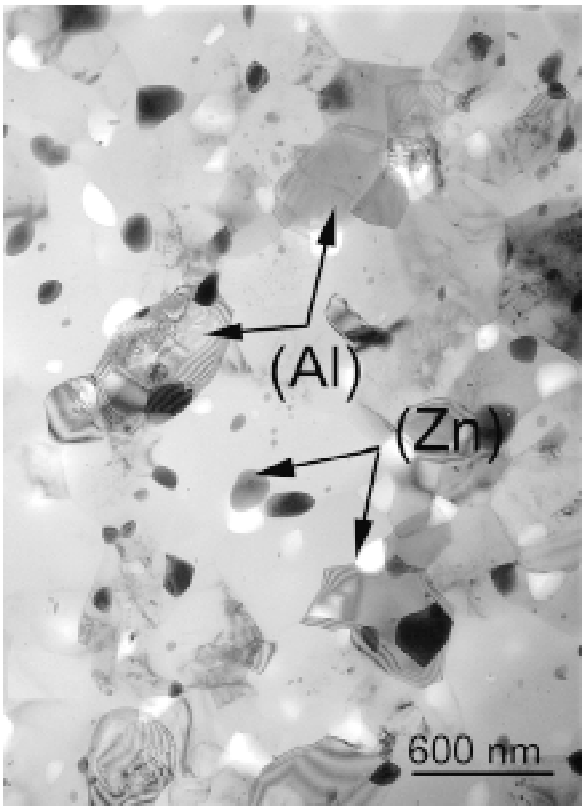

Fig. 5.2. TEM bright field (BF) image of the Al-30%Zn alloy after HPT deformation.

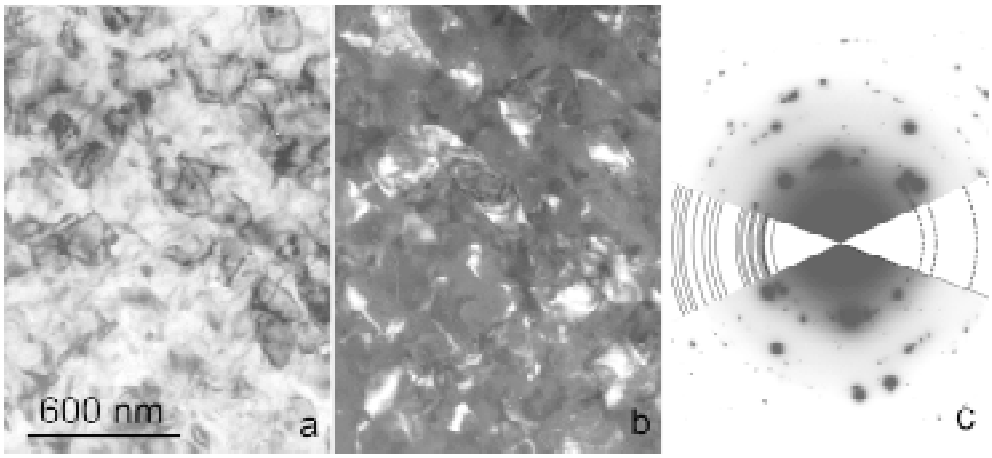

Fig. 5.3. Bright field (a), dark field (b) images and SAED TEM pattern (c) of the Al–10%Mg alloy after HPT deformation.

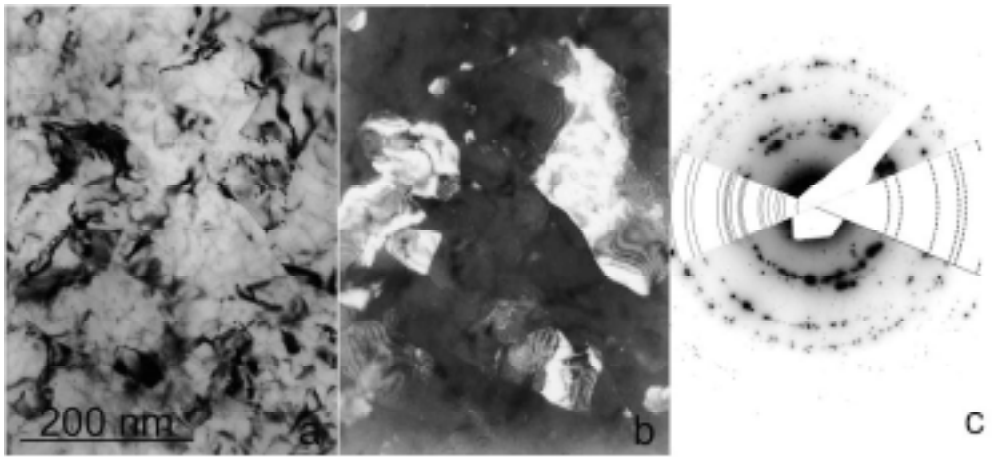

Fig. 5.4. BF (a), DF (b) images and SAED TEM pattern (c) of the Al-4%Mg-10%Zn alloy after HPT deformation.

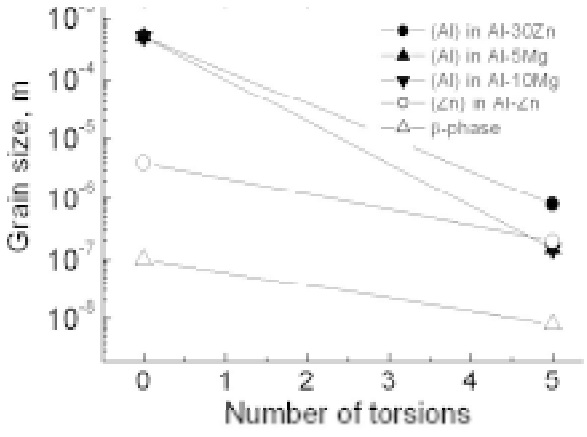

Fig. 5.5. Grain size of (Al) solid solution and second phases (Zn) and Al_3Mg_2 before and after HPT.

Fig. 5.6a for Al-Zn alloys that the lattice parameter *a* increases after HPT deformation, therefore, recovering to a value close to that of pure Al. This means that the phase state of the material after HPT deformation is closer to the equilibrium than that for the CG material. Fig. 5.6c demonstrates that the lattice parameter *a* in the Al-30 wt.% Zn alloy increases very rapidly during HPT. The value of *a* already reaches its final value after one turn (Fig. 5.6c). In Al-Mg alloys the lattice parameter decreases after HPT deformation. However, in Al-Mg alloys such recovery is much less pronounced.

According to the equilibrium phase diagrams, the Al-Zn alloys have to contain the (Al) solid solution with Zn content less than 0.5% and (Zn) solid solution with Al content less than 0.1% at atmospheric pressure and room temperature [178]. In the Al-Mg alloys (Al) solid solution with Mg content less than 1% and β-phase particles have to be

present [178]. The same is true for the Al-Zn-Mg alloys but they contain τ-phase instead of β phase. Only the volume ratio of these phases is different at different Zn and Mg content. In CG samples the same phases are present, but the (Al) solid solution is in all cases supersaturated at room temperature. HPT deformation at room temperature leads to the decrease of (Al), (Zn), τ and β phases grain size. This means that HPT produces a less equilibrium grain structure. On the other hand, the supersaturated (Al) solid solution decomposes in all studied samples. This means that HPT gives a more equilibrium phase structure. From this point of view, HPT cannot be considered as a cold work, since the phase equilibration proceeds even at room temperature, similar to the warm deformation at moderate strains.

Grain refinement and equlibration of phases during high pressure torsion. There is a distinct difference between the behavior of Zn and Mg during the decomposition of supersaturated solid solution under the same HPT conditions. The Al-Zn solid solutions decompose almost completely and reach the equilibrium concentration at room temperature. The decomposition of Al-Mg and Al-Zn-Mg solid solutions proceeds only partly. According to the equilibrium phase diagrams the Al-10 wt.% Zn, Al-20 wt.% Zn and Al-30 wt.% Zn alloys have to contain at atmospheric pressure and room temperature the (Al) solid solution with Zn content less than 0.5 wt.% and (Zn) solid solution with Al content less than 0.1 wt.% [18]. In the Al-5 wt.% Mg and Al-10 wt.% Mg alloys the (Al) solid solution with Mg content less than 1 wt.% and β-phase Al_3Mg_2 has to be present [178]. In ternary alloys Al-2 wt.% Mg-5 wt.% Zn and Al-4 wt.% Mg-10 wt.% Zn the (Al) solid solution with Zn and Mg content less than 0.5 wt. % and τ-phase $Mg_{32}(ZnAl)_{49}$ has to be present [19]. Only the proportions of these phases have to be different in different alloys. It is important to underline that the proportion of Zn and Al in the τ phase can vary. In CG samples the same phases are present, but the (Al) solid solution is in all cases supersaturated at room temperature. HPT deformation at room temperature decrease in all cases the grain size of (Al), (Zn) and intermetallic phases (Fig. 5.5). It means that HPT leads from more to the less equlibrium grain structure. On the other hand, the supersaturated (Al) solid solution decomposes in all cases. It means that HPT leads from less to the more equilibrium phase structure. This is a distinct difference between the behavior of Zn and Mg during the decomposition of supersaturated solid solution in the same HPT conditions. The Al-Zn solid solutions almost completely decompose and reach the equilibrium concentration at room temperature. The decomposition of Al-Mg solid solutions proceeds only partly. In ternary alloys Mg leaves the supersaturated solid solution slower than Zn. Let us consider a possible mechanism which can be responsible for the decomposition of supersaturated solid solution and different behavior of Zn and Mg.

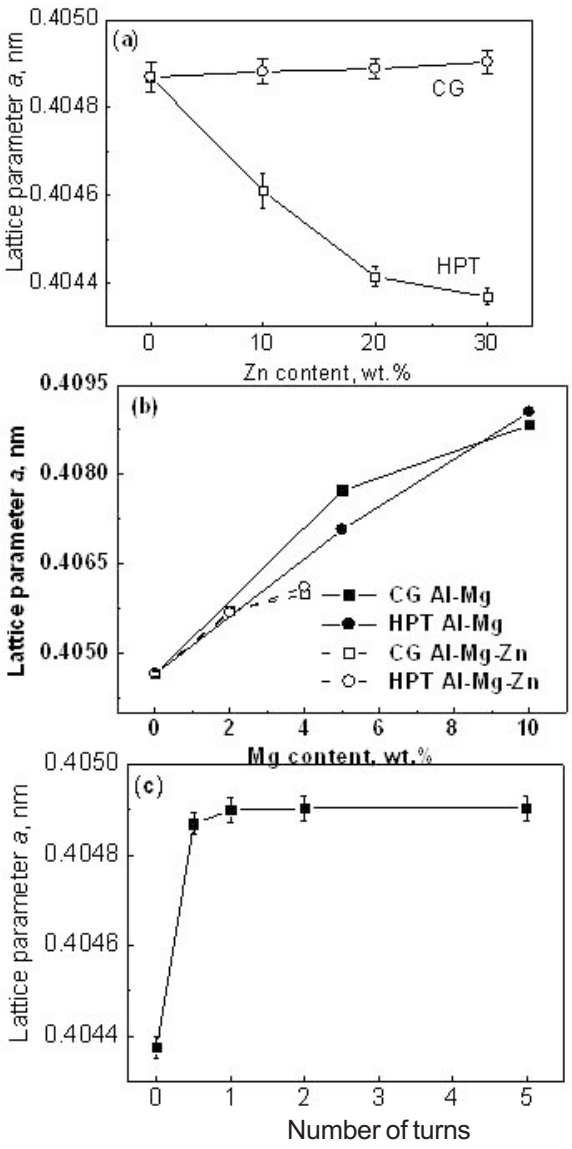

Fig. 5.6. Dependence of the lattice parameter on the alloying element concentration for the Al–Zn (a), Al–Mg and Al–Mg–Zn (b) alloys. (c) Dependence of the lattice parameter vs. the deformation degree in the Al-30wt.% Zn alloy.

Bulk diffusion as a possible mechanism of recovery during HPT. The supersaturation is the driving force for the bulk diffusion of Mg and Zn from the solid solution to the sinks being the particles of (Zn), β and τ phases, respectively. The diffusion paths for individual Zn and Mg atoms would be about 800 and 100 nm, respectively. It corresponds to the bulk diffusion coefficients· of 10^{-15} $m^2 \cdot s^{-1}$ and 10^{-17} $m^2 \cdot s^{-1}$. There are two groups of tracer diffusion data for bulk diffusion of Zn in Al: measured in polycrystals (D_0 = 0.30 10^{-4} $m^2 \cdot s^{-1}$, Q = 121.4 $kJ \cdot mol^{-1}$, 700-920K, ^{65}Zn, [172]) and single crystals (D_0 = 0.259 10^{-4} $m^2 \cdot s^{-1}$, Q = 120.8 $kJ \cdot mol^{-1}$, 630-926K, ^{65}Zn [171]). After extrapolation to 300K both deliver very close values of D (300K) = 0.95 10^{-23} $m^2 \cdot s^{-1}$ and D (300K) = 1.0· 10^{-23} $m^2 \cdot s^{-1}$. The extrapolation of data for Mg bulk diffusion in Al single crystals (D_0 = 1.24 10^{-4} $m^2 \cdot s^{-1}$, Q = 130.4 $kJ \cdot mol^{-1}$, 667-928K, ^{28}Mg [176]) D (300K) = 1.7 10^{-24} $m^2 \cdot s^{-1}$. Although the Mg diffuses somewhat slower than Zn, the difference of about 8 orders of magnitude remains unexplained. Can HPT produce additional vacancies for acceleration of bulk diffusion, similar to those produced by the irradiation of materials?

Irradiation of supersaturated solid solutions at ambient temperature is usually considered as a balance between radiation-induced disordering and radiation-accelerated diffusion towards the equlibrium state [181]. Similar to our work, the irradiation-induced decomposition at low temperatures was observed for Al-Zn solid solutions [183,200-203]. On the other hand, the 1 MeV e^- irradiation enhanced the decomposition of supersaturated Al-Ge solid solutions and no effect was found for the decomposition of Al-Mg alloys [183]. If cold work produces point defects, their presence must accelerate all the phenomena which are controlled by diffusion. Particularly, the reason for the observed decomposition of supersaturated solid solution during HPT can be the temporary increase of the vacancy concentration which increases the diffusion rate.

The early estimations of the vacancy production during cold work were made based on a comparison with the data on residual resistivity [204]. In metals the residual resistivity attributed to point defects increases with the strain ε, and according to laws which vary somewhat with the type of stress-strain curve. From the residual resistivity per Frenkel pair, deduced from irradiation experiments, it was concluded that atomic concentrations of 10^{-5} to 10^{-4} are reached for strains $\varepsilon \approx 1$ [205,206]. Therefore, even a strain of $\varepsilon \approx 1$ produces a concentration of vacancies comparable to the equilibrium one at the melting point (about 10^{-4} [204]). This estimation for metals agrees with data obtained on ionic solids. The cold work of ionic solid should produce a strong temporary increase of its ionic conductivity. Indeed, the strain of $\varepsilon = 0.1$ temporarily multiplies by 100 the electric conductivity of NaCl [207]. From this change one deduces that about 10^{-5} defects per atom have been introduced [62]. Two processes can be invoked in the creation of vacancies and interstitials [204]: (1) Rapid displacement of the nearly pure screw dislocations containing jogs and (2) Recombination of dislocations other than screws placed in neighbouring parallel planes.

The first process is important only by very high dislocation velocities close to that of sound. It is rather improbable even for HPT conditions. Various forms of the second process were proposed [204]. The most probable mechanism for the cubic crystals is that the production occurs each time a mobile dislocation loop cuts across the 'attractive tree' of the Frank dislocation network [208,209]. When two parts of a mobile loop meet after having crossed an 'attractive tree', they are in different slip planes if jogs have been formed, i.e. if the Burgers vectors of the 'tree' are not parallel to the slip plane of the loop. Furthermore, the loops meet at an angle and with a large kinetic energy, because they are running away from their metastable equilibrium position. Therefore, they would recombine by climb over a certain length g, until they meet at a vanishing angle. The climb has pushed the jog of the loop at the length g, thus creating a row of point defects. The number n of point defects created per 'attractive tree' crossed is given by length g. They should be of the order of the initial length of a mobile loop which is in turn proportional to the size of the Frank network l. If dN attractive trees are crossed, the number of point defects created per atom will be

$$dc = nb^3 dN = Alb^3 dN, \tag{5.1}$$

where b is the Burgers vector and numerical constant $A = g/l$ is about 10. The corresponding increase in strain is

$$d\varepsilon = l^2 b dN. \tag{5.2}$$

Since stress $\sigma \approx \mu b/4l$ [204] (m being the shear modulus):

$$dc / d\varepsilon = \sigma / 3\mu. \tag{5.3}$$

Such a law is relatively well followed in face centred cubic metals [208-210]. On the linear deformation stage it predicts a parabolic increase of the atomic concentration c of point defects. From $d\sigma/d\varepsilon \approx$

μ/200 it follows that $c \approx 10^{-4}\,\varepsilon^2$. This estimation agrees well with measurements on copper giving $c \approx 10^{-5}$ to 10^{-4} for strains $\varepsilon \approx 1$ [205,206]. Formal application of this relation for our case $\varepsilon \approx 10$ delivers an exceptionally high vacancy concentration of 10^{-2} which is sufficient to ensure equilibration. However, it is unclear, whether the dislocation mechanism for the vacancy production proposed for low deformations remains valid by SPD. Therefore, we have to consider the alternative mechanism of GB diffusion.

Grain boundary (GB) diffusion as a possible mechanism of recovery during HPT. In Al-Zn alloys the supersaturated solid solution with concentration of ~ 12 wt.% completely decomposes after 300 s. The mean distance between Zn particles in the nanostructured Al-30 wt.% Zn alloy is about 2 μm. This means that each particle collected the Zn atoms from the surroundings with a radius equal to the diffusion path. In case that this process would be controlled by the bulk diffusion, it gives an estimation for $D = (10^{-12}\ m^2/\ 300\ s) = 3\cdot10^{-15}\ m^2\cdot s^{-1}$ which is at least 8 orders of magnitude higher that that of conventional bulk diffusion at 300K. The transport of Zn from the (Al) matrix can be controlled by grain boundary diffusion of Zn atoms along (Al) GBs. Let us suppose that the moving GBs during HPT swept at least once each Zn atom in the bulk, saving the bulk diffusion path from the bulk to a GB. In this case the path for GB diffusion would be roughly the same of 1 μm delivering the sD_0 value of $1.5\ 10^{-24}$ $m^3\cdot s^{-1}$ for GB thickness of $\delta = 0.5$ nm and segregation factor $s = 1$.

In another report [211] the data were obtained for ^{65}Zn tracer GB diffusion in the 99.99% purity Al polycrystal in the temperature interval of 428–593K. Three groups of GBs were defined, namely (I) high-angle GBs with low activation energy Q of GB diffusion ($sD_0\delta = 1\ 10^{-9}\ m^3\cdot s^{-1}$, $Q = 118\ kJ\cdot mol^{-1}$), (II) high-angle GBs with high activation energy ($sD_0\delta = 1.6\ 10^{-11}\ m^3\cdot s^{-1}$, $Q = 90\ kJ\cdot mol^{-1}$) and (III) low-angle GBs between subgrains ($sD_0\delta = 6\cdot10^{-14}\ m^3\cdot s^{-1}$, $Q = 60\ kJ\cdot mol^{-1}$). The extrapolation of these data for the Zn diffusion to 300K deliver, respectively, (I) $sD\delta = 3\cdot10^{-24}\ m^3s^{-1}$, (II) $sD\delta = 2\cdot10^{-26}\ m^3s^{-1}$, and (III) $sD\delta = 2\cdot10^{-29}\ m^3s^{-1}$. The first value is surprisingly close to the estimation for the diffusion path needed for the equilibration of the composition of Al-Zn supersaturated solid solution during the HPT treatment. A similar value of $sD\delta = 10^{-23}\ m^3\cdot s^{-1}$ follows also from [212,213].

In [214] the parameters of Zn GB diffusion were measured by electron probe microanalysis in Al-bicristals with individual tilt and twist GBS with various misorientation angles in the temperature interval 523–613K. The pre-exponentials $sD_0\delta$ and activation energies Q for tilt GBs lie in the intervals $2\ 10^{-16}$–$10^{-12}\ m^3\cdot s^{-1}$ and 40–80 $kJ\cdot mol^{-1}$ respectively [214]. The pre-exponentials and activation energies for twist GBs lie in the intervals 10^{-15}–$10^{-9}\ m^3\cdot s^{-1}$ and 50–130 $kJ\cdot mol^{-1}$ respectively [215]. The extrapolation to 300K delivers sDd values for tilt GBs between 10^{-24} and $10^{-22}\ m^3\cdot s^{-1}$. Therefore, all tilt GB studied in [69] and some twist GBs form the family of 'high-diffusivity' GBs can build the channels for the diffusion which is quick enough to eqilibrate the Al-Zn solid solutions during HPT.

In [216] the parameters of Zn GB diffusion were determined in the Al-30 wt.% Zn alloy using the discontinuous precipitation reaction controlled by GB diffusion. The advantage of these measurements is that they were performed at the rather low temperatures of 350–500K close to the ambient temperature. The extrapolation to 300K delivers the sDd value $4\cdot10^{-23}\ m^3\cdot s^{-1}$. Therefore, the GBs in Al form the diffusion paths for Zn which can be responsible for the decomposition of supersaturated solid solution during HPT. The ^{65}Zn tracer measurements obtained in the temperature interval of 493 – 673K demonstrate that the increase of Zn content can further enhance the GB diffusivity in Al-Zn alloys [217-219]. The extrapolation to 300K delivers the $sD\delta$ values of $3\cdot10^{-22}\ m^3\cdot s^{-1}$ (2 wt.% Zn), $10^{-21}\ m^3\cdot s^{-1}$ (4.33 wt.% Zn) and $10^{-20}\ m^3\cdot s^{-1}$ (8 to 10 at.% Zn).

The data for Mg GB diffusion in Al are not so numerous, perhaps due to the lower values of sDd. In [218,220] the values of $sD_0\delta = 7\cdot10^{-14}\ m^3\cdot s^{-1}$ and $Q = 87\ kJ\cdot mol^{-1}$ were obtained. The extrapolation to 300K delivers the $sD\delta$ value $5\ 10^{-28}\ m^3\cdot s^{-1}$. It is about 5 orders of magnitude lower than the typical values for the Zn GB diffusivities. The direct comparison of Zn and Mg diffusion allow the data on chemical diffusion of Al-0.1 wt.% Sc alloys [221]. Though the $sD\delta$ values were extracted from the comparison of integral measurements on coarse- and nanograined polycrystals obtained by ECAP (as well as in [220-222]), the data demonstrate undoubtedly the lower GB diffusion of Mg in comparison with Zn. This fact can explain the slower decomposition of supersaturated solid solution in Al-Mg alloys studied in our work in comparison with Al-Zn alloys in the same HPT conditions. Nevertheless, both Zn and Mg GB diffusivities extrapolated towards 300K are much higher than the $sD\delta$ value for the Al GB self-diffusion ($10^{-31}\ m^3\cdot s^{-1}$ [213]). Basing on rather scarce data on GB diffusion in Al, one can conclude that Al-Ga supersaturated solid solutions would also de-

compose very quickly (sD_0 value extrapolated to 300K is about 10^{-21} m^3s^{-1} [223]).

If GB diffusion is so effective, why does the supersaturated solid solution not decompose without any HPT? The reason is in the low bulk diffusivity. The solute atoms are frozen in the bulk and cannot reach the GBs. During HPT, GBs move and cross many times every element of the volume, sweeping in such a way the 'frozen' solute atoms. This mechanism is to some extent the opposite of the well-known diffusion-induced grain boundary migration.

Influence of the high pressure and GB phase transitions. The pressure during HPT is 5 GPa. It is sufficient to influence both the phase diagram and diffusivity, and the system could evolve to the state which is in equilibrium at high pressures and differs from that at atmospheric one. Let us analyse this factor. The solubility of Zn in (Al) decreases with increasing pressure and no new phases appear at room temperature [180,181]. The same is true also for the Al-Mg system [182]. High pressure drastically decreases the bulk diffusivity. The extrapolation of data obtained in Al-Mg alloys at 3.3 GPa by studying the chemical diffusion in polycrystals (D_0 = 3 10^{-5} $m^2 \cdot s^{-1}$, Q = 151 $kJ \cdot mol^{-1}$, 667–928K [224]) to 300K and 0% Mg delivers the value D (300K, 3.3 GPa) = 10^{-27} $m^2 \cdot s^{-1}$. It is about 3 orders of magnitude lower than at atmospheric pressure (see above). Extrapolation to 5 GPa gives a value of D (300K, 5 GPa) = 10^{-28}–10^{-29} $m^2 \cdot s^{-1}$. The data of investigations of Zn GB diffusion under high pressures in Al polycrystals [225] were obtained in conditions similar to [212]. They demonstrate that by extrapolation to 5 GPa the GB diffusivity decreases by 3.5 to 4.7 orders of magnitude depending on the GB class. By using the estimation made above, one obtains (I) $sD\delta$=10^{-27} $m^3 \cdot s^{-1}$ and (II) $sD\delta$=10^{-30} $m^3 \cdot s^{-1}$. These values are again lower than the estimated sDd value of 1.5 10^{-24} $m^3 \cdot s^{-1}$ needed for the equilibration of supersaturated solid solution by GB diffusion. It seems that the hypothesis of the additional vacancies produced during SPD is realistic and can explain the appearing discrepancy.

It has been shown that some GB phase transitions (prewetting, premelting) can lead to the formation of thin equilibrium layers of GB phases which are stable in the GB and unstable in the bulk [184-186]. If the grain size in matrix A decreases, the formation of GB layers consumes more and more atoms of second component B. Simple geometrical considerations demonstrate that if such a layer has two monolayers of B like in Cu-Bi system [184,189,190] it consumes about 6, 15 and 20 vol.% B at grain size d = 50, 20 and 10 nm respectively. On the other hand, thin layers of GB phases do not input significantly in XRD spectra, it is complicated to observe them in conventional TEM and even by HREM. In [167] about 2.4 vol.% cementite disappeared from XRD spectra and TEM micrographs by decreasing the grain size d between 50 and 20 nm. It can be explained by the formation of a thin layer of a GB phase [21]. GB layers can also lead to the enhanced GB diffusivity $sD\delta$ increasing to the certain extent s, D and δ as in the Fe-Si-Zn and Cu-Bi systems [21,187,188,191,192,194]. Some indications of GB phase transitions exist for the Al-based systems with high GB diffusivity like Al-Zn or Al-Ga. The data of this work also demonstrate the difference in equlibration kinetics between Al-Zn and Al-Mg systems and make reasonable the search for the GB layers in the Al-based systems.

It may be concluded that (i) Severe plastic deformation by HPT of binary and ternary Al-Zn, Al-Mg and Al-Mg-Zn alloys decreases drastically the size of (Al) and (Zn) grains (below 100 nm) and particles of reinforcing b and t phases (below 10 nm). Therefore, HPT leads to the formation of nanostructure which is less equlibrium than that of the initial coarse grained material; (ii) At the same time, during HPT the Zn-rich supersaturated solid solution (Al) decomposes completely and reaches the equilibrium corresponding to room temperature. This process is less pronounced for Mg-rich (Al). In ternary alloys Zn also leaves the supersaturated solid solution easier than Mg. Therefore, HPT leads to the formation of phase structure which is more equlibrium than that of the initial coarse grained material; (iii) Most probable mechanism of the equilibration of the (Al) supersaturated solid solution is grain boundary diffusion accelerated by fluxes of vacancies built due to the SPD and by the sweeping of Mg and Zn atoms from the bulk by moving GBs; (iii) Therefore, the severe plastic deformation of supersaturated solid solutions can be considered similar to irradiation at ambient temperature, as a balance between deformation-induced disordering and deformation-accelerated diffusion towards the equilibrium state.

6. ANNEALING PHENOMENA AND CREEP BEHAVIOR IN NANOSCALE MATERIALS

6.1. Grain boundary state and creep of bulk nanoscale metals

Many useful properties of metallic polycrystals, in particular strength and plasticity, are affected sig-

nificantly by their structural features, especially grain boundary state [226-228], both the structural state and extent of GBs (grain size) being of importance [229,230]. Submicrocrystalline and nanostructured metallic materials produced by severe plastic deformation are characterized by significant extent of GBs and by non-equilibrium (high energy) GB state relative to the respective coarse-grain counterparts, which may be due to long-range elastic stress fields arising on the GBs [10,231,232]. The above metals are noted for high diffusivities of their GBs, which exceed by several orders the respective values for their coarse-grain counterparts [11,233,234,235]. However, the effect of GB diffusivity on plastic deformation development and structural evolution regularities during annealing, especially at elevated temperatures and simultaneously applied loading (e.g. during creep), has been studied insufficiently. Few theoretical investigations (if any) are concerned with relating the diffusion features and diffusion-controlled processes in submicrocrystalline materials to their GB state. Another step in this direction may be the development of computational methods for defining static and dynamic characteristics of GBs in these materials. In particular, a method of computer-aided GB simulation technique is proposed. This enables one to relate the specific surface energy and stresses arising on the GBs in submicrocrystalline and nanostructured metals to the excess volume of GBs and to define diffusivities over the GBs. The effect of GB state on the creep features in submicrocrystalline metals has been investigated experimentally. The results obtained are presented herein.

Energy, stresses and diffusion on the GBs in submicrocrystalline and nanostructured metals. The grain boundary is a planar defect of the crystalline structure. The equilibrium atomic bond lengths in the GB core are different from those of the ideal crystal lattice. However, only partial relaxation of the GB atomic structure is allowed due to the constraints imposed by the neighboring grains. Therefore, even if all of the atoms are in positions corresponding with the minimal free energy, stresses would arise in the system containing GBs. The excess stresses associated with the GBs are described by the components of the 2D tensor of stresses $\tau_{\alpha\beta}$ on the interface (e.g. GB) [236]:

$$\tau_{\alpha\beta} = \int_{-\infty}^{\infty} \left[\sigma_{\alpha\beta}(z) - \sigma_{\alpha\beta}^{(0)} \right] dz, \qquad (6.1)$$

where the co-ordinate axis z is chosen along the normal to the GB; $\sigma_{\alpha\beta}(z)$ are the volume stress tensor components dependent on the co-ordinate z; $\sigma_{\alpha\beta}^{0}$ are the stresses concentrated in a grain far away from the GB core where the GB effect is negligible. The following equation relates the GB stresses to the specific surface energy of the GB (γ) taken per unit of GB area [236]:

$$\tau_{\alpha\beta} = \gamma\delta_{\alpha\beta} + \frac{\partial\gamma}{\partial\varepsilon_{\alpha\beta}}, \qquad (6.2)$$

where $\delta_{\alpha\beta}$ denotes the Kronecker delta function; the partial derivatives are taken with respect to the strain tensor components $\varepsilon_{\alpha\beta}$ in the GB plane. Eq. (6.2) relates explicitly the GB stress components, i.e. the GB tension characterized by the specific surface energy (γ) of the GB and the second term related to the variation in γ during the deformation. Due to GB formation, the available energy would increase: hence γ would always be positive in sign. No constraints are imposed, however, on the sign of the derivative $\partial\varepsilon_{\alpha\beta}/\partial\varepsilon_{\alpha\beta}$ and of the GB stresses. The quantity $\tau=\Sigma\tau_{\alpha\alpha}/2$ (analog of pressure $P=\Sigma\sigma_{ii}/3$ for the 3D tensor of elastic stresses σ_{ii}) is a scalar characteristic of the GB stresses. In the presence of tensile stresses with the GB area tending to reduce elastically the stress τ would be positive in sign, while in the presence of compressive stresses with the GB area tending to increase elastically the stress t would be negative in sign.

On the other hand, the GB stresses, while being a macroscopic quantity, are induced by the atomic structural features and interatomic forces in the GB core. Therefore, the GB stresses can be related to the atomic structural features of the GB using the excess GB volume δV, i.e. rigid-body displacement of grains along the normal to the GB plane, as a generalized characteristic of the GB on an atomic scale level:

$$\delta V = \frac{(V_{GB} - V_B)}{A}, \qquad (6.3)$$

where A is the GB area; V_B is the perfect crystal volume; V_{GB} is the volume of bicrystal having the same number of atoms.

The theoretical dependencies of δ and $\sum$ on excess volume δV are obtained using the calculated values of the respective quantities as representative sample of high-angle symmetrical tilt GB in model copper bicrystals. We used the well-known model of bicrystal with rigid atom layers in directions normal to the GB, which bound the simulation

cell, and periodic boundary conditions in the GB plane [237]. The calculations were performed by the molecular statics method at 0K and the embedded-atom method (EAM) potential is used to describe the atomic interactions in Cu [238,239]. In the EAM framework the configuration energy E for a system of atoms can be given as the sum of contributions E_i of atoms i by the following relation

$$E = \sum_i E_i = \sum_i \left\{ F_i[\bar{\rho}_i] + \frac{1}{2}\sum_j \Phi_{ij}(R_{ij}) \right\}, \qquad (6.4)$$

where $\bar{\rho}_i = \sum_{j\neq i} \rho_i(R_{ji})$ is the superposition of atomic densities $\rho_j(R_{ji})$ in the site of atom i for the rest of the atoms in the system; $F[\rho]$ is the embedding function and $\Phi(R)$ is the pair potential as a function of interatomic spacing R. Assuming the volume stresses to become negligible far away from the GB, the GB stress tensor is described by the following relation [240,241]

$$\tau_{\alpha\beta} = \frac{1}{A}\sum_i \sum_{j(\neq i)} \left(F_i'[\bar{\rho}_i] \frac{\partial p_j(R_{ji})}{\partial R_{ji}} + \frac{1}{2}\frac{\partial \Phi(R_{ji})}{\partial R_{ji}} \right) \cdot \frac{R_{ji\alpha} R_{ji\beta}}{R_{ji}}. \qquad (6.5)$$

Here $\vec{R}_{ij} = \vec{R}_j - \vec{R}_i$ is the vector directed from site i to site j and the primed term is the first derivative of the embedding function with respect to the argument.

Fig. 6.1 illustrates the sample of high-angle symmetrical tilt GBs considered herein, the GB orientations corresponding with the graphic construction proposed in [242]. As is seen from the figure, the GBs considered are fairly uniformly spread over the entire region of high-angle symmetrical tilt GBs in the fcc crystal. Consideration was given to sample of 33 GBs in Cu having reciprocal densities of coincidence sites in the range $\Sigma = 5$ to $\Sigma = 253$, the GB excess volumes varying in the interval of 0.06 to 0.34 Å.

Specific surface energies γ of GBs and GB stresses τ have been calculated and the results are presented in Fig. 6.2 as the excess volume function. As is seen from the figure, the specific surface energy of GBs is an approximately linear function of the excess volume, which is in good qualitative agreement with the reported data [243]. The proportionality factor is defined from the inclination of the straight line $\gamma(\delta V)$ to an accuracy of 9.9%; the value obtained is equal to 1.28 (J/m^2)/Å. The dependence $\tau(\delta V)$ obtained for the GBs in Cu is also an approxi-

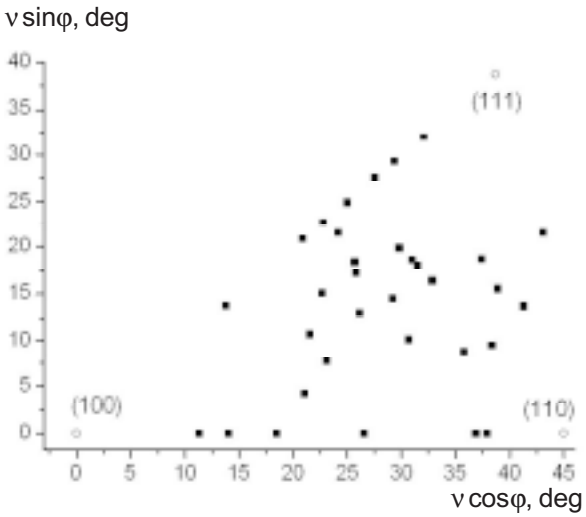

Fig. 6.1. A schematic of symmetrical tilt grain boundaries (dark squares). ν and φ are the polar an azimuthally angles at which the normal is directed to the grain boundary plane.

mately linear one. The respective proportionality factor is determined to an accuracy of 8.5%, the value obtained is equal to 9.85 (J/m^2)/Å (Fig. 6.2b). It can be concluded that the values t obtained for GB having significant excess volume are 1.5 times as high as the values γ. As is seen from Fig. 6.2b, the GBs having insignificant excess volume are characterized by GB stresses that are negative in sign. Thus it is stated that GB stresses differ from GB tension in a qualitative sense since GB tension is determined by specific surface tension; hence it is negative in sign. The dependency $\tau(\delta V)$ illustrated in Fig. 6.2b has a negative final value in the range $\delta V \geq 0$; hence this can be only associated with high-angle GBs.

By the treatment of the above dependence $\tau(\delta V)$ one has to take into account the general features exhibited by the atomic structure of high-angle GBs in metals. A number of theoretical and experimental investigations have provided data on GBs on the atomic scale level (see in review [232]). It is found that the average atomic density within the GB is lower than that of the crystal volume. (GB excess volume is positive in sign). However, within the GB core there occur pairs of atoms separated by a spacing that is much less in comparison with the atomic spacing within the ideal lattice. With due regard to the specific features of GB atomic structure in metals, a plausible explanation can be offered for the fact that the GB stresses would increase from nega-

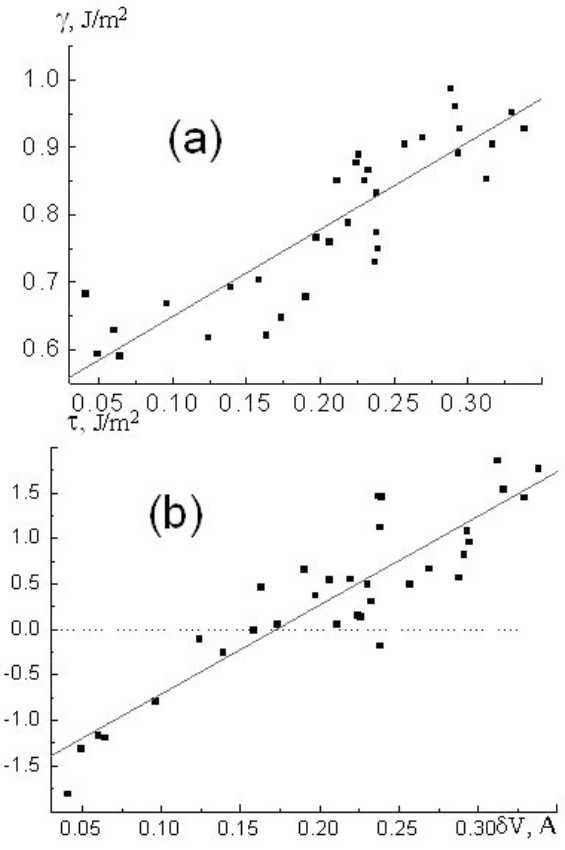

Fig. 6.2. The excess volume δV dependencies of the calculated values of grain boundary energy γ(a) and grain boundary stresses τ(b). The straight lines in the figure are plotted on the base of linear extrapolation by the least squares method.

tive values to values exceeding the specific surface energies of the GBs (Fig. 6.2b). This may be attributed to the following two factors. On the one hand, reduction in the average atomic density with a resultant decrease in the average coordination number of atomic sites in the GB core brings about a reduction in the average equilibrium bond length within the GB relative to that of the grains.

The approximation in the EAM framework takes into account the concurrent reduction in the average equilibrium bond length with decreasing coordination number, which is a specific feature of the atomic interaction in metals to maintain bond order [244]. However, the equilibrium bond length within the GB stops short of reaching the average due to the constraints imposed on the local atomic displacement by the interaction with the atoms within the neighboring grains. Consequently, within the GB there arise tensile (positive) stresses the level of which increases with growing excess volume of the GB (concurrent reduction in the average atomic density within the GB).

On the other hand, the bonds between atoms in close proximity would be contracted. Hence the contribution of these atoms to the GB stresses is a negative one, which determines the sign of stresses on the GB with insignificant excess volume.

Thus, the estimates obtained for the GBs in Cu suggest that both the GB stresses and the specific surface energies of the GBs are growing linearly with increasing GB excess volume. However, the GB stresses arising on the GBs with insignificant excess volume, as distinct from the specific surface energies of the GBs, are negative in sign.

Thus the computational technique developed is intended for (I) calculation of GB stresses and specific surface energies on the GBs in submicrocrystalline and nanostructured materials by assuming the activation energy of GB diffusion to vary in proportion to the GB specific energy per atom of the GB core (atomic density per unit of GB area is assumed to be equal to three atomic monolayers); (II) correlation of GB diffusivities in coarse-grain, submicrocrystalline materials and nanostructured polycrystals produced by SPD, D_b and D_{SPD}, respectively. The relationship $D_{SPD}/D_b=\exp[\Delta E/(kT)]$ has been established for Cu [245], where ΔE is the difference between the specific energies of the GBs in the submicrocrystalline and coarse-grain states as determined from the theoretical dependence of GB energy on GB excess volume. An analysis of this relationship shows that the GB diffusivities in submicrocrystalline metals exceed by a factor of 10 to 10^3 the respective values of the coarse-grain counterparts.

Thus, the diffusivity estimates provided by the computer-aided simulation of GB stresses and the dependencies of specific surface energy of GB on GB excess volume support the results of direct methods which suggest that the effective diffusivities derived for submicrocrystalline materials are by several orders higher relative to the respective coarse-grain counterparts.

The effect of GB state on the creep in bulk submicrocrystalline metals. A comparative study was made of the creep in submicrocrystalline and coarse-grain metals [10, 246, 247]. It has been found that the creep behavior of submicrocrystalline metals exhibits a distinctive feature in the temperature interval $T < 0.3\ T_{melt}$ (T_{melt} is melting point), i.e. the

apparent activation energy of creep, Q_c, decreases by 1.5 - 2 times relative to the respective coarse-grain counterparts, which might be due to the growing contribution of grain boundary sliding (GBS) to the total deformation. It is known [248] that the attainment of superplastic state and grain refinement in superplastic alloys causes a changeover in the deformation mechanisms from processes involving dislocation slip in the grain bulk to GBS mechanisms. The apparent activation energy for the creep, Q_c, in this case decreases from values approximately equal to the activation energy for bulk self-diffusion, Q_v, which controls the processes of climb of lattice dislocations to values close to the activation energy for grain-boundary diffusion, Q_b, which controls the processes of GBS [235]. It has been found [227] that the contribution of GBS to the total deformation during the creep of coarse-grain polycrystalline material can be increased without grain refinement. This is achieved by translating the GBs into a nonequilibrium (high-energy) state by generating grain-boundary diffusion fluxes of impurity atoms from an external source. In this case, Q_c also decreases to become close to values corresponding to grain-boundary diffusion.

Thus the creep behavior of submicrocrystalline metals produced by SPD is found to exhibit distinctive features, which might be attributed to two factors, i.e. GB state and grain size. This led to attempts to define the extent to which each of these two factors affects the mechanisms involved in the creep of submicrocrystalline metals [249].

When annealing treatment is performed at temperatures below the recrystallization temperature [10], this causes relaxation of elastic strains and reduction in the density of defects, especially on the GBs and in the near-GB regions with resultant changes in the state of faulted metal structure. The processes involving recovery of structure, recrystallization and formation of elastic stresses can be controlled using reliable methods, e.g. transmission electron microscopy in conjunction with optical metallography, as well as investigations of temperature dependencies of microhardness and electrical resistivity [249]. Fig. 6.3a illustrates the temperature dependence of electrical resistivity. As is seen from the figure, the processes of recovery start operating in submicrocrystalline Ni even in the temperature interval 373-573K, with recrystallization being completed in submicrocrystalline Ni and Cu at 673K and 573K, respectively.

When the annealing is carried on in the temperature range of 398-548K, no marked changes

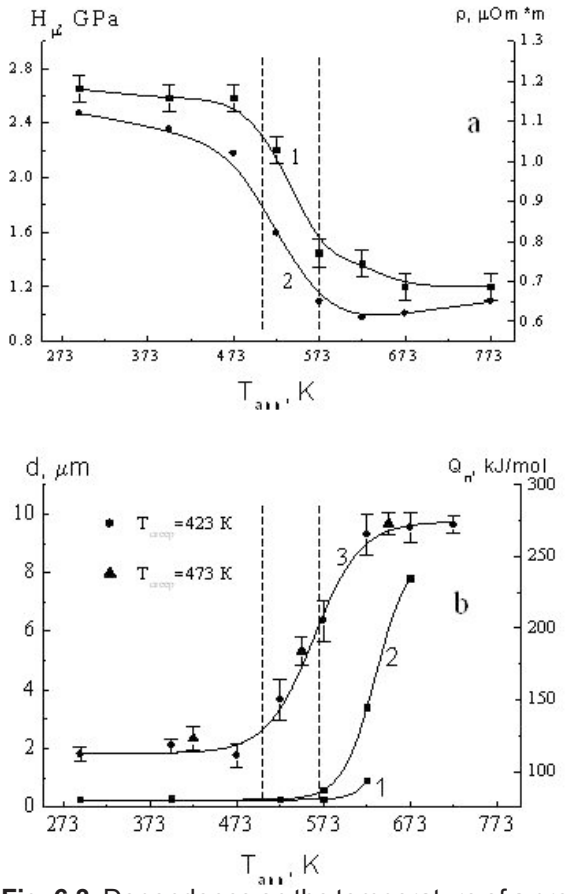

Fig. 6.3. Dependence on the temperature of a preliminary annealing of (a) microhardness (curve 1) and electrical resistivity (curve 2) and (b) grain size *d* (curve 1and curve 2) and effective activation energy for creep Q_c of submicrocrystalline nickel (curve 3).

are found to occur in the worked material structure with the grain size remaining the same as determined by electron microscopy. However, after annealing at 523 and 548K, the number of grain boundaries with fringe contrast increases to 10-20% and the extinction contours inside grains surrounded by such boundaries vanish. This is evidence for the development of stress relaxation processes on such GBs in a material whose grain size remains unchanged. After annealing at 573K, the material grain size in isolated material regions increases up to 0.4-0.8 μm. The samples subjected to annealing at 573-673K undergo recrystallization. Materials with such structure are characterized by a bimodal distribution of grain sizes. After annealing at 673K, the grain size distribution is close to a normal logarithmic one. The dependence of average grain size on

annealing temperature obtained for submicrocrystalline Ni is displayed in Fig. 6.3b (curves 1 and 2).

Fig. 6.3b (curve 3) shows the dependence of effective activation energy for creep, Q_c, on the preliminary annealing temperature which was obtained for submicrocrystalline Ni. As is seen from the figure, the quantity Q_c obtained for submicrocrystalline Ni in the as-received state and after the annealing at $T < 523K$ has a significantly lower value relative to the coarse-grain counterpart (115±15 and 276 kJ/mol, respectively). It should be noted, however, that the exponent n for the stress index in the stress dependence of steady-state creep rate obtained for submicrocrystalline Ni (after annealing at 398K) is slightly higher relative to the respective value obtained for the coarse-grain counterpart ($n \sim 9$ and $n \sim 7$, respectively) [250]. After annealing at $T > 473K$, the value Q_c begins to increase. At an annealing temperature of 673K the recrystallization of structure is completed and the value Q_c becomes equal to 270±10 kJ/mol, which is close to the apparent activation energy for creep in coarse-grained Ni.

Thus, the above experimental results indicate that the variation in the apparent activation energy as a function of preliminary annealing temperature observed during creep in submicrocrystalline Ni exhibits two distinctive features. First, the value Q_c observed for submicrocrystalline Ni decreases by a factor of 2.5 relative to the coarse-grain counterpart. Second, the value Q_c tends to grow significantly after annealing in the temperature range of 473-573K, while the average grain size remains practically the same.

It is known that during the creep of coarse-grain Ni under the conditions specified herein the main processes involved in the deformation are those of intragranular dislocation slip controlled by volume self-diffusion with the apparent activation energy for creep being close to that for volume self-diffusion, Q_v [250]. The values Q_c obtained for submicrocrystalline (SMC) Ni were matched against the available data on the activation energy Q_v of volume self-diffusion observed in coarse-grained Ni (284 kJ/mol) and the activation energy for grain-boundary diffusion, Q_b, in submicrocrystalline Ni (60.2 kJ/mol [11,233]. It has been found that the value of the apparent activation energy of creep for SMC nickel is much lower than Q_v but twice as great as Q_b. This suggests that during the creep in submicro-crystalline Ni under the experimental conditions specified herein two mechanisms of deformation are operative: intragranular dislocation slip controlled by volume diffusion and GBS controlled by grain-boundary diffusion. The contributions of intragranular dislocation slip and GBS are approximately the same. It might be for this reason that the value Q_c obtained for submicrocrystalline Ni is lower than the activation energy for volume diffusion and significantly greater than the activation energy for grain-boundary diffusion observed for the same material.

It is found [251] that the contribution of GBS to the total deformation is likely to be significant in submicrocrystalline metals at relatively low temperatures. Thus in the tensile Cu samples it amounted to 20% at room temperature. The GBS processes are operative during the creep of nanocrystalline Ni samples investigated herein, including those subjected to preliminary annealing at 398K, which is evidenced by the presence on the polished sample surface of distinct steps associated with shear along the grain boundaries at $T \leq 423K$ [249]. It is reasonable to assume that at higher temperatures the process of GBS also contributes essentially to the total deformation during creep. The significant contribution of GBS to the total deformation by the active tension and during the creep of submicrocrystalline materials appears to be related to two factors: the nonequilibrium (high-energy) state of grain boundaries that are formed as a result of SPD and the small grain size (a few tens of microns) [10]. The increase in the creep activation energy observed for submicrocrystalline Ni [248] subjected to a preliminary annealing at 473-573K, with the grain-size remaining unchanged, can be related to the transition of the GBs from nonequilibrium to equilibrium state and to the resulting decrease in the contribution of GBS to the total deformation during creep. Upon increasing the annealing temperature, Q_c continues to grow to become equal to the activation energy of bulk self-diffusion due to recrystallization and grain growth. As a result, the contribution of GBS to the total deformation becomes less significant and in the temperature interval investigated the processes of intragranular deformation become predominant involving dislocation motion controlled by volume self-diffusion [251].

The computer simulation studies of the grain boundaries in Cu and Ni suggest that both the stresses and the specific surface energy of the grain boundary grow linearly with increasing excess volume of the grain boundary. However, the stresses on the grain boundaries having insignificant excess volume are negative in sign as distinct from the specific surface energy of the grain boundary. The stresses on the grain boundaries having significant excess volume are positive in sign and their magni-

tude is almost twice that of the specific surface energy of the grain boundary. The grain boundary diffusivities in Cu have been estimated on the base of investigations of the theoretical dependence of grain boundary stresses and specific surface energy on the grain boundary excess volume. The results obtained support the data yielded by direct methods which suggest that the effective diffusivities in submicrocrystalline metals exceed by a few orders the corresponding values obtained for their respective coarse-grain counterparts.

As a result of preliminary isothermal heat treatment of submicrocrystalline material, the nonequilibrium grain boundaries in the treated material pass to an equilibrium state, with the grain size remaining in the micron range. This causes a significant increase in the apparent activation energy of creep, which may be attributed to the contribution of grain boundary sliding to the total deformation becoming less due to the enhanced resistance to shear over the equilibrium grain boundaries relative to the nonequilibrium grain boundaries. As the temperature of preliminary anneals increases and approaches the temperature of recrystallization (~ 673K), the activation energy of creep also tends to grow to become equal to the activation energy of volume self-diffusion, e. g. in coarse-grain crystalline Ni. At elevated temperatures, the creep in this material is controlled by the motion and climb of dislocations, the contribution of grain boundary sliding being negligible.

6.2. Structure recovery and diffusion in nonequilibrium GBs in nanomaterials

Kinetics of grain boundary recovery in nanomaterials. As a consequence of the absorption of lattice dislocations during the preparation of nanomaterials by SPD, GBs transform into a nonequilibrium state that is characterised by long-range stresses and excess elastic energy. It is considered that these GBs largely determine many properties of nanomaterials [4, 252]. At high temperatures the nonequilibrium state of GBs is unstable. It evolves to form an equilibrium dislocation structure from extrinsic grain boundary dislocations (EGBDs). This process of relaxation of nonequilibrium grain boundary structure is referred to as grain boundary recovery. The kinetics of grain boundary recovery is of a particular importance for the structural stability of nanomaterials and their diffusion and mechanical properties at intermediate and high temperatures.

According to the recent model of GBs in nanomaterials, junction disclinations and arrays of gliding EGBDs constitute two main components of the nonequilibrium GB structure [253]. The disclinations are coupled into screened configurations such as disclination dipoles or quadrupoles, or higher order multipoles [168]. A model of the relaxation of disclination dipoles has been proposed recently [254]. According to this model, dislocations composing a disclination dipole tend to leave the host boundary through junctions under the influence of their repulsive interactions. To let the dislocations leave the boundary, a dislocation splitting reaction must occur in the junctions. If the dihedral angle between neighbouring boundaries is more than 90°, that is typical for real polycrystals, a dissociation into two dislocations with Burgers vectors parallel to neighbour boundary planes will be energetically favoured. The dislocations resulted from this dissociation can glide on corresponding boundaries unless they meet EGBDs of opposite sign gliding from neighbour junctions and annihilate. When one dislocation leaves the boundary through the junction and annihilates by this way, the next dislocation of the disclination dipole approaches the junction by climb and the process described above is repeated. As the climb of EGBDs is the slowest process, it will control the whole GB recovery process.

The relaxation of a disclination quadrupole, which is the most common defect in deformed polycrystals has been considered elsewhere [255].

Consider two finite walls of sessile EGBDs shown in Fig. 6.4. This pair of walls is equivalent to a quadrupole of disclinations located on grain junctions (Fig. 6.5). The disclination quadrupole is characterized by three parameters: strength Ω and two arms that in the most general case have different values a_1 and a_2 [256]. Normally, both the strength and arms of disclination quadrupoles may vary during relaxation. An increase of the arms without a supply of dislocations leads to a decrease of the strength of the quadrupole, as the total Burgers vector of dislocations composing the quadrupole is conserved.

In the present case the arms of the quadrupole are fixed to distances between the triple junctions, and its relaxation can only occur by a decrease of the strength, due to the loss of constituent dislocations through the triple junctions. We will consider a simple geometry of the model polycrystal such that the arms of the disclination quadrupole are equal: $2a_1=2a_2=2a=L$. Taking another geometry will change the final result by a factor of the order of unity. Let the initial value of the strength of the quadrupole be

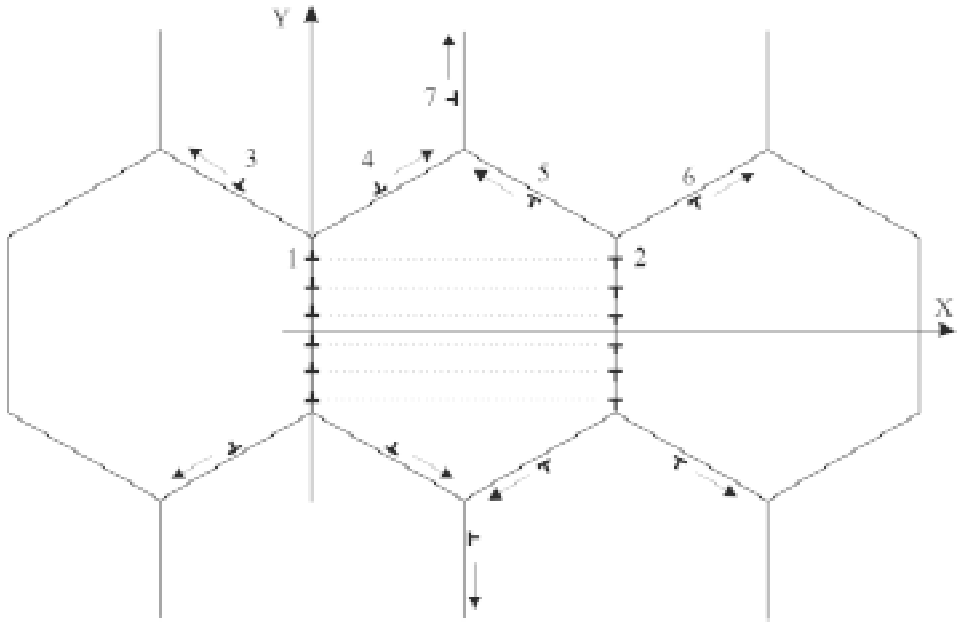

Fig. 6.4. A model for the relaxation of a system of discrete sessile EGBDs. Arrows indicate on the direction of dislocations' motion.

equal to $\Omega_0=\boldsymbol{b}/h_0$, where $\boldsymbol{b}$ is the Burgers vector of dislocations and h_0 is their initial spacing. It is assumed that in the initial state dislocations are distributed equidistantly along boundaries. Moreover, dislocations lying on the opposite boundaries are coupled into dipoles as shown in Fig. 6.4. When the temperature is raised, the dislocations climb to junctions under interaction forces. Leading dislocations of the walls can leave the boundaries if a dislocation reaction at the junctions occurs. As a result of this reaction, sessile dislocations 1 and 2 split into gliding dislocations 3, 4 and 5, 6, respectively. This splitting is energetically favored when the dihedral angle between boundaries on which dislocations 3 and 4 glide is obtuse. Further, the dislocations 3, 4 and 5, 6 can easily leave the junction by glide. In general, glide motion of EGBDs with a tangential Burgers vector may also require GB diffusion, as a step is associated with these EGBDs. However, a transformation of the steps can occur by local diffusion near the EGBD cores, thus the glide of EGBDs from the junctions are not expected to influence significantly the kinetics of relaxation. Calculations show that, if the dihedral angle between boundaries is obtuse, the forces acting on dislocations 3,4 and 5,6 repel them from the junction. If dislocations 4 and 5 do not annihilate somewhere in the middle of corresponding boundaries and reach the neighbor junctions, an energetically favored recombination reaction is possible as a consequence of which a gliding dislocation 7 forms. The latter can glide along a boundary unless it annihilates with a dislocation of opposite sign or further continue its motion through the next junction and so on. Thus, dislocations 1 and 2 can be excluded from consideration. When an EGBD leaves the boundary at each junction, the quadrupole strength decreases by b/a, where $a=L/2$, and L is the length of the boundary. After the loss of one dislocation the next dislocation approaches the junction to continue the relaxation process. It is clear from this

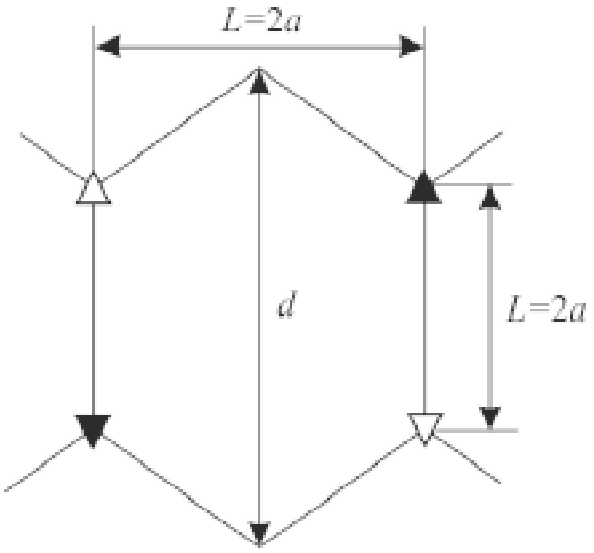

Fig. 6.5. A disclination quadrupole equivalent to a pair of EGBD walls represented in Fig. 6.4.

model that the relaxation of a disclination quadrupole is controlled by the climb of EGBDs to the triple lines, moreover the arm of the quadrupole is kept constant and equal to the length of the boundary.

Consider the two discrete dislocation walls depicted in Fig. 6.4. Let the walls contain $N=2n$ dislocations with ordinates $y_{\pm i}=\pm h_0/2, \pm 3h_0/2,...\pm(2n\text{-}1)h_0/2$. In view of symmetry of the system, the motion equations for dislocations can be written only for one wall lying in the *zOy* plane (Fig. 6.4). It is necessary to take into consideration, however, that the motion of dislocations in wall 1 occurs not only in the stress field of $(2n\text{-}1)$ dislocations of this wall, but also in the stress field of $2n$ dislocations of wall 2. Let the separation of the walls be $L=2a$. The normal stress acting on the i-th dislocation is written as

$$\sigma'_{xx} = -\frac{Gb}{2\pi(1-\nu)}\left\{\left(\sum_{j\neq i}^{n}\frac{1}{y_i-y_j}+\sum_{j=1}^{n}\frac{1}{y_i-y_j}\right)-\right.$$
$$\left.\sum_{j=1}^{n}\left[\frac{(y_i-y_j)(12a^2+(y_i-y_j)^2)}{(4a^2+(y_i-y_j)^2)^2}+\right.\right. \qquad (6.6)$$
$$\left.\left.\frac{(y_i+y_j)(12a^2+(y_i+y_j)^2)}{(4a^2+(y_i+y_j)^2)^2}\right]\right.,$$

where b is the Burgers vector magnitude of EGBDs, y_k is the ordinate of k-th dislocation. The dislocation motion is simulated according to equations [255]

$$\frac{dy_i}{dt} = -\frac{\delta D_b V_a}{bkT}\left(\frac{\sigma_{xx}^{i+1}-\sigma_{xx}^{i}}{y_{i+1}-y_i}-\frac{\sigma_{xx}^{i}-\sigma_{xx}^{i-1}}{y_i-y_{i-1}}\right). \qquad (6.7)$$

When every next dislocation approaches the bottom and upper junctions, it is excluded from consideration and n is decreased by 1. Hence the ratio $d\Omega/\Omega dt$ can be calculated from the time interval Δt in which two neighbor dislocations successively approach a junction. For any time moment the current quadrupole strength is equal to $\Omega = b/h$, where $h = L/2n=a/n$ is an average distance between dislocations. That is, $\Omega = 2nb/L$. As a consequence of a loss of one dislocation from each junction, the quadrupole's strength decreases by an amount $\Delta\Omega = 2b/L=b/a$. Therefore, the relative relaxation rate is defined as $d\Omega/\Omega dt=\Delta\Omega/\Omega\Delta t=1/n\Delta t$. For a numerical integration of Eq. (6.7) a second-order Runge-Kutte method has been applied. Plots of the dependence of $d\Omega/\Omega d\tau$ on the number of EGBDs remaining in the dipole, n, are shown in Fig. 6.6. Here the time is normalized as follows: $\tau = [4\delta D_b GV_a/(1\text{-}\nu)kTL^3]t$. These curves are qualitatively similar to the curves obtained elsewhere [254], but there are quantitative differences. Particularly, the stationary value of $d\Omega/\Omega d\tau$ is approximately equal to 6.5 (in the case of dipole $d\Omega/\Omega d\tau \approx 8$ [254]). Thus, one obtains the following equation for the relaxation of disclination quadrupole strength:

$$\frac{d\Omega}{dt} = -\frac{26\delta D_b GV_a}{\pi(1-\nu)kTL^3}\Omega \approx$$
$$-\frac{100\delta D_b GV_a}{kTd^3}\Omega, \qquad (6.8)$$

where it is taken into account that for the chosen model of a polycrystal $L \approx d/2$, d is the grain size, and it is assumed that $\nu = 0.35$. From Eq. (6.8) it follows that a disclination quadrupole relaxes similarly to a dipole according to an exponential law $\Omega(t)=\Omega_0\exp(-t/t_s)$ with a characteristic relaxation time roughly longer than the characteristic relaxation time for the dipole:

$$t_s = \frac{kTd^3}{100\delta D_b GV_a}. \qquad (6.9)$$

Calculations have shown [255] that the excess energy of the GBs due to disclination quadrupoles obeys the same exponential law of relaxation

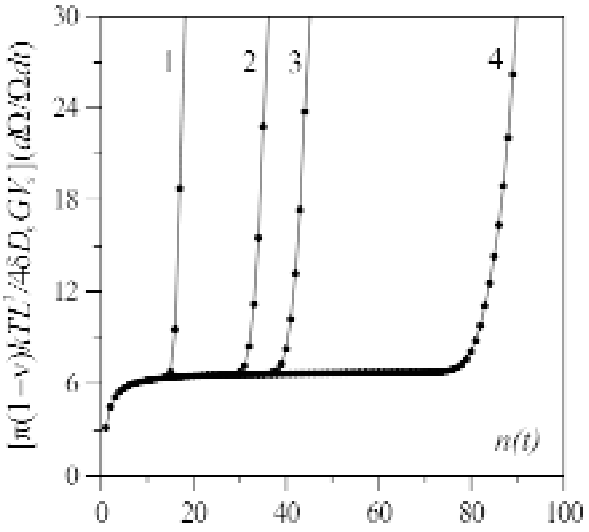

Fig. 6.6. The plots of a dependence of the relative relaxation rate of a junction disclination quadrupole on the current number of EGBDs: (curve 1), (curve 2), (curve 3), and (curve 4).

$$\Delta E = \Delta E_0 \exp\left(-\frac{t}{t_e}\right) \quad (6.10)$$

with a characteristic time equal to

$$t_e = \frac{t_s}{2} = \frac{kTd^3}{200\delta D_b G V_a}. \quad (6.11)$$

A study of the relaxation of the second main component of nonequilibrium GB structure, arrays of gliding EGBDs, shows that the average Burgers vector density of these EGBDs $\overline{\beta}$ also decreases by an exponential law with a characteristic time very similar to that given by Eq. 6.11. Therefore, Eq. (6.11) can be considered as a general equation which gives the characteristic time for grain boundary recovery.

As one can see from Eq. (6.11), the GB recovery time decreases with a decrease of the grain size. Therefore, structural transformations in nanomaterials will occur much faster than in coarse-grained polycrystals.

The results obtained can be compared to experimental data reported on samples of submicrocrystalline Cu prepared by severe plastic deformation [27]. These authors observed a significant relaxation of the GB structure and elastic moduli after 1 hour annealing of the samples at T=398K. A calculation of the characteristic relaxation time from Eq. (6.11) using the values of material parameters for Cu (δD_b=2.35·10^{-14}exp(-107200/*RT*) m^3/s [257], G=5·10^4 MPa, V_a=1.18·10^{-29} m^3) yields t_0=60 min. This is in very good agreement with the experimental data.

Relationship between the grain boundary diffusion and grain boundary recovery. Eq. (6.11) shows that the time of GB recovery depends on the GB diffusion coefficient. In turn, the GB recovery influences the GB diffusion since nonequilibrium GBs have a higher diffusion coefficient. This interrelationship is very important for understanding of the particularities of GB diffusion in nanocrystals and for a correct processing of experimental data on this characteristic.

Direct measurements of the coefficient of grain boundary diffusion D_b in nanocrystalline materials lead to contradictory results. The first investigations demonstrated that, for nanocrystals prepared through condensation in a gas with subsequent compaction of the powder, the diffusion coefficient is many orders of magnitude greater than the coefficient of grain-boundary diffusion in the materials having a standard grain size [258]. As a result, even the averaged diffusion coefficient for nanocrystals turns out to be larger than the coefficient D_b for usual materials. The activation energy of grain-boundary diffusion in nanocrystals, as a rule, is approximately equal to half the activation energy in coarse-grained materials and is close to the activation energy of surface diffusion [258]. More recent studies revealed that this effect is most likely associated with the porosity of nanocrystalline samples, which was found to be equal to 10% and greater [259]. For nanocrystals with a density close to that of the crystal, the diffusion coefficient at nanocrystal boundaries proved to be equal or somewhat greater than the diffusion coefficient at usual grain boundaries [259,260]. However, in submicrocrystalline nickel with a grain size of about 300 nm and a density approximately equal to that of the crystal, the coefficient of copper grain boundary diffusion in the temperature range 398 – 448K is four or five orders of magnitude larger than the diffusion coefficient determined from extrapolating the data for coarse-grain nickel in the high-temperature range [11]. Preliminary annealing of submicrocrystalline nickel at a temperature of 623K leads to the complete disappearance of the effect of an increase in the diffusion coefficient. From the aforesaid, it follows that the coefficient of grain-boundary diffusion in nanocrystals depends primarily not on the grain size but on the structure of the grain boundaries that exist in a nonequilibrium state in the as-prepared samples. The diffusion coefficient for nonequilibrium grain boundaries can exceed the diffusion coefficient for equilibrium grain boundaries. Possible mechanisms leading to this effect have been discussed recently (see, for example, [261,262]). Direct experimental measurements of the diffusion coefficient, as a rule, are carried out at sufficiently high temperatures in order to provide appreciable penetration of the diffusant into the studied material. Under these conditions, the nonequilibrium structure of the grain boundaries undergoes relaxation due to grain-boundary diffusion. The relaxation is accompanied by a gradual decrease in the grain-boundary diffusion coefficient. Thus, the actual diffusion experiment with nanocrystals is necessarily accomplished with a time-dependent diffusion coefficient. This can substantially affect the experimentally measured diffusion coefficient.

The GB diffusion equation with time-dependent coefficient was solved and experimental data on GB diffusion in nanocrystals were analyzed in terms of this solution [263].

In order to estimate the diffusion coefficient at nonequilibrium grain boundaries characteristic of the structure of as-prepared nanocrystals, Borisov's relationship [264] is used:

$$D_b^{ne} = D_b^{eq} \exp\left(\frac{\Delta E}{kT}\right), \tag{6.12}$$

where D_b^{ne} and D_b^{eq} are the diffusion coefficients along nonequilibrium and equilibrium grain boundaries, respectively, and ΔE is the excess energy of nonequilibrium grain boundaries per atom. The excess energy of nonequilibrium GBs depend on time according to Eq. (6.10).

If one assumes that the gradient of the diffusant concentration is directed along the x axis lying in the plane of the grain boundary, taking into account Eqs. (6.10) and (6.11), the diffusion equation can be represented in the following form

$$\frac{\partial c}{\partial t} = D_b^{eq} \exp\left(\frac{\Delta E_0}{kT} e^{-\frac{t}{t_0}}\right) \frac{\partial^2 c}{\partial x^2}. \tag{6.13}$$

This equation can be solved by changing the variables:

$$\tau = \int_0^t \exp\left(\frac{\Delta E_0}{kT} e^{-\frac{t}{t_0}}\right) dt = t_0 \int_0^{t/t_0} \exp\left(\frac{\Delta E_0}{kT} e^{-z}\right) dz, \tag{6.14}$$

As a result, we obtain a standard diffusion equation,

$$\frac{\partial c}{\partial \tau} = D_b^{eq} \frac{\partial^2 c}{\partial x^2}. \tag{6.15}$$

For diffusion in regime 'C', which is characterized by the absence of migration of the diffusant from the boundaries into the grains and is most commonly used to measure the grain-boundary diffusion coefficient in nanocrystals, the solution to Eq. (6.15) takes the form

$$c(x,\tau) = c_0 erfc\left(\frac{x}{\sqrt{4D_b^{eq}\tau}}\right). \tag{6.16}$$

As a rule, the experimental diffusion coefficient is determined by fitting the concentration profiles for diffusant obtained by either radio-tracer method or secondary ion spectroscopy. Concentration profiles are usually plotted in terms of the dependence of the diffusant concentration on the square of diffusion depth at a time corresponding to the time of diffusion annealing. It follows from Eq. (6.16) that, upon changing over from the variable τ to the variable t, the dependence of the concentration on the depth does not alter qualitatively. Consequently, the time dependence of the diffusion coefficient does not affect the functional form of the concentration profiles. However, from the analysis of the experimental profiles constructed in the $c - t$ coordinates, we can determine the effective diffusion coefficient satisfying the condition $\tau D_b^{eq} = D_{ef} t$, that is,

$$\frac{D_{ef}}{D_b^{eq}} = \frac{\tau(t)}{t}. \tag{6.17}$$

The dependence of the ratio $\tau(t)/t$ on t is shown in Fig. 6.7. As an example, the ratio at the initial moment of time is chosen equal to 100. Let us now consider two limiting cases. In the first case, the diffusion experiment is performed under the condition that the time of annealing is considerably longer than the time of relaxation: $t >> t_0$. This becomes possible at a sufficiently high temperature of annealing. Hence, we have $\tau \approx t$ and the measured diffusion coefficient coincides with the diffusion coefficient at the equilibrium grain boundaries: $D_{ef} \approx D_b^{eq}$. In the second case $t << t_0$, we obtain $\tau \approx \exp(E_0/kT)t >> t$. This situation can occur in short-time annealing at low temperatures. Under these conditions, the effective diffusion coefficient exceeds the diffusion coefficient at the equilibrium grain boundaries by several orders of magnitude. In the range between the limiting cases, the time of annealing is of the same order of magnitude as the time of relaxation and an increase in the temperature (or in the time of diffusion annealing) leads to a gradual decrease in the ratio D_b^{ne}/D_b^{eq}. It can be seen from Fig. 6.7 that, at $D_b^{ne}/D_b^{eq} = 100$, the effective diffusion coefficient exceeds the value of D_b^{eq} by approximately one order of magnitude even after a lapse of time $3t_0$. Therefore, the measured diffusion coefficient substantially depends on the time of diffusion annealing; i.e., the shorter the time of diffusion annealing, the larger the effective diffusion coefficient. In order to determine the intrinsic diffusion coefficient D_b^{eq} it is necessary to perform the diffusion annealing for a time considerably longer than t_0.

The above behavior of the diffusion coefficient is confirmed by the experimental data. For example, the measured coefficient of grain-boundary self-diffusion in nanocrystalline iron with a grain size d =

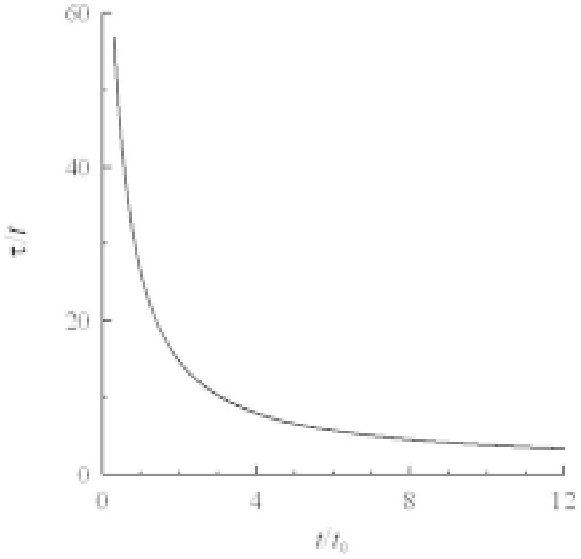

Fig. 6.7. Time dependence of the ratio characterizing the relative increase in the diffusion coefficient.

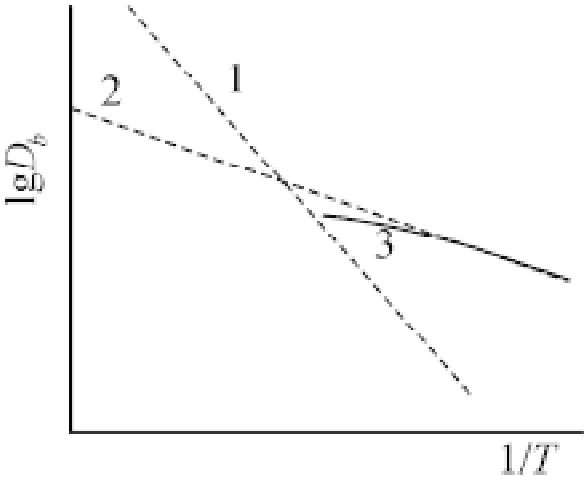

Fig. 6.8. Temperature dependences of the diffusion coefficient for (1) equilibrium grain boundaries at high temperatures, (2) nonequilibrium grain boundaries at low temperatures, and (3) nonequilibrium grain boundaries at intermediate temperatures.

19–38 nm decreases by one order of magnitude in the case when the time of diffusion annealing at the same temperature (473K) increases from 1.5 h to 3 days [265]. In submicrocrystalline nickel, the copper diffusion coefficient decreases by three orders of magnitude after annealing at a temperature of 523K [11]. The disagreement between the available experimental data can be explained to some extent in terms of the time dependence of the effective diffusion coefficient considered above. Table 6.1 presents the calculated relaxation times for the nonequilibrium structure of the grain boundaries in comparison with the times of diffusion annealing used in the experiments.

It is evident from the table that, in the measurements performed with nanocrystalline palladium and iron, the diffusion annealing over the entire temperature range covered was carried out during a period of time considerably longer than the time of relaxation. Under these conditions, the effective diffusion coefficient is close to the coefficient which is observed in the experiment. On the other hand, three-hour annealing is obviously not sufficient for relaxation of grain boundaries in nickel and the effective diffusion coefficient in submicrocrystalline nickel substantially exceeds the diffusion coefficient .

The grain boundary recovery occurring simultaneously during the diffusion experiment causes another significant effect, namely a drastic decrease in the apparent activation energy of diffusion. According to Eq. (6.12), the activation energy of diffusion decreases by ΔE; consequently, the activation energy of diffusion at the grain boundaries appears to be ΔE_b-E. Fig. 6.8 depicts the dependences $\lg D_b$-$1/T$ with activation energies E_b (straight line 1) and E_b-ΔE (straight line 2). As the temperature increases, the temperature dependence of the diffusion coefficient is represented first by branch 2 and then (after the complete relaxation of the grain boundaries) by branch 1. At intermediate temperatures and times of annealing, the relaxation decreases the diffusion coefficient at nonequilibrium grain boundaries as compared to that represented by branch 2 and the actual dependence deviates downward along

Table 6.1. Characteristic relaxation times of nonequilibrium grain boundaries in comparison with the annealing times in measurements of the diffusion coefficient of nanocrystals.

Metal	d, nm	T, K	D_b, m^2/s	t_0, h	t_d, h
Pd	100	430	$2\cdot10^{-21}$	15	240
		577	$1\cdot10^{-18}$	0.04	48
Ni	300	398	$6\cdot10^{-21}$	80	3
		448	$3\cdot10^{-19}$	1,8	3
Fe	25	450	$1\cdot10^{-22}$	3	386
		500	$1\cdot10^{-20}$	0.03	1.5-69

curve 3. The slope of this branch is less than that of branch 2. Therefore, the diffusion activation energy measured in the experiment should be less than the value of E_b-ΔE. This can explain the fact that the measured activation energy of grain-boundary diffusion in nanocrystals is approximately half that for usual polycrystals. In the case when the time of diffusion annealing is chosen without regard for the relaxation time t_0 and is identical for all the temperatures studied above, we cannot rule out the possibility that the diffusion coefficient exhibits an anomalous behavior when portion 3 in Fig. 6.8 has a negative slope, i.e., when the apparent activation energy of diffusion is negative.

6.3. Emission of lattice dislocations from grain boundaries in nanocrystalline materials

Nanocrystalline materials fabricated by severe plastic deformation methods are characterized by the specific structural features including a non-equilibrium (highly defective) state of grain boundaries, the absence of fabrication-produced flaws, and the range of grain size d from tentatively 50 to 100 nm; see, e.g., [4,266,267] and previous sections of this review article. The structural features are responsible for the outstanding mechanical properties of such nanocrystalline materials showing very high strength and hardeness [4,266,267]. At the same time, most nanocrystalline materials synthesized by severe plastic deformation and other methods (compaction of nanoparticles, electrodeposition, *etc.*) exhibit low tensile ductility. This property essentially limits practical utility of nanocrystalline materials. However, in recent years, several examples of substantial ductility and even superplasticity of nanocrystalline materials (Ni, Ni_3Al, Al- and Ti-based alloys) fabricated by severe plastic deformation have been reported [8,127,268-272]. These examples are very intriguing, because materials characterized by both high strength and enhanced ductility are highly desired for numerous structural applications. To fabricate simultaneously superstrong and ductile nanocrystalline materials of various chemical compositions, knowledge on fundamental mechanisms of plastic deformation in the nanocrystalline matter is needed. At present, though there are many experimentally documented facts, computer simulations and theoretical models of plastic deformation in nanocrystalline materials, its mechanisms and their sensitivity to the nanostructure and material parameters are under discussion; see, e.g., [273-279]. In this section, we briefly discuss theoretical representations on deformation mechanisms operating in nanocrystalline materials fabricated by severe plastic deformation and analyze the role of dislocation emission processes in achievement of ductility in such materials.

In general, the following deformation mechanisms are viewed to operate in nanocrystalline materials fabricated by various techniques [273-279]:

- lattice dislocation slip;
- twin deformation conducted by partial dislocations emitted from GBs;
- GB sliding;
- rotational deformation occurring via movement of GB disclinations;
- GB diffusional creep (Coble creep) and triple junction diffusional creep modes.

Contributions of these mechanisms to plastic flow in a nanocrystalline sample strongly depend on its structural, loading and material parameters. In doing so, the grain size d serves as the basic structural factor influencing the action of deformation mechanisms in nanocrystalline materials. Thus, the lattice dislocation slip is treated to be dominant in nanocrystalline materials with intermediate grains having the size d in the range from d_c to 100 nm, where the critical grain size d_c is around 10-30 nm and value of 100 nm is by definition the upper limit of grain sizes for nanocrystalline materials; see, e.g., [280]. In particular, it is the case of nanocrystalline materials fabricated by severe plastic deformation, because they commonly have grain sizes ranging from 50 to 100 nm [4,266,267].

The lattice dislocation slip is the dominant deformation mode in conventional coarse-grained materials where its carriers – perfect lattice dislocations – are generated and storaged in the form of dislocation cells/subgrains in large grain interiors during plastic deformation. In contrast, lattice dislocations are not intensively storied in grain interiors in deformed nanocrystalline materials with intermediate grains. The deformation behavior of these materials is crucially affected by GBs operating as active sources and sinks of lattice dislocations [281]. More precisely, GBs serve as the lattice dislocations sinks, in which case lattice dislocations are absorbed at GBs and transformed into 'extrinsic' GB dislocations (Fig. 6.9). Also, GBs serve as the lattice dislocation sources, in which case lattice dislocations are emited from GBs due to their structural transformations (Fig. 6.9).

For instance, experiments [272,282] are indicative of the emission of perfect lattice dislocations from grain boundaries. Experimental data [283-286]

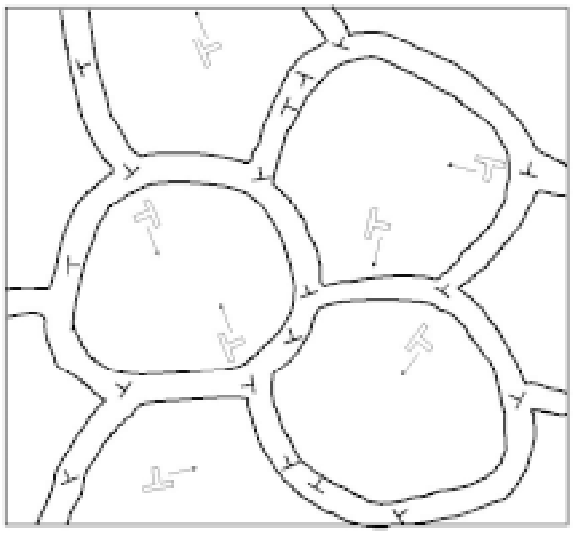

Fig. 6.9. Plastic deformation in nanocrystalline materials with intermediate grains involves intense emission of lattice dislocations from grain boundaries and absorption of lattice dislocations by grain boundaries.

give evidence for the emission of partial lattice dislocations from grain boundaries. In these circumstances, both the lattice dislocation emission from grain boundaries and, in general, evolution of dislocations at grain boundaries essentially influence plastic deformation processes in nanocrystalline materials with intermediate grains [281]. In particular, evolution of dislocations at grain boundaries crucially affects the level of the flow stress in deformed nanocrystalline materials with intermediate grains. In doing so, absorption of lattice dislocations by GBs and their transformations into 'extrinsic' GB dislocations (Fig. 6.9) provides an increase in the density of immobile dislocations at grain boundaries.

This increase leads to the strengthening of a material during plastic deformation, because immobile dislocations elastically interact with mobile dislocations and thereby hamper their movement. Both the annihilation of grain boundary dislocations and emission of lattice dislocations by GBs (Fig. 6.9) commonly provide a decrease in the density of immobile dislocations at grain boundaries and thereby give rise to the softening (recovery) of a material during plastic deformation. Following Wang and Ma [281], after some initial stage of deformation, the above competing factors – strengthening and softening – reach equilibrium. That is, a steady state is realized in which the increase in the GB dislocation density is completely compensated by the corresponding decrease. The steady state is characterized by tentatively constant values of both the mean dislocation density at GBs and flow stress. A material characterized by a tentatively constant flow stress under tensile mechanical load commonly shows plastic flow localization in shear bands, which is followed by the macroscopic necking and failure. As shown in a lot of experiments, this deformation behavior is typical for most nanocrystalline materials with intermediate grains; see [281] and references therein.

Recently, however, several groups have reported substantial tensile ductility and even superplasticity of nanocrystalline materials fabricated by severe plastic deformation and other methods [8,127,268-272,281,282,287-292]. In the case of nanocrystalline materials fabricated by severe plastic deformation, the action of plastic deformation mechanisms has its specific features that can serve as a basis for achievement of tensile ductility. First, a good tensile ductility is exhibited by nanocrystalline materials deformed at low temperatures [281,282]. In this situation, recovery processes associated with both the GB dislocation annihilation and emission of lattice dislocations by GBs are suppressed and do not compensate the strengthening associated with lattice dislocation absorption at GBs. As a result, a nanocrystalline sample under low temperature deformation can show good ductility due to the strengthening that prevents plastic flow localization.

Second, a good tensile ductility can be exhibited by nanocrystalline materials characterized by positive strain rate sensitivity of the flow stress. It means that a local increase of the plastic strain rate in a region where plastic flow is localized leads to a local increase of the flow stress in this region. As a corollary, the plastic flow localization is hampered and the neck formation is suppressed in nanocrystalline materials characterized by the positive strain rate sensitivity. Commonly the positive strain rate sensitivity occurs due to viscous plastic flow [272,293]. In this context, plastic flow characterized by the positive strain rate sensitivity can occur in nanocrystallie materials fabricated by severe plastic deformation through viscous plastic flow mechanisms conducted by non-equilibrium (highly defective) grain boundaries in such materials.

In order to achieve a good tensile ductility in a nanocrystalline material, it is crucially important to suppress brittle failure processes initiated by nucleation of nanocracks at local stress concentrators. In the context discussed, let us briefly consider the effects of both annihilation of grain boundary dislo-

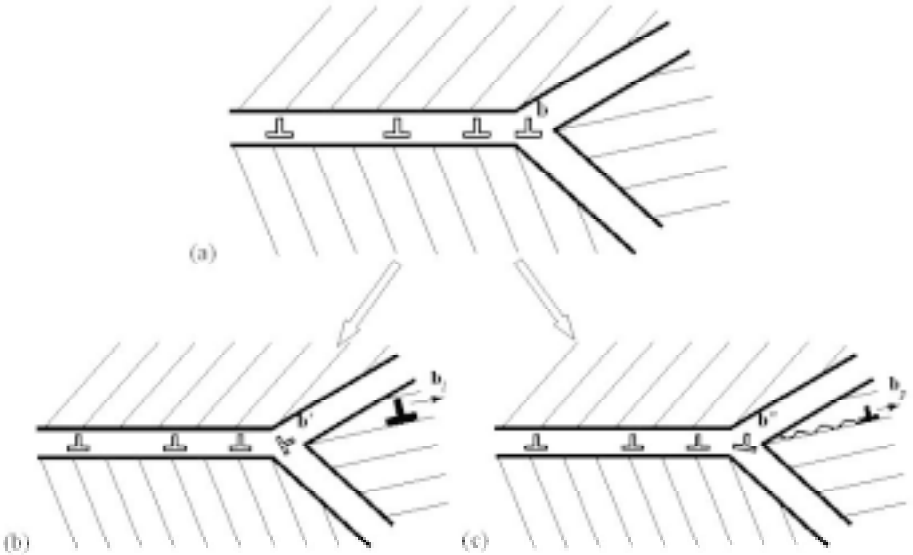

Fig. 6.10. Emission of lattice dislocations from triple junctions of grain boundaries. (a) Grain boundary dislocations (carrying grain boundary sliding) are stopped at triple junction. (b) Perfect and (c) partial lattice dislocation is emitted from triple junction that obstructs grain boundary sliding. Stacking fault (wavy line) is formed behind the moving partial dislocation.

cations and emission of lattice dislocations by grain boundaries in nanocrystalline materials fabricated by severe plastic deformation. As noted above, both the dislocation annihilation and emission of lattice dislocations by grain boundaries (Fig. 6.9) provide a decrease in the density of immobile grain boundary dislocations and thereby give rise to the softening (recovery) of a material during plastic deformation. In doing so, the annihilation processes involve dislocation configurations consisting of closely distant dislocations of opposite Burgers vectors. Such configurations of grain boundary dislocations create screened stress fields which commonly are not able to initiate the nanocrack nucleation. In contrast, the lattice dislocation emission by grain boundaries is driven by accumulation of grain boundary dislocations having Burgers vectors of one sign and thereby creating non-screened stress fields that can initiate the nanocrack nucleation [294-296]. In this context, the lattice dislocation emission by grain boundaries affects ductility of deformed nanocrystalline materials. If intensity of the lattice dislocation emission is low, a nanocrystalline specimen shows ability to intense nanocrack formation followed by the macroscopic failure. If intensity of the lattice dislocation emission is high, a nanocrystalline specimen can exhibit enhanced ductility.

Let us consider mechanisms for the lattice dislocation emission from grain boundaries. A theoretical model [297] describes emission of perfect and partial lattice dislocations as a process induced by the preceding grain boundary sliding. A pile-up of grain boundary dislocations is generated under the action of mechanical load in a grain boundary in a plastically deformed nanocrystalline sample. Mechanical-load-induced motion of the grain boundary dislocation pile-up is stopped by a triple junction. There are several ways of evolution of the grain boundary dislocation pile-up, including emission of either perfect (Fig. 6.10a) or partial (Fig. 6.10b) dislocations from the triple junction [298]. In the second case, stacking faults are formed behind the moving partial dislocations (Fig. 6.10b).

Emission of lattice dislocations by grain boundaries can effectively occur also as a process accompanying rotational deformation in nanocrystalline materials. The rotational deformation mode – plastic deformation accompanied by crystal lattice rotations – occurs through movement of grain boundary disclination dipoles and is able of effectively contributing to plastic flow in nanocrystalline materials [299-302]. It is confirmed by experimental observations of disclination dipoles and grain rotations

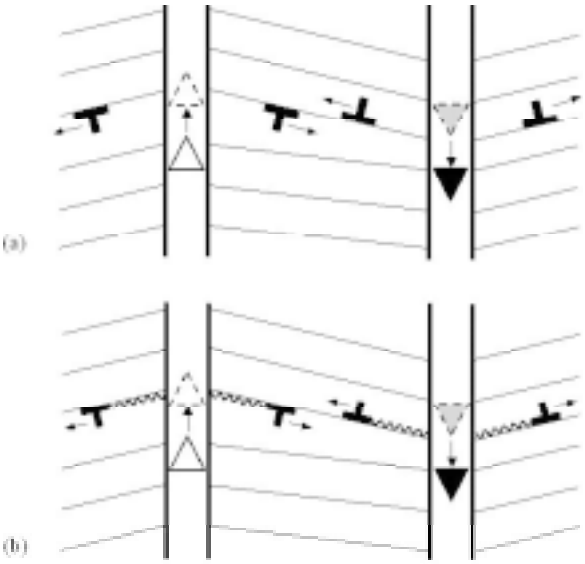

Fig. 6.11. Emission of lattice dislocations from grain boundaries with disclinations carrying rotational deformation. (a) Perfect lattice dislocations are emitted from grain boundaries due to movement of grain boundary disclinations (triangles). (b) Partial lattice dislocations are emitted from grain boundaries due to movement of grain boundary disclinations (triangles). Stacking faults (wavy line) are formed behind the moving partial dislocations.

in mechanically loaded bulk nanocrystalline materials and films [298,303,304]. Recently, theoretical models [300,301] have been suggested to describe the rotational deformation in nanocrystalline solids as the process that occurs mostly via the motion of grain boundary disclination dipoles and induces the emission of perfect and partial lattice dislocations from GBs into the adjacent grain interiors (Fig. 6.11).

These mechanisms for the dislocation emission from grain boundaries (Figs. 6.10 and 6.11) can be treated as a manifestation of the interaction between different deformation modes in deformed nanocrystalline materials. Since nanocrystalline materials are aggregates of numerous structural units (nano-sized grains and grain boundaries), different deformation mechanisms (modes) can operate and strongly influence each other. That is, there is a kind of effective interaction between deformation modes in the nanocrystalline matter. In the discussed cases, the processes of the lattice dislocation emission from grain boundaries are induced by preceeding grain boundary sliding (Fig. 6.10) and rotational deformation (Fig. 6.11).

The former case (Fig. 6.10) is an example of the effective interaction between grain boundary sliding and the lattice dislocation slip conducted by lattice dislocations emitted from grain boundaries. The second case (Fig. 6.11) is an example of the effective interaction between rotational deformation and the lattice dislocation slip.

Besides, the lattice dislocation emission from grain boundaries can occur as a result of either transformations of GB dislocations at high-angle GBs (Fig. 6.12a) or decay of low-angle GBs [305] under the shear stress action (Fig. 6.12b). In both these cases, the initial GB structures undergo transformations resulting in the lattice dislocation emission. Non-equilibrium grain boundaries in nanocrystalline materials fabricated by severe plastic deformation contain high-density ensembles of disorderedly distributed dislocations. In these circumstances, stress fields of non-equilibrium grain boundaries are characterized by essential spatial inhomogeneities that facilitate the lattice dislocation emission from these boundaries. This factor enhances ductility of nanocrystalline materials fabricated by severe plastic deformation, because the intense emission of lattice dislocations by grain boundaries eliminates local stress concentrators, nuclei of nanocracks.

Thus nanocrystalline materials fabricated by severe plastic deformation are characterized by such structural features as a non-equilibrium (highly defective) state of grain boundaries, the absence of fabrication-produced flaws, and the range of grain size d from tentatively 50 to 100 nm. With these structural features, the lattice dislocation slip is the dominant deformation mode whose action is strongly affected by non-equilibrium grain boundaries. In particular, non-equilibrium grain boundaries obstruct movement of lattice dislocations and absorb them, thus contributing to the strengthening of deformed nanocrystalline materials. On the other hand, non-equilibrium grain boundaries intensively emit perfect lattice dislocations into grain interiors. The intense emission of lattice dislocations by grain boundaries gives rise to the softening and eliminates local stress concentrators - nuclei of nanocracks – in deformed nanocrystalline materials.

So, non-equilibrium grain boundaries are able to intensively emit perfect and partial lattice dislocations into grain interiors in nanocrystalline materials fabricated by severe plastic deformation. The emission of lattice dislocations by non-equilibrium grain boundaries gives rise to the softening and eliminates local stress concentrators – nuclei of nano-

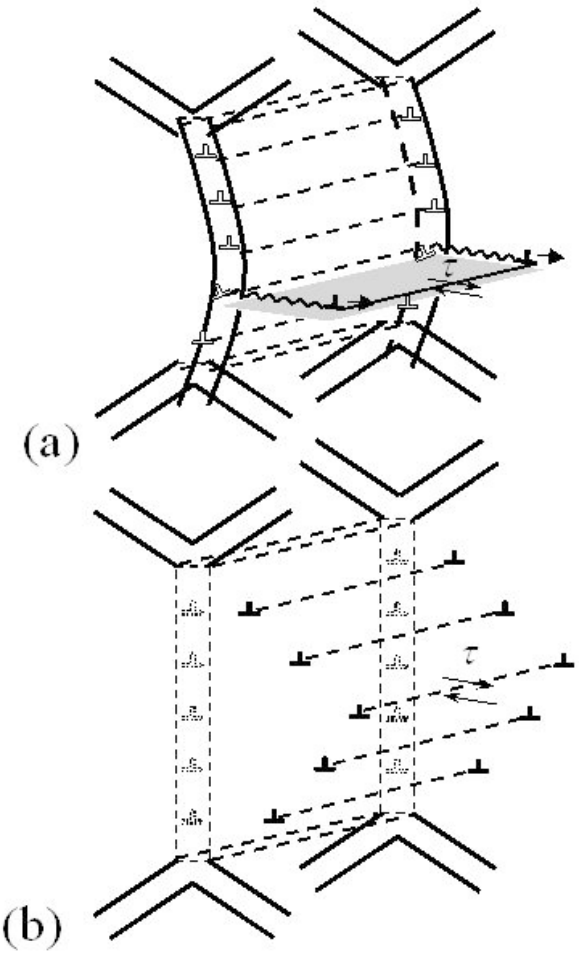

Fig. 6.12. Emission of lattice dislocations from grain boundaries. (a) Partial lattice dislocation is emitted from grain boundary due to transformation (splitting) of grain boundary dislocation. Stacking fault is formed behind the moving partial dislocation. (b) Perfect lattice dislocations are released due to decay of a low-angle tilt boundary under shear stress action.

cracks – in nanocrystalline materials under plastic deformation.

7. CONCLUDING REMARKS

This review has been devoted to a study of interface phenomena influencing advanced properties of nanoscale materials processed by means of severe plastic deformation, high-energy ball milling and their combinations. Interface phenomena include processes of interface defect structure relaxation from a highly nonequilibrium state to an equilibrium condition, grain boundary phase transformations, enhanced grain boundary and triple junction diffusivity. On the basis of an experimental investigation, a theoretical description of the key interfacial phenomena controlling the functional properties of advanced bulk nanoscale materials has been conducted. An interface defect structure investigation has been performed by TEM, high-resolution X-ray diffraction, atomic simulation and modeling. The problem of the transition from a highly non-equilibrium state to an equilibrium one, which seems to be responsible for low thermostability of nanoscale materials, was studied. Also enhanced grain boundary diffusivity is addressed. Structure recovery and grain growth in nanocrystalline materials have been investigated by analytical methods and modeling.

Several major conclusions may be drawn from these investigations:

- Severe plastic deformation such as ECAP and HPT can be successfully applied both for grain refinement in pure metals and alloys and for cold consolidation of ball milled powders;
- A correlation between microstructure and mechanical properties of Co foils prepared by ball milling and subsequent high pressure torsion has been presented. The crystallite size is found to be significantly reduced after HPT, much further than by subjecting Co powders to a long-term milling process alone. Simultaneously, large amounts of stacking faults, especially deformation faults, are created during HPT. This is in contrast with BM, where the twin fault probability is significantly larger than the deformation fault probability;
- Partially glassy materials can be prepared by cold-compaction using high pressure torsion of ball-milled $Fe_{77}Al_{2.14}Ga_{0.86}P_{8.4}C_5B_4Si_{2.6}$ amorphous ribbons. The torsion straining process induces significant changes in the short-range order (both chemical and topological) of the multicomponent alloy which result in the formation of dispersed nanocrystallites inside the amorphous matrix and a reduction in the overall crystallization enthalpy. The HPT ribbons exhibit enhanced Curie temperature and microhardness with respect to the BM ribbons. This cold-compaction technique proves itself to be appropriate for the fabrication of thin bulk partially amorphous disks and it is particularly appealing for the consolidation of amorphous alloys with reduced supercooled liquid region.
- High-resolution X-ray diffraction and TEM experiments can be used to determine the microstruc-

ture and dislocation density in ultrafine-grained materials after processing by ECAP, HPT, cold rolling and their combinations. Assuming that the crystallite size distribution in all samples obeys a log-normal function and that the strains are caused by dislocations, the parameters of the crystallite size distribution and the dislocation structure were calculated by fitting the Fourier transforms of the experimental X-ray diffraction profiles to physically well established theoretical functions. The crystallite size values were compared to the grain sizes determined by TEM. It was found that the additional deformation after ECAP resulted in further grain refinement and an increase of the dislocation density. However, electrodeposition gives an even finer microstructure and a higher dislocation density than the materials processed by SPD methods. The crystallite size values are lower than the grain size for all the specimens, since the former measures the dislocation cell size in SPD materials. For the elctrodeposited nickel, the crystallite size is close to the grain size determined by TEM;

- By means of differential scanning calorimetry and high-resolution X-ray diffraction, the microstructural parameters and released enthalpy have been measured in ultrafine-grained nickel processed by ECAP, HPT and their combination. The difference between the released DSC enthalpy and the elastic energy is attributed to the GB surface energy and the normalized surface energy has been evaluated. All nickel samples show GB surface energies for high-angle boundaries in the range of 1.0-1.2 J/m^2 which is higher than reported in the literature. This is attributed to the non-equilibrium state of GBs existing in UFG materials obtained by severe plastic deformation.
- Severe plastic deformation by HPT of binary and ternary Al-Zn, Al-Mg and Al-Mg-Zn alloys decreases drastically the size of (Al) and (Zn) grains (below 100 nm) and particles of reinforcing β and τ phases (below 10 nm). Therefore, HPT leads to the formation of a nanostructure which is less equilibrium than that of the initial coarse grained material. At the same time, during HPT the Zn-rich supersaturated solid solution (Al) decomposes completely and reaches the equilibrium corresponding to room temperature. This process is less pronounced for Mg-rich (Al). In ternary alloys Zn also leaves the supersaturated solid solution easier than Mg. Therefore, HPT leads to the formation of a phase structure which is more equilibrium than that of the initial coarse grained material. The most probable mechanism of the equilibration of the (Al) supersaturated solid solution is the grain boundary diffusion accelerated by fluxes of vacancies due to the SPD and by the sweeping of Mg and Zn atoms from the bulk by moving GBs. It appears that the severe plastic deformation of supersaturated solid solutions can be considered, similar to irradiation at ambient temperature, as a balance between deformation-induced disordering and deformation-accelerated diffusion towards the equilibrium state;
- As a result of preliminary isothermal heat treatment of submicrocrystalline material, the nonequilibrium grain boundaries in the treated material pass to an equilibrium state, with the grain size remaining in the micron range. This causes a significant increase in the apparent activation energy of creep, which may be attributed to the contribution of grain boundary sliding to the total deformation becoming less due to the enhanced resistance to shear over the equilibrium grain boundaries relative to the non-equilibrium grain boundaries. As the temperature of preliminary anneals increases and approaches the temperature of recrystallization (~ 673K), the activation energy of creep also tends to increase to become equal to the activation energy of volume self-diffusion, e. g. in coarse-grain crystalline Ni. At elevated temperatures, the creep in this material is controlled by the motion and climb of dislocations, the contribution of grain boundary sliding being negligible;
- The grain boundary recovery occurring simultaneously during the diffusion experiment causes another significant effect, namely a drastic decrease in the apparent activation energy of diffusion. This can explain the fact that the measured activation energy of grain-boundary diffusion in nanocrystals is approximately half that for usual polycrystals. In the case when the time of diffusion annealing is chosen without regard for the relaxation time and is the same for all temperatures of annealing, one cannot rule out the possibility of an anomalous behavior of the diffusion coefficient exhibiting a negative activation energy.
- Non-equilibrium grain boundaries are able to intensively emit perfect and partial lattice dislocations into grain interiors in nanocrystalline materials fabricated by severe plastic deformation. The emission of lattice dislocations by non-equilibrium grain boundaries gives rise to the softening and eliminates local stress concen-

trators - nuclei of nanocracks – in nanocrystalline materials under plastic deformation.

ACKNOWLEDGEMENTS

All authors gratefully acknowledge the support of INTAS 03-51-3779 project. Investigations of Stuttgart and Moscow teams were partly supported by Russian Foundation for Basic Research (contracts 03-02-16947, 05-02-16528) and German Federal Ministry for Education and Research (WTZ-Project RUS 04/014). A.A. Nazarov acknowledges a partial support from the Russian Science Support Foundation and from ONR through a Subcontract No. 2004-0199-01 with the North Carolina State University (NCSU PI D.W. Brenner). Bellaterra team work was partially supported by Spanish government grant (MAT 2004-01679).

Russian Foundation for Basic Research (03-02-16955) and Ministry of Education of Russian Federation and CRDF in the network of BRHE program (grant 016-02) are highly acknowledged by Tomsk team for partial support. The work of researchers (I.A. Ovid'ko and N.V. Skiba) of St. Petersburg team was partially supported by the Office of US Naval Research (grant N00014-05-1-0217), the Russian Academy of Sciences Program "Structural Mechanics of Materials and Construction Elements", and Russian Foundation of Basic Research (grant 04-01-00211).

REFERENCES

[1] H. Gleiter // *Prog. Mater. Sci*. **33** (1989) 223.
[2] H. Gleiter // *Acta Mater*. **48** (2000) 1.
[3] *Nanomaterilas for Structural Applications*, MRS Symp. Proc. Vol. 740, ed. by C.C. Berndt, T. Fischer, I. Ovid'ko, G. Skandan and T. Tsakalakos (MRS: Warrendale, 2003) and Nanotechnology Research Direction: IWGN Workshop Report. 1998.
[4] R.Z Valiev, R.K. Islamgaliev and I.V. Alexandrov // *Prog. Mater. Sci*. **45** (2000) 103.
[5] H. Tanimoto, L. Pasquini, R. Prummer, H. Kronmuller and H.-E. Schaefer // *Scripta Mater.* **42** (2000) 961.
[6] A. Hernando and J.M. Gonzalez // *Hyperfine Interact*. **130** (2000) 221.
[7] C. Suryanarayana // *JOM* **54** (2002) 24.
[8] S. X. McFadden, R. S. Mishra, R. Z. Valiev, A. P. Zhilyaev and A. K. Mukherjee // *Nature* **398** (1999) 684.
[9] L. Lu, M. L. Sui and K. Lu // *Science* **287** (2000) 1463.
[10] Yu. R. Kolobov and R. Z. Valiev, G. P. Grabovetskaya, A.P.Zhilyaev, E.F. Dudarev, K.V.Ivanov, M.B.Ivanov, O.A.Kashin and E.V. Naidenkin, *Grain boundary diffusion and properties of nanostructured materials* (Nauka Publ. (Sibirian Branch), Novosibirsk, 2001) 232p, in Russian.
[11] Yu. R. Kolobov, G. P. Grabovetskaya, M. B. Ivanov, A. P. Zhilyaev and R. Z. Valiev // *Scripta Mater*. **44** (2001) 873.
[12] L.-S. Chang, E. Rabkin, B.B. Straumal, B. Baretzky and W. Gust // *Acta Mater*. **47** (1999) 4041.
[13] B.B. Straumal, G. López, E. J. Mittemeijer, W. Gust and A.P. Zhilyaev // *Diff. Def. Forum* **216-217** (2003) 307.
[14] L. Del Bianco, A. Hernando, E. Bonetti and E. Navarro // *Phys. Rev. B* **56** (1997) 8894.
[15] E. Bonetti, L. Del Bianco, D. Fiorani, D. Rinaldi, R. Caciuffo and A. Hernando // *Phys. Rev. Lett.* **83** (1999) 2829.
[16] X. Amils, J. Nogues, S. Suriñach, J.S. Munoz, M.D. Baró, A. Hernando and J.P. Morniroli // *Phys. Rev. B* **63** (2001) 052402.
[17] Y. Iwahashi, Z. Horita, M. Nemoto and T.G. Langdon // *Acta Mater.* **45** (1997) 4733.
[18] Y. Iwahashi, Z. Horita, M. Nemoto and T.G. Langdon // *Acta Mater*. **46** (1998) 3317.
[19] A. P. Zhilyaev, G. V. Nurislamova, Bae-Kyun Kim, M. D. Baro, J. A. Szpunar and T. G. Langdon // *Acta Mater*. **51** (2003) 653.
[20] A P. Zhilyaev, J. Gubicza, S. Suriñach, M. D. Baró and T. G. Langdon // *Mater.Sci. Forum* **426-432** (2003) 4507.
[21] B. B. Straumal. *Grain boundary phase transitions* (Moscow, Nauka publishers, 2003), in Russian.
[22] M.Yu. Gutkin and I.A. Ovid'ko, *Physical Mechanics of Deformed Nanostructures. Vol. 1. Nanocrystalline Materials* (Yanus, St.-Petersburg, 2003), in Russian.
[23] M.Yu. Gutkin and I.A. Ovid'ko, *Physical Mechanics of Deformed Nanostructures. Vol. 2. Nanocrystalline Films and Coatings* (St.-Petersburg, Yanus, 2005), in Russian.
[24] M. D. Baró, Yu. R. Kolobov, I. A. Ovidko, H.-E. Schaefer, B. B. Straumal, R. Z. Valiev, I.V. Alexandrov, M. Ivanov, K. Reimann, A. B. Reizis, S. Suriñach and A. P. Zhilyaev // *Rev. Adv. Mater. Sci*. **2** (2001) 1.
[25] V.M. Segal, V.I. Reznikov, A.E. Drobyshevkij and V.I. Kopylov // *Metally* **1** (1981) 115.

[26] V.M. Segal, V.I. Reznikov, V.I. Kopylov, D.A. Pavlik and V.F. Malyshev. *Processes of plastic transformation of metals* (Navuka I tehnika, Minsk,1984), in Russian.
[27] R.Z. Valiev, A.V. Korsnikov and R.R. Mulyukov // *Mater. Sci. Eng.* **A 166** (1993) 141.
[28] N.H. Ahmadeev, R.Z. Valiev, V.I. Kopylov and R.R. Mulyukov // *Russian Metally* **5** (1992) 96.
[29] Y. Iwahashi, J. Wang, Z. Horita, M. Nemoto and T.G. Langdon // *Scripta Mater.* **35** (1996) 143.
[30] K. Nakashima, Z. Horita, M. Nemoto and T.G. Langdon // *Acta Mater*. **46** (1998) 1589.
[31] K. Oh-ishi, Z. Horita, M. Furukawa, M. Nemoto and T.G. Langdon // *Metall. Mater. Trans*. **29A** (1998) 2011.
[32] N. A. Smirnova, V. I. Levit and V.P. Pilyugin // *Phys. Met. Metall*. **61** (1986) 127.
[33] M. V. Degtyarev, T. I. Chashchukhina, L. M.Voronova, L. S. Davydova and V. P Pilyugin // *Phys. Metals Metallog*. **90** (2000) 604.
[34] R. Z.Valiev, Yu. V. Ivanisenko, E. F. Rauch and B. Baudelet // *Acta Mater.* **44 (**1996) 4705.
[35] H. S. Kim // *J. Mater. Process. Tech*. **113** (2001) 617.
[36] A.P.Zhilyaev, K. Oh-ishi, T.G. Langdon and T.R. McNelley // *Mater. Sci. Eng. A* (2005), in press.
[37] P.S. Gilman and J.S. Benjamin // *Ann. Rev. Mater. Sci.* **11** (1983) 279.
[38] C.C. Koch // *Ann. Rev. Mater. Sci*. **19** (1989) 121.
[39] C.C. Koch, In: *Processing of Metals and Alloys*, ed. by R. W. Cahn (VCH Verlagsgeselltschaft, Weinheim, 1991) p. 193.
[40] A.R. Troiano and J.L. Tokich // *Trans. Am. Inst. Min., Metall. Petrol. Eng.* **175** (1948) 728.
[41] C.R. Houska, B.L. Averbach and M. Cohen // *Acta Metall.* **33** (1985) 1293
[42] P. Tolédano, G. Krexner, M. Prem, H.P. Weber and V.P. Dmitriev // *Phys. Rev.* B **64** (2001) 144104.
[43] R. Adams and C. Altstetter // *Trans. AIME* **242** (1968) 139
[44] H. Bibring and F. Sebilleau // *Rev. Met.* **52** (1955) 569.
[45] E.A. Owen and D.M. Jones // *Proc. Phys. Soc. B* **67** (1954) 456
[46] C.G. Granqvist and R. A. Buhrman // *J. Appl. Phys*. **47** (1976) 2200.
[47] O. Kitakami, T. Sakurai, Y. Miyashita, Y. Takeno, Y. Shimada, H. Tacano, H. Awano and Y. Sugita // *Jpn. J. Appl. Phys.* **35** (1996) 1724.
[48] J.Y. Huang, Y.K. Wu and H.Q. Ye // *Appl. Phys. Lett.* **66** (1995) 308.
[49] B.S. Murty and S. Ranganathan // *Internat. Mater. Rev.* **43** (1998) 101.
[50] R.Z. Valiev, R.S. Mishra, J. Groza and A.K. Mukherjee // *Scripta Mater*. **34** (1996) 1443.
[51] P.W. Bridgeman, *Studies in large plastic flow and fracture* (McGraw-Hill, New York, 1952).
[52] L. Lutterotti and P. J. Scardi // *Appl. Crystallogr.* **23** (1990) 246.
[53] R.A. Young, *The Rietveld Method* (Oxford University Press, Oxford, 1995).
[54] L. Lutterotti and S. Gialanella // *Acta Mater*. **46** (1997) 101.
[55] P. Sahu, M. De and S. Kajiwara // *Mater. Sci. Eng. A* **333** (2002) 10.
[56] B.E. Warren, *X-ray diffraction* (Addison-Wesley, Reading, 1969).
[57] F. Cardellini and G. Mazzone // *Phil. Mag*. A **67** (1993) 1289.
[58] J.Y. Huang, Y.K. Wu and H.Q. Ye // *Acta Mater*. **44** (1996) 1201.
[59] J. Sort, J. Nogués, S. Suriñach and M.D. Baró // *Phil. Mag.* **83** (2003) 439.
[60] J. Sort, N.M. Mateescu, J. Nogues, S. Surinach and M.D. Baro // *J. Metast. Nanocryst. Mater*. **12** (2002) 126.
[61] A. Bonefacic, D. Duzevic and A. Kirin // *Fizika (Zagreb)* **12** (1980) 210.
[62] C.S. Yoo, P. Söderlind and H.Cynn // *J. Phys.: Condens. Matter.* **10** (1998) L311.
[63] A.Z. Seeger // *Zt. Metallk.* 47 (1956) 653.
[64] S. Mahajan, M.L. Green and D. Brassen // *Metall. Trans. A* **8** (1977) 283.
[65] R.W. Hertzberg, *Deformation and fracture mechanisms of engineering materials* (Wiley, New York, 1996).
[66] M.A. Meyers, O. Vöhringer and V.A. Lubarda // *Acta Mater.* **49** (2001) 4025.
[67] E. El-Danaf, S.R. Kalidindi and R.D. Doherty // *Metall. Mater. Trans*. *A* **30** (1999) 1223.
[68] M.A. Meyers, U.R. Andrade and A.H. Chokshi // *Metall. Mater. Trans. A* **26** (1995) 2881.

[69] H. Fujita and N. Fujita // *Mater. Trans.* **42** (2001) 1474.
[70] Y. Minonishi, S. Ishioka, M. Koiwa and S. Morozumi // *Philos. Mag. A* **45** (1982) 835.
[71] A. Horsewell, B. Ralph and P.R. Howell // *Phys. Stat. Sol. (a)* **29** (1975) 587.
[72] J. Singh and S. Ranganathan // *Phys. Stat. Sol (a)* **73** (1981) 243.
[73] G.M. Chow, J. Zhang, Y.Y. Li, J. Ding and W.C. Goh // *Mater. Sci. Eng. A* **304-306** (2001) 194.
[74] K. Sangwal, B. Surowska and P. Blaziak // *Mat. Chem. Phys*. **77** (2002) 511.
[75] R.S. Lima, J. Karthikeyan, C.M. Kay, J. Lidemann and C.C. Berndt // *Thin Solid Films* **416** (2002) 129.
[76] C. Suryanarayana , D. Mukhopadhyay, S.N. Patankar and F.H. Froes // *J. Mater. Res*. **7** (1992) 2114.
[77] C.S. Pande, R.A. Masumura and P.M. Hazzledine // *Mater. Phys. Mech.* **5** (2002) 16.
[78] L. Remy // *Metall. Trans. A* **12** (1981) 387.
[79] R.C. Pond, A. Serra and D.J. Bacon // *Acta Mater*. **47** (1999) 1441.
[80] I. Karaman, H. Sehitoglu, A.J. Beaudoin, Y.I. Chumlyakov, H.J. Maier and C.N. Tome // *Acta Mater*. **48** (2000) 2031.
[81] A. Inoue // *Acta Mater*. **48** (2000) 279.
[82] T. Mizoguchi, K. Yamauchi and H. Kiyajima, *Amorphous Magnetism* (Plenum, New York, 1973).
[83] H. Fugimori, T. Masumoto, Y. Obi and M. Kikuchi // *Japn. J. Appl. Phys.* **13** (1974) 1889.
[84] A. Inoue, T. Zhang and T. Masumoto // *Mater. Trans. JIM* **30** (1989) 965.
[85] T. Zhang, A. Inoue and T. Masumoto // *Mater. Trans. JIM* **32** (1991) 1005.
[86] A. Peker and W.L. Johnson // *Appl. Phys. Let.* **63** (1993) 2342.
[87] T.D. Shen and R.B. Schwarz // *Appl. Phys. Let.* **75** (1999) 49.
[88] A. Inoue // *Mater. Sci. Forum* **179-181** (1995) 691.
[89] A. Inoue // *Mater. Trans. JIM* **36** (1995) 866.
[90] A. Inoue and J.S. Gook // *Mater. Trans. JIM* **36** (1995) 1180.
[91] T. Mizushima, A. Makino and A. Inoue // *J. Appl. Phys*. **83** (1998) 6329.
[92] S. Yoshida, T. Mizushima, A. Makino and A. Inoue // *Mater. Sci. Eng. A* **304-306A** (2001) 1019.
[93] M. Stoica, J. Degmova, S. Roth, J. Eckert, J. Grahl, L. Schultz, A.R. Yavari, A. Kvick and G. Heunen // *Mater. Trans. JIM* **43** (2002) 1.
[94] A.R. Yavari, W.J. Botta Filho, C.A.D. Rodrigues, C. Cardoso and R.Z. Valiev // *Scripta Mater*. **46** (2002) 711.
[95] J. Sort, A. Zhilyaev, M. Zielinska, J. Nogués, S. Suriñach, J. Thibault and M.D. Baró // *Acta Mater*. **51** (2003) 6385.
[96] M.Takagi, Y. Kawamura, T. Imura, J. Nishigaki and H. Saka // *J. Mater. Sci*. **27** (1992) 817.
[97] H.H. Liebermann, C.D. Graham and P.J. Flanders // *IEEE Trans. Magn*. **13** (1977) 1541.
[98] G. J. Fan, M. X. Quan and Z.Q. Hu // *Appl. Phys. Let.* **68** (1996) 319.
[99] J. Sort, D.C. Ile, A. P. Zhilyaev, A. Concustell, T. Czeppe, M. Stoica, S. Suriñach, J. Eckert and M. D. Baró // *Scripta mater.* **50** (2004) 1221.
[100] W.H. Zhong, C.Q. Sun, B.K. Tay, S. Li, H.L. Bai and E.Y. Jiang // *J. Phys.: Cond. Mat*. **14** (2002) L399.
[101] N. Schlorke, J. Eckert and L. Schultz // *J. Phys. D: Appl. Phys*. **32** (1999) 855.
[102] T.W. Wu, F. Spaepen, In: *Mechanical behavior of rapidly solidified materials*, ed. by S. M. L. Sastry and B. A. McDonald (TMS-AIME, Warrendale, 1986).
[103] A. Révész, A. Concustell, L.K. Varga, S. Suriñach and M.D. Baró // *Mater. Sci. Eng. A* **375-377** (2004) 776.
[104] K. Neishi, Z. Horita and T. G. Langdon // *Mater. Sci. Eng. A* **325** (2002) 54.
[105] A. P. Zhilyaev, G. V. Nurislamova, M. D. Baro, R. Z. Valiev and T. G. Langdon // *Metall. Mater. Trans*. **33A** (2002) 1865.
[106] A. P. Zhilyaev, S. Lee, G. V. Nurislamova, R. Z. Valiev and T. G. Langdon // *Scripta Mater.* **44** (2001) 2753.
[107] J. A. Eastman, M. R. Fitzsimmons and L. J. Thompson // *Phil. Mag. B* **66** (1992) 667.
[108] Cziraki, Zs. Tonkovics, I. Gerocs, B. Fogarassy, I. Groma, E. Toth-Kadar, T. Tarnoczi and I. Bakonyi // *Mat. Sci. Eng. A* **179-180** (1994) 531.
[109] N. Wang, Z. Wang, K. T. Aust and U. Erb // *Acta Mater*. **45** (1997) 1655.
[110] T. Ungár, J. Gubicza, G. Ribarik and A. Borbély // *J. Appl. Cryst.* **34** (2001) 298.

[111] G. Ribárik, T. Ungár and J. Gubicza // *J. Appl. Cryst*. **34** (2001) 669.
[112] M. Wilkens and H. Eckert // *Z. Naturforsch. Teil. A*. **19** (1964) 459.
[113] T. Ungár, L. S. Tóth, J. Illy and I. Kovács // *Acta Metall.* **34** (1986) 1257.
[114] M. Wilkens, in: *Fundamental Aspects of Dislocation Theory*, Vol. II., ed. by J. A. Simmons, R. de Wit and R. Bullough (Nat. Bur. Stand. (US) Spec. Publ. No. 317, Washington, 1970) p.1195.
[115] T. Ungár and G. Tichy // *Phys. Status solidi a* **171** (1999) 425.
[116] T. Ungár, I. Dragomir, Á. Révész and A. Borbély // *J. Appl. Cryst*. **32** (1999) 992.
[117] A. P. Zhilyaev, G.V. Nurislamova, S. Suriñach, M.D. Baro and T.G. Langdon // *Mater. Phys. Mech*. **5** (2002) 23.
[118] A. P. Zhilyaev, B.-K. Kim, G. V. Nurislamova, M. D. Baro, J. A. Szpunar and T. G. Langdon // *Scripta Mater*. **46** (2002) 575.
[119] Y. Saito, H. Utsunomiya, T. Sakai and R.G. Hong // *Scripta Mater*. **39** (1998) 1221.
[120] Y. Saito, H. Utsunomiya, N. Tsuji and T. Sakai // *Acta Mater.* **47** (1999) 579.
[121] N. Tsuji, Y. Saito, H. Utsunomiya and S. Tanigawa // *Scripta Mater.* **40** (1999) 795.
[122] R.S. Mishra, M.W. Mahoney, S.X. McFadden, N.A. Mara and A.K. Mukherjee // *Scripta Mater.* **42** (1999) 163.
[123] J-Q. Su, T. W. Nelson and C. J. Sterling // *J. Mater. Res.* **18** (2003) 1757.
[124] I. Charit and R.S. Mishra // *Mater. Sci. Eng. A* **359** (2003) 290.
[125] Y.S. Sato, Y. Kurihara, S.H.C. Park, H. Kokawa and N. Tsuji // *Scripta Mater.* **50** (2004) 57.
[126] A.P. Zhilyaev, J. Gubicza, G. Nurislamova, A. Revesz, S. Suriñach, M.D. Baró and T. Ungár // *Phys. stat. sol. a* **198** (2003) 263.
[127] R.Z. Valiev, I.V. Alexandrov, Y.T. Zhu and T.C. Lowe // *J. Mater. Res.* **17** (2002) 5.
[128] V.M. Segal // *Mater. Sci. Eng., A* **197** (1995) 157.
[129] V.M. Segal // *Mater. Sci. Eng. A* **271** (1999) 322.
[130] M. Furukawa, Z. Horita, M. Nemoto and T.G. Langdon // *J. Mater. Sci*. **36** (2001) 2835.
[131] J. Wang, Y. Iwahashi, Z. Horita, M. Furukawa, M. Nemoto, R.Z. Valiev and T.G. Langdon // *Acta Mater*. **44** (1996) 2973.
[132] H. Hasegawa, S. Komura, A. Utsunomiya, Z. Horita, M. Furukawa, M. Nemoto and T.G. Langdon // *Mater. Sci. Eng. A* **265** (1999) 188.
[133] A.P. Zhilyaev, V.Yu. Gertsman, O.V. Mishin, A.I. Pshenichnyuk, I.V. Aleksandrov and R.Z. Valiev // *Acta Metall. Mater.* **41** (1993) 2657.
[134] V.Y. Gertsman, K. Tangri and R.Z. Valiev // *Acta Metall. Mater.* **42** (1994) 1785.
[135] A. Gholinia, P.B. Prangnell and M.V. Markushev // *Acta Mater.* **48** (2000) 1115.
[136] C.P. Chang, P.L. Sun and P.W. Kao // *Acta Mater.* **48** (2000) 3377.
[137] J.C. Huang, I.C. Hsiao, T.D. Wang and B.Y. Lou // *Scripta Mater.* **43** (2000) 213.
[138] J-Y. Chang, J-S. Yoon and G-H. Kim // *Scripta Mater.* **45** (2001) 347.
[139] S.D. Terhune, D.L. Swisher, K. Oh-ishi, Z. Horita, T.G. Langdon and T.R. McNelley // *Metall. Mater. Trans.* **33A** (2002) 2173.
[140] Z.C. Wang and P.B. Prangnell // *Mater. Sci. Eng. A* **328** (2002) 87.
[141] J.R. Bowen, O.V. Mishin, P.B. Prangnell and D. Juul Jensen // *Scripta Mater.* **47** (2002) 289.
[142] P.L. Sun, C.Y. Yu, P.W. Kao and C.P. Chang // *Scripta Mater*. **47** (2002) 377.
[143] Y.C. Chen, Y.Y. Huang, C.P. Chang and P.W. Kao // *Acta Mater*. **51** (2003) 2005.
[144] O.V. Mishin, D. Juul Jensen and N. Hansen // *Mater. Sci. Eng. A* **342** (2003) 320.
[145] A. Goloborodko, O. Sitdikov, T. Sakai, R. Kaibyshev and H. Miura // *Mater. Trans.* **44** (2003) 766.
[146] O.V. Mishin, V.Y. Gertsman, R.Z. Valiev and G. Gottstein // *Scripta Mater.* **35** (1996) 873.
[147] G. Wang, S.D. Wu, L. Zuo, C. Esling, Z.G. Wang and G.Y. Li // *Mater. Sci. Eng*., **A346** (2003) 83.
[148] W.S. Choi, H.S. Ryoo, S.K. Hwang, M.H. Kim, S.I. Kwun and S.W. Chae // *Metall. Mater. Trans.* **33A**, (2002) 973.
[149] D.J. Dingley and D.P. Field // *Mater. Sci. Technol.* **12** (1996) 1.
[150] J. Wang, Z. Horita, M. Furukawa, M. Nemoto, N.K. Tsenev, R.Z. Valiev, Y. Ma and T.G. Langdon // J. *Mater. Res.* **8** (1993) 2810.

[151] Z. Horita, D.J. Smith, M. Furukawa, M. Nemoto, R.Z. Valiev and T.G. Langdon // *J. Mater. Res*. **11** (1996) 1880.
[152] D.G. Brandon // *Acta Metall.* **30** (1966) 1479.
[153] G.R. Canova, U.F. Kocks and J.J. Jonas // *Acta Metall.* **32** (1984) 211.
[154] L.S. Tóth, R.A. Maisson, L. Germain, S.C. Baik and S. Suwas // *Acta Mater*. **52** (2004) 1885.
[155] D. Swisher, K. Oh-ishi, A. P. Zhilyaev and T. R. McNelley, (2005), to be published.
[156] W.T. Read, *Dislocations in Crystals* (McGraw-Hill, New York, 1953).
[157] M.W. Grabski and R. Korski // *Phil. Mag*. **22** (1970) 707.
[158] Y.K. Huang, A.A. Menovsky and F.R. de Boer // *NanoStruct. Mater*. **2** (1993) 587.
[159] H. Jiang, Y.T. Zhu, D.P. Butt, I.V. Alexandrov and T.C. Lowe // *Mater. Sci. Eng. A* **290** (2000) 128.
[160] A. Tschope, R. Birringer and H. Gleiter // *J. Appl. Phys*. **71** (1992) 5391.
[161] L.C. Chen and F.J. Spaepen // *J. Appl. Phys*. **69** (1991) 679.
[162] R.Z. Valiev // *Ann. Chim. Fr*. **21** (1996) 369.
[163] F.Z. Utyashev, F.U. Enikeev and V.V. Latysh // *Ann.Chim. Fr*. **21** (1996) 379.
[164] M. Djahanbakhsh, W. Lojkowski, G. Bürkle, G. Baumann, Y.V. Ivanisenko, R.Z. Valiev and H.-J. Fecht // *Mater. Sci. Forum* **360-362** (2001) 175.
[165] A.V. Korznikov, Yu.V. Ivanisenko, D.V. Laptionok, I.M. Safarov, V.P. Pilyugin and R.Z. Valiev // *NanoStruct. Mater*. **4** (1994) 159.
[166] V.A. Likhachev and V.V.Rybin // *Izvestia AN SSSR. ser. fiz*. **37** (1973) 2433.
[167] Yu. Ivanisenko, W. Lojkowski, R.Z. Valiev and H.-J. Fecht // *Acta Mater*. **51** (2003) 5555.
[168] V.V.Rybin, *Large plastic deformation and fracture of metals* (Metallurgia, Moscow, 1986),in Russian.
[169] V.V. Rybin, A.A. Zisman and N.Yu. Zolotorevsky // *Acta Metall. Mater.* **41** (1993) 2211.
[170] *Phase transformations during irradiation*, ed. by F.V. Nolfi Jr. (Applied Science Publishers, London, 1983).
[171] N.L. Peterson and S.J. Rothman // *Phys. Rev. B* **1** (1970) 3264.
[172] I. Gödény, D.L. Beke and F.J. Kedves // *Phys. stat. sol. a* **13** (1972) 155.
[173] S.J. Rothman, N.L. Peterson, L.J. Nowicki and L.C. Robinson // *Phys. stat. sol. b* **63** (1974) K29.
[174] D.M. Poole and H.J. Axon // *J. Inst. Met.* **80** (1952) 599.
[175] E.C. Ellwood // *J. Inst. Met.* **80** (1952) 217.
[176] H.J. Axon and Y.W. Hume-Rothery // *Proc. Roy. Soc.* **193** (1948) 1.
[177] D.M. Poole and H.J. Axon // *J. Inst. Met*. **80** (1952) 599.
[178] *Binary alloy phase diagrams*, ed. by T.B. Massalski *et al.* (ASM International, Materials Park, OH, 1993).
[179] *Ternary alloys*, **Vol. 7,** ed. by G. Petzov and G. Effenberg (MSI-VCH, Weinheim, 1993).
[180] Y.-S. Kang, H. Araki, Y. Minamino, T. Yamane, S. Saji, K. Azuma and Y. Miyamoto // *J. Japan Inst. Metals* **57** (1993) 990.
[181] Y. Fujinaga and T. Sato. // *J. Alloys and Comp.* **209** (1994) 311.
[182] M.I. Zakharova and V.A. Ilina // *Zh. Fiz. Khim*. **24** (1950) 714, in Russian.
[183] G. Martin, R. Cauvin and A. Barbu, In: *Phase transformations during irradiation* ed. by Nolfi F. V. Jr. (Applied Science Publishers, London, 1983) p.47.
[184] L.-S. Chang, E. Rabkin, B.B. Straumal, B. Baretzky and W. Gust // *Acta mater.* **47** (1999) 4041.
[185] B. Straumal, S.I. Prokofjev, L.-S. Chang, N.E. Sluchanko, B. Baretzky, W. Gust and E. Mittemeijer // *Def. Diff. Forum* **188-190** (2001) 1343.
[186] B.B. Straumal, P. Zieba and W. Gust // *Int. J. Inorg. Mater*. 3 (2001) 1113.
[187] E.I. Rabkin, V.N. Semenov, L.S. Shvindlerman and B.B. Straumal // *Acta metall. mater*. 39 (1991) 627.
[188] E.I. Rabkin, L.S. Shvindlerman and B.B. Straumal // In*t. J. Mod. Phys. B* **5** (1991) 2989.
[189] J. Schölhammer, B. Baretzky, W. Gust, E. Mittemeijer and B. Straumal // *Interf. Sci*. **9** (2001) 43.
[190] L.-S. Chang, E. Rabkin, B.B. Straumal, S. Hoffmann, B. Baretzky and W. Gust // *Defect Diff. Forum* **156** (1998) 135.
[191] O.I. Noskovich, E.I. Rabkin, V.N. Semenov, B.B. Straumal and L.S. Shvindlerman // *Acta metall. mater*. 39 (1991) 3091.

[192] B.B. Straumal, O.I. Noskovich, V.N. Semenov, L.S. Shvindlerman, W. Gust and B. Predel // *Acta metall. mater*. 40 (1992) 795.
[193] B. Straumal, E. Rabkin, W. Lojkowski, W. Gust and L.S. Shvindlerman // *Acta mater.* **45** (1997) 1931.
[194] B. Straumal and B. Baretzky // *Diff. Def. Forum* **216-217** (2003) 53.
[195] B.B. Straumal, N.E. Sluchanko and W. Gust // *Def. Diff. Forum* **188-190** (2001) 185.
[196] B. Straumal, G. Lopez, W. Gust and E. Mittemeijer, In: *Nanomaterials by severe plastic deformation. Fundamentals – Processing – Applications*, ed. by M.J. Zehetbauer and R.Z. Valiev (University of Vienna, Vienna, 2003) p. 642.
[197] K. Higashi, T.G. Nieh, M. Mabuchi and J. Wadsworth // *Scripta metall. mater*. **32** (1995) 1079.
[198] Y. Takayama, T. Tozawa and H. Kato // *Acta mater.* **47** (1999) 1263.
[199] L.F. Vereshchagin, *Synthetic diamonds and hydraulic extrusion* (Nauka, Moscow, 1997),in Russian.
[200] R. Cauvin and G.Martin // *J. Nucl. Mater*. **83** (1979) 67.
[201] R. Cauvin and G. Martin // *Phys. Rev. B* **23** (1981) 3322.
[202] R. Cauvin and G. Martin // *Phys. Rev. B* **23** (1981) 3333.
[203] R. Cauvin and G. Martin // *Phys. Rev. B* **25** (1983) 3385.
[204] J. Friedel, *Dislocations* (Pergamon press, Oxford, 1964).
[205] T.H. Blewitt, R.R. Coltman and J.K. Redman // *J. Appl. Phys*. **28** (1954) 651.
[206] M. Winterberger // *Acta Metall*. **7** (1959) 549.
[207] Z. Gyulai and D. Hartley // *Z. Physik* **51** (1928) 378.
[208] G. Saada // *Acta Met.* **9** (1961) 166.
[209] G. Saada // *Acta Met*. **9** (1961) 965.
[210] G. Saada // *Acta Met*. **10** (1962) 551.
[211] D.L. Beke, I. Gödény, G. Erdelyi and F.J. Kedves // *Phil. Mag. A* **56** (1987) 659.
[212] D.L. Beke, I. Gödény and F.J. Kedves // *Phil. Mag. A.* **47** (1983) 281.
[213] D.L. Beke, I. Gödény and F.J. Kedves // *Trans. Jap. Inst. Met. Suppl.* **27** (1986) 649.
[214] A.N. Aleshin, V.Yu. Aristov, B.S. Bokstein and L.S. Shvindlerman // *Phys.stat. sol. a* **45** (1978) 359.
[215] A.N. Aleshin, B.S. Bokstein, A.L. Petelin and L.S. Shvindlerman // *Metallofizika* **2** (1980) 83.
[216] P. Zieba, A. Pawlowski and W. Gust // *Def. Diff. Forum* **194** (2001) 1759.
[217] A. Häßner // *Isotopenpraxis* **5** (1969) 143.
[218] A. Häßner // *Krist. Tech*. **8** (1973) 1.
[219] A. Häßner // *Krist. Tech.* **9** (1974) 1371.
[220] T. Fujita, H. Hasegawa, Z. Horita and T.G. Langdon // *Def. Diff. Forum* **194** (2001) 1205.
[221] T. Fujita, Z. Horita and T.G. Langdon // *Mater. Sci. Forum* **396-402** (2002) 1061.
[222] T. Fujita, Z. Horita and T.G. Langdon // *Mater. Sci. Eng.* **A371** (2004) 241.
[223] A.B. Vladimirov, V.N. Kaygorodov, S.M. Klotsman, V.D. Symbelov and I.S. Trachtenberg // *Phys. Metal. Metallogr.* **39(1)** (1975) 78.
[224] Y. Minamino, Y. Toshimi, A. Shinomura, M. Shimada, M. Koizumi, N. Ogawa, J. Takahashi and H. Kimura // *J. Mater. Sci.* **18** (1983) 2679.
[225] G. Erdelyi, W. Lojkowski, D.L. Beke, I. Godeny and F.J. Kedves // *Phil. Mag. A* **56** (1987) 673.
[226] O. A. Kaibyshev and R.Z. Valiev, *Grain boundaries and properties of metals* (Metallurgija, Moscow. 1987), in Russian.
[227] Yu. R. Kolobov, *Diffusion-controlled processes on grain boundaries and ductility of metal polycrystals* (Nauka, Novosibirsk, 1998), in Russian.
[228] A.N.Orlov, V.N. Perevezentsev and V. V. Rybin, *Grain boundaries in metals* (Metallurgija, Moscow. 1980), in Russian.
[229] H. Gleiter and B. Chalmers // *Prog. Mater. Sci.* (1972).
[230] T. Watanabe // *Mater. Sci. Forum* **243-245** (1997) 21.
[231] R.Z.Valiev and I.V.Alexandrov, *Nanostructured materials produced by severe plastic deformation* (Logos, Moscow, 2000), in Russian.
[232] N. I. Noskova and R.R. Mulyukov, *Submicrocrystalline and nanocrystalline metals and alloys*. (UrO RAN, Ekaterinburg, 2003), in Russian.

[233] G.P. Grabovetskaya, I.V. Ratochka, Yu. R. Kolobov and L.N.Puchkareva // *Phys. Metals Metallogr.* **83** (1997) 112.
[234] R. Würschum, K.Reimann, S. Grub *et al.* // *Phil. Mag. Let.* **76** (1997) 407.
[235] Yu.R. Kolobov, G.P. Grabovetskaya, K.V. Ivanov and M.B. Ivanov // *Interface Sci.* **10** (2002) 31.
[236] H. Ibach // *Surface Sci. Report* **29** (1997) 193.
[237] D. Wolf // *Phil. Mag. A* **62** (1990) 447.
[238] Y. Mishin, M.J. Mehl, D.A. Papaconstantpoulos, A.F. Voter and J.D. Kress // *Phys. Rev. B* **63** (2001) 224106.
[239] M. S. Daw and M. I. Baskes // *Phys. Rev. B* **29** (1984) 6443.
[240] G.J. Ackland and M.W. Finnis // *Phil. Mag. A* **54** (1986) 301.
[241] P.Gumbsch and M.S. Daw // *Phys. Rev. B* **44** (1991) 3934.
[242] D. Wolf // *Phil. Mag. A* **62** (1990) 447.
[243] K.L Merkle // *Microsc. Microanal*. **3** (1997) 339.
[244] P.Beurden and G.J. Kramer // *Phys. Rev. B* **63** (2001) 165106.
[245] Yu.R. Kolobov, I.V. Ratochka, K.V. Ivanov and A.G. Lipnitskiy // *Russian Physics Journal* **8 (**2004) 49.
[246] Yu.R. Kolobov, G.P Grabovetskaya, K.V. Ivanov and M.B. Ivanov // *Defect and Diffusion Foru*. **216-217** (2003) 253.
[247] G.P.Grabovetskaya, Yu.R.Kolobov, K.V.Ivanov and N.V.Girsova // *Phys. Metals Metallography* **94** (2002) S37.
[248] M.V. Grabskiy, *Structural superplasticity of metals* (Metallurgia, Moscow. 1975).
[249] G.P.Grabovetskaya, Yu.R. Kolobov, K.V.Ivanov and N.V.Girsova // *Phys. Metals Metallogr.* **91** (2001) 532.
[250] H.J. Frost and M.F. Ashby, *Deformation-mechanism maps* (Pergamon Press, 1982).
[251] R.Z. Valiev, E.V. Kozlov, Yu.V. Ivanov, J. Lian, A.A. Nazarov and B. Baudelet // *Acta Metal. Mater*. **42** (1994) 2467.
[252] A.A. Nazarov and R.R. Mulyukov, In: *Handbook of Nanoscience, Engineering and Technology*, ed by W.A. Goddard, D. Brenner, S.E. Lyshevski and G.J. Iafrate (CRC Press, 2002) p.22-1.
[253] A.A. Nazarov, A.E. Romanov and R.Z. Valiev // *Acta Metall. Mater*. **41** (1993) 1033.
[254] A.A. Nazarov // *Interface Sci*. **8** (2000) 315.
[255] D.V. Bachurin and A.A. Nazarov // *Philos. Mag*. *A* **83** (2003) 2653.
[256] A.E. Romanov and V.I. Vladimirov, In: *Dislocation in Solids*, V.9, ed by F.R.N. Nabarro (North-Holland, Amsterdam, 1992) p.191.
[257] I. Kaur, W. Gust and L. Kozma, *Handbook of Grain Boundary and Interphase Boundary Diffusion Data* (Stuttgart: Ziegler Press, 1989).
[258] H. Gleiter // *Phys. status sol. b* **172** (1992) 41.
[259] R.Würschum, U.Brossmann and H.-E. Schaefer, In: *Nanostructured Materials: Processing, Properties, and Potential Applications*, ed. by C.C. Koch *et al.* (William Andrew, New York, 1998).
[260] R. Würschum, K. Reimann, S. Grub, A. Kubler, P. Schwarwaechter, W. Frank, O. Kruse, H.D. Carstanjen and H-E. Schaefer // *Philos. Mag. B* **76** (1997) 401.
[261] I.A. Ovid'ko, A.B. Reizis and R.A. Masumura // *Mater. Phys. Mech.* **1** (2000) 103.
[262] A.A. Nazarov // *Philos. Mag. Let.* **80** (2000) 221.
[263] A.A. Nazarov // *Phys. Sol. State* **45** (2003) 1166.
[264] V.T. Borisov, V.M. Golikov and G.V. Shcherbedinski // *Phys. Metals Metallogr*. **17** (1964) 881.
[265] S. Herth, T. Michel, H. Tanimoto, M. Egersmann, R. Dittmar, H.-E. Schaefer, W. Frank and R. Wurschum // *Def. Diff. Forum* 1**94-199** (2001) 1199.
[266] *Investigations and Applications of Severe Plastic Deformation*, ed. by T.C. Lowe and R.Z. Valiev (Kluwer, Dordrecht, 2000).
[267] R.Z. Valiev // *Nature Mater*. **3** (2004) 511.
[268]R.S. Mishra, V.V. Stolyarov, C. Echer, R.Z. Valiev and A.K. Mukherjee // *Mater. Sci. Eng. A* **298** (2001) 44.
[269] R.Z. Valiev, C. Song, S.X. McFadden, A.K. Mukherjee and R.S. Mishra // *Phil .Mag. A* **81** (2001) 25.
[270] R.S. Mishra, R.Z. Valiev, S.X. McFadden, R.K. Islamgaliev and A.K. Mukherjee // *Phil. Mag. A* 81 (2001) 37.
[271] R.K. Islamgaliev, R.Z. Valiev, R.S. Mishra and A.K. Mukherjee // *Mater. Sci. Eng. A* **304-306** (2001) 206.
[272] A.K. Mukherjee // *Mater. Sci. Eng. A* **322** (2002) 1.

[273] K.S. Kumar, S. Suresh and H. Swygenhoven // *Acta Mater.* **51** (2003) 5743.
[274] *Mechanical Properties of Nanocrystalline Materials and Nanocomposites,* ed. by I.A. Ovid'ko, C.S. Pande, R. Krishnamoorti, E. Lavernia and G. Skandan (MRS, Warrendale, 2004).
[275] X. Zhang, H. Wang and C.C. Koch // R*ev. Adv. Mater. Sci*. **6** (2004) 53.
[276] M.Yu. Gutkin and I.A. Ovid'ko, *Plastic Deformation in Nanocrystalline Materials* (Springer, Berlin, Heidelberg, New York, 2004).
[277] D. Wolf, V. Yamakov, S.R. Phillpot, A.K. Mukherjee and H. Gleiter // *Acta Mater.* **53** (2005) 1.
[278] I.A. Ovid'ko // *Int. Mater. Rev.* **50** (2005), in press.
[279] B.Q. Han, E.J. Lavernia and F.A. Mohamed // *Rev. Adv. Mater. Sci. **9** (2004) 1.*
[280] *Nanotechnology Research Directions*, ed. by M.C. Roco, R.S. Williams and P. Alivisatos (Kluwer, Dordrecht, 2000).
[281] Y.M. Wang and E. Ma // *Acta Mater.* **52** (2004) 1699.
[282] K.S. Kumar, S. Suresh, M.F. Chisholm, J.A. Horton and P. Wang // *Acta Mater.* **51** (2003) 387.
[283] J. H. He and E.J. Lavernia // *J. Mater. Res.* **16** (2001) 2724.
[284] M.W. Chen, E. Ma, K.J. Hemker, H.W. Sheng, Y.M. Wang and X.M. Cheng // *Science* **300** (2003) 1275.
[285] X.Z. Liao, F. Zhou, E.J. Lavernia, S.G. Srinivasan, M.I. Baskes, D.W. He and Y.T. Zhu // *Appl. Phys. Lett.* **83** (2003) 632.
[286] X.Z. Liao, S.G. Srinivasan, Y.H. Zhao, M.I. Baskes, Y.T. Zhu, F. Zhou, E.J. Lavernia and H.F. Hu // *Appl. Phys. Lett.* **84** (2004) 3564.
[287] Y. Wang, E. Ma, R.Z. Valiev and Y. Zhu // *Adv. Mater*. **16** (2004) 328.
[288] V.L. Tellkamp, A. Melmed and E.J. Lavernia // *Metall. Mater. Trans. A* **32** (2001) 2335.
[289] Y. Wang, M. Chen, F. Zhou and E. Ma // *Nature* **419** (2002) 912.
[290] G. He, J. Eckert, W. Loeser and L. Schultz // *Nature Mater.* **2** (2003) 33.
[291] A.V. Sergueeva, N.A. Mara and A.K. Mukherjee // *Rev. Adv. Mater. Sci*. **7** (2004) 67.
[292] K.M. Youssef, R.O. Scattergood, K.L. Murty and C.C. Koch // *Appl. Phys. Lett*. **85** (2004) 929.
[293] K.A. Padmanabhan and H. Gleiter // *Mater. Sci. Eng. A* **381** (2004) 28.
[294] I.A. Ovid'ko and A.G. Sheinerman // *Acta Mater.* **52** (2004) 1201.
[295] I.A. Ovid'ko and A.G. Sheinerman // *Acta Mater*. **53** (2005) 1347.
[296] M.Yu. Gutkin and I.A. Ovid'ko // *Phil. Mag. Let.* **84** (2004) 655.
[297] A.A Fedorov, M.Yu. Gutkin and I.A. Ovid'ko // *Acta Mater.* **51** (2003) 887.
[298] M. Ke, W.W. Milligan, S.A. Hackney, J.E. Carsley and E.C. Aifantis // *Nanostruct. Mater*. **5** (1995) 689.
[299] I.A. Ovid'ko // *Science* **295** (2002) 2386.
[300] M.Yu. Gutkin, A.L. Kolesnikova, I.A. Ovid'ko and N.V. Skiba // *Phil. Mag. Let*. **82** (2002) 651.
[301] M.Yu. Gutkin, I.A. Ovid'ko and N.V. Skiba // *Phys. Sol. State* **46** (2004) 2042.
[302] M.Yu. Gutkin, I.A. Ovid'ko and N.V. Skiba // *Acta Mater*. **51** (2003) 4059.
[303] M. Murayama, J.M. Howe, H. Hidaka and S. Takaki // *Science* **295** (2002) 2433.
[304] Z. Shan, E.A. Stach, J.M.K. Wiezorek, J.A. Knapp, D.M. Follstaedt and S.X. Mao // *Science* **305** (2004) 654.
[305] S.V. Bobylev, M.Yu. Gutkin and I.A. Ovid'ko // *Acta Mater.* **52** (2004) 3793.